Failure Analysis of Thick Composite Flexural Plates Constrained by Bolt Joints

Alireza Gorjipoor

A Thesis
In the Department
of
Mechanical, Industrial & Aerospace Engineering

Presented in Partial Fulfillment of the Requirements
For the Degree of
Doctor of Philosophy (Mechanical Engineering) at
Concordia University
Montreal, Quebec, Canada

March 2018

CONCORDIA UNIVERSITY
SCHOOL OF GRADUATE STUDIES

This is to certify that the thesis prepared

By: Alireza Gorjipoor

Entitled: Failure Analysis of Thick Composite Flexural Plates Constrained by Bolt Joints

and submitted in partial fulfillment of the requirements for the degree of

Doctor of Philosophy (Mechanical Engineering)

complies with the regulations of the University and meets the accepted standards with respect to originality and quality.

Signed by the final examining committee:

____Chair
Dr. S. Samuel Li

____External Examiner
Dr. Wenbin Yu

____External to Program
Dr. Catharine Marsden

____Examiner
Dr. Mehdi Hojjati

____Examiner
Dr. Ayhan Ince

____Thesis Co-Supervisor
Dr. Suong Van Hoa

____Thesis Co-Supervisor
Dr. Rajamohan Ganesan

Approved by ____
Dr. Ali Dolatabadi, Graduate Program Director

Thursday, April 26, 2018 ____
Dr. Amir Asif, Dean
Faculty of Engineering and Computer Science

Abstract

Title: Failure Analysis of Thick Composite Flexural Plates Constrained by Bolt Joints

Alireza Gorjipoor, Ph.D.

Concordia University, 2018

This research study introduces a numerical model to predict failure in thick glass/epoxy laminated beams subjected to flexural bending moment and bolt joint loads. The accuracy of the proposed model was verified by experiments using strain gages and Digital Image Correlation (DIC) methods. During last decades, aluminum and steel have been substituted by composite materials specially in the aerospace industry where higher specific strength and stiffness are the main criteria for material selection. The yoke of the helicopter is one of the recent applications of thick composite structures. The yoke connects the main rotor blade to the hub using bolt joints and it is manufactured as a thick glass/epoxy beam. Performing the experimental tests during the design process of the yoke is highly expensive and time-consuming.

In this study, a numerical model is introduced to perform stress and failure analysis for a simplified model of the yoke. This simplified model consists of a thick composite laminate subjected to flexural bending moment and bolt joint connections. At first, a finite element model was developed to predict the structural behavior of the beam in the presence of flexural bending which is the main load in the real application. In the next step, Progressive damage modeling was added to the stress analysis code, to provide a package for failure prediction for this case study.

This model can be utilized in the design process of the yoke to reduce the number of the required iterative experiments. The results showed the agreement between strain distribution obtained from the finite element model and the experimental results from strain gages and Digital Image Correlation (DIC). Also, a good correlation was observed between experimental tests and failure prediction performed through simulation. The results of failure analysis showed a good agreement with the experimental tests about the final failure load level, crack position on the surface, pattern of failure propagation inside the plate and dominant failure mode. In addition, the failure analysis will provide information about the failure initiation load level and the position of the first failed elements inside the plate.

Acknowledgement

Firstly, I would like to express my sincere gratitude to Prof. Suong V. Hoa for the continuous support of my Ph.D study and related research, for his patience, motivation, and immense knowledge. His guidance helped me in all the time of research and writing of this thesis. I could not have imagined having a better advisor and mentor for my Ph.D study. The door to Prof. Hoa office was always open whenever I ran into a trouble spot or had a question about my research or writing. He consistently allowed this thesis to be my own work but steered me in the right the direction whenever he thought I needed it. My sincere thanks also go to Prof. Rajamohan Ganesan for his unconditional valuable guidance and encouragement. Dr. Ganesan provided me with the tools that I needed to choose the right direction and successfully complete my dissertation

I would like to thank all my colleagues and members of Concordia Center for Composite (CONCOM) for their support. Specially, I would like to express my appreciations to Mr. Jeffery Simpson and Dr. Farjad Shadmehri. Their contribution in manufacturing and testing of the flexural thick composite beam is very much appreciated.

Technical support and comments from Mr. Elliott Schulte, Mr. Francois Landry, Mr. James Corrigan from Bell Helicopter, and Mr. Robert Fews from Concordia University during CRIAQ meetings are appreciated. Furthermore, I would like to acknowledge the support of this research by CRIAQ (Consortium for Research and Innovation in Aerospace in Quebec), NSERC (Natural Sciences and Engineering Research Council of Canada), and Bell Helicopter Textron Canada Ltd.

To end with, I would like to express my heartfelt gratitude to my father and my mother for their unlimited love and support through my whole life. Finally, to my beautiful wife, Sara, thank you for being the only support I have ever had, and I will ever be needing.

Dedication

This thesis is dedicated to:

My beloved parents

and

My beautiful wife, Sara

and

Melody.

Table of Contents

Table of Figures

Table of Tables

1 Introduction

Finding the optimum design for aerospace structures has been always a challenging endeavor since safety plays the most important role while designers tend to reduce the weight as much as possible. During centuries scientists tried to find appropriate materials, design and manufacturing processes to fulfill the requirements in the design and manufacturing of aero structures. Early biplane aircrafts structure (like Wright Flyer) were mostly constructed from wood frames and connecting wires. In the 1930s, the designers started to substitute wood with metal. The technics were well developed to manufacture thin metal sheets which assisted the designers to come up with the idea of a frame structure (consists of spars and ribs) and a closing thin skin. This idea is still the design base of the most conventional structures of the aircraft such as wing and fuselage.

A lot of efforts have been dedicated by the scientists to find an appropriate substitute for the conventional metals used in this industry such as aluminum and steel to introduce lighter and more fuel-efficient flying objects. The results of such an effort was creating and utilization of composite materials. High strength and high stiffness besides lower weight make them the most desirable choice for aerospace application. In addition, they have more design variables comparing to isotropic materials which provides design flexibility but also complexity. Although composite structures are growing fast in the aviation industry it should be considered that metals still have decades of background.

Up to now, studies have been focused on design, manufacturing and application of thin laminated composites because their structural behavior is less complicated compared to thick composites. Therefore, theories to analyze thin composites have been significantly developed. In addition, different methods have been very well adapted to their manufacturing for a variety range of application. Recently, improvements in manufacturing methods and equipment [1] lead the scientists' attention towards the design and analysis of thick laminates to make them suitable for specific industrial applications.

One of the applications of thick laminated composites in aerospace industry, is the yoke of helicopter. In general, the yoke has two sides, one is attached to the main rotor blade and the other is clamped to the mast using bolt joints. At present, the yoke is made of Glass Fiber Reinforced Polymers (GFRP). The schematic of the yoke is illustrated in Figure 1-1. Regarding the specific application described above, the most critical concerns during the design process of the yoke are as following:

The structure is subjected to the flexural bending due to aerodynamic loads.

The structure is subjected to centrifugal forces due to rotation of the blade.

The yoke is under the clamping loads of the bolt joins.

As the failure of the yoke will be catastrophic for the whole system of the helicopter and can cause the stall of the aircraft, it is of great importance to find the optimum design concept to satisfy both safety and weight requirements of this part. In the other way, manufacturing and testing of such a structure will induce high costs to the company. As a result, developing a model which can predict the structural behavior of the yoke in the design process will help the designers to narrow down their primary concepts and reduce the number of tests required in the design process.

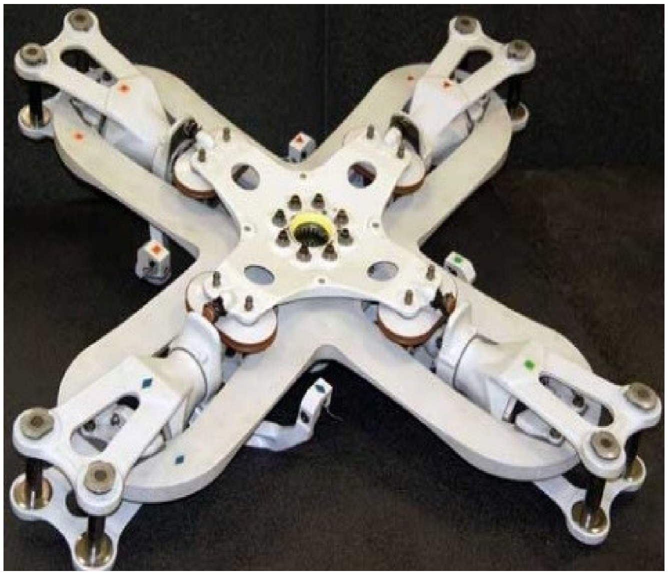

Figure 1-1: Schematic of the yoke in the rotor assembly (http://www.cadorath.com)

1.1 Model simplification

As described before, the yoke has a complicated structure which is subjected to various loadings during operation. Considering all including aspects to start the structural behavior simulation will be too complicated. In addition, the experimental validation of such a complicated model will require very advanced technologies. This study intends to introduce a feasible process for analysis of a thick composite plate when it is subjected to flexural bending and bolt joints simultaneously. The introduced model for the simplified plate, will be used by the industry to develop the required procedure for the analysis of the actual structure of the yoke. Figure 1-2 shows the simplified model versus the complete one.

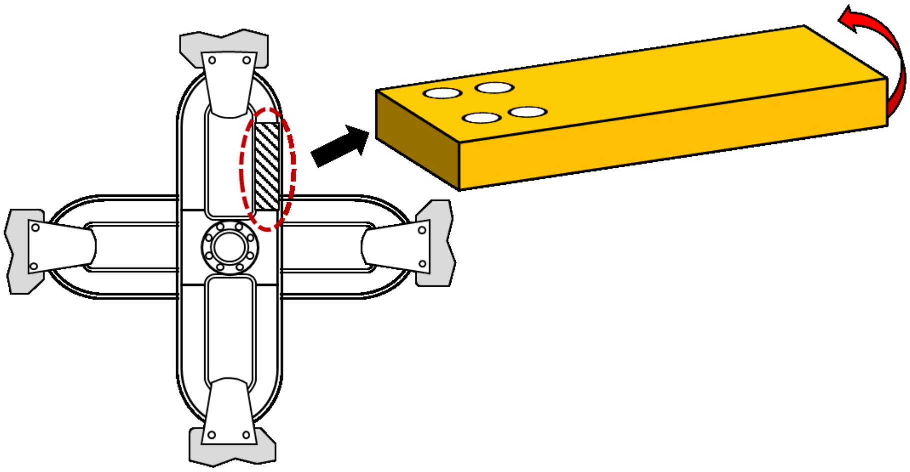

Figure 1-2: Schematic of the simplified model

1.2 Research Goals

The principal goal of this study is to introduce an effective method to study the structural behavior of thick laminated composite plate subjected to flexural bending under the boundary condition of the bolted joints. The results of stress analysis of thick composites will be combined with a progressive damage model (PDM) to predict the damage initiation and propagation in the part. In addition, the parametric finite element simulation provides the ability to study the effect of different parameters such as bolt and washer size, number of layers and layers orientation on the failure behavior of the yoke in different loading conditions.

To proceed step by step toward the final model, the project has been subcategorized into different phases:

1. Bolt joint in thick composites:

Finite element analysis of thick composite laminate in presence of the bolt joint.

FE modeling verification using Digital Image Correlation (DIC) and strain gages.

Study the effect of the thickness on the structural behavior of the plate.

2. Flexural bending of thick composites:

Finite element analysis of the laminate subjected to bending in presence of the bolt joints.

Verification using experimental methods such as Digital Image Correlation (DIC) and strain gages.

Thickness effect investigation in flexural bending model.

3. Failure analysis of thick composites:

Development of an adapted Progressive Damage Model (PDM).

Numerical and experimental failure analysis of thick composite subjected to bolt joint.

Numerical and experimental failure analysis of flexural model.

Investigation the effect of thickness on failure behavior.

1.3 Methodology

1.3.1 Numerical analysis

Finite element analysis (FEA) was selected as the numerical method for model development. It was desired to create a model which can provide the ability to perform further parametric studies. Therefore, a full three-dimensional parametric model was created in ANSYS using APDL programming language. The details of the parameter definition during the simulation process of different study cases will be discussed in future chapters. The basic parameters which are defined and controlled by the designer are listed below.

- Composite plate geometry (Plate width and length, the position and diameter of the bolt holes)
- Joint configuration (Washer inner and outer diameters, Bolt shaft and head sizes)
- Number of layers, layers thickness and orientation
- Material properties of all the parts of the assembly such as plate, washer, bolt, and buffer pads.
- Mesh sizing at critical areas
- Loading condition (Joints clamping force, Flexural bending maximum deflection and the rate of loading)
- Failure analysis parameters (Material degradation percentage and final failure criteria)

To build the finite element model Solid186 element has been used for both the homogenous and the layered parts. For composite laminates the solid element should be associated with a shell section in order to define orientation and thickness of each ply. The clamping torque is converted to the pretension force in the stud of the bolt and a pretension section has been created using elements Pret179 to apply this load. Finally, Conta174 and Targe170 elements are utilized on the mating surfaces to simulate contact. The number of total elements varies between different case studies [2].

1.3.2 Failure Investigation – Progressive Damage Model

The ultimate purpose of developing a verified finite element stress analysis was to provide a tool for failure investigation inside the plate. Finding the position of the crack initiation and the pattern of the propagation is a challenging endeavor in design process. The results of stress analysis should be incorporated into a suitable failure criterion to predict the failure behavior of the structure. Progress Damage Modeling (PDM) is selected to trace the failure propagation in the sample. To perform a PDM the first step is stress analysis to find the stress distribution in the part, then the failure analysis should be performed which provide the designers the critical spots in which the potential of crack initiation is higher. If some parts of the structure fail regarding the defined criterion then the process continues to the next step and if not, the load will be increased, and the process restarts again. In the situation at which some of the elements have failed, the material properties of those elements must be degraded. The material degradation scenario can be defined based on the failure mode and severity. At the final stage the part should be tested for the final failure. Because even if the part fails partially, it is possible that higher loads would be tolerable by the structure. Therefore, it is required to define a final failure criterion. The final failure can be defined based on the stiffness of the part or the degree of the propagation of the crack.

1.3.3 Experimental Tests

Any numerical simulation requires validation by some experimental tests to be considered reliable. In this study two parallel experimental investigations have been engaged to validate and rectify the finite element simulation process. First, strain measurement using strain gages and second, finding strain and displacement field at non- faying surfaces of the plate utilizing Digital Image Correlation (DIC) method.

Strain gages are very common tools to measure strain in structures. Here in this study different axial and T-Rosette gages are installed on the top surface of the plate and on the thickness side to find the strain in different positions and compare them with FEA data. A bolt equipped with a force transducer was incorporated to measure the pretension force in different clamping torques. This relation is a requirement for the joint simulation.

Digital Image Correlation (DIC) method has been utilized to find full field strain distribution pattern on the surfaces. DIC is a practical tool for in-plane and out-of-plane displacement measurements. The method is based on a comparison between digital images taken before and after loading. The whole process consists of three main steps: 1) preparing the specimen and imaging setup, 2) capturing images before and after loading and 3) image processing using computers. During the last step the DIC post processing software tracks the different node displacements during loading and interpolate the displacement field between these nodes to find the full displacement and strain field in the plane [26]. From the available displacement field, it is possible to calculate strain field.

1.4 Literature review

This literature review categorizes studies in two major subjects. First, the stress analysis in thick laminates without the joints has been reviewed and in the second part, the main focus is on bolted joints effect on structural behavior of composite laminates and the methods which are used to predict the failure based on stress analysis results.

1.4.1 Stress analysis of thick composites

By introducing composite materials as a desirable choice for aerostructures, the researchers dedicated a lot of effort to develop appropriate knowledge for design and analysis of the structures made from this type of materials. It is clear that composites have a more complicated behavior comparing with isotropic materials[3]–[5]. As it was previously mentioned, thin composite plates were the first generation of this type of materials in aerospace industry; hence design, test and analysis methods of thin composite parts have been very well developed so far.

In the literature several theories have been proposed for analysis of composite laminate[6]. Here the three most popular theories are reviewed. The first theory is Classical laminate theory (CLT). In this theory the field of displacement at any position along the thickness of the plate is a function of the displacement at the midplane. In this theory it is assumed that all the lines perpendicular to the plate remain straight and perpendicular to the mid plane after deformation. Therefore, transverse shear and transverse normal effects are totally neglected in this theory which makes it suitable for thin laminates[7]–[9].

The second theory is First order shear theory (FST). In this theory instead of neglecting of the transverse shear, a constant transverse shear is assumed along the thickness of the plate [10]–[12]. The plane stress assumption was applied on both CLT and FST theories. Consecutively, second or higher order deformation theories were developed for analysis of the composite plates [13]–[17]. It is difficult to find a physical meaning for higher order terms [6]. The third theory is called Layerwise theory. Although, in this theory, the displacement field is continuous through the whole thickness of the laminate, the derivative of the displacement with respect to the thickness coordinate can have some discontinuity along the thickness levels[6]. Layerwise theory is suitable for the structures made of thick composites [9], [18]–[20] and can be associated with finite element analysis.

For several years great effort has been devoted to the study of the composite structures manufactured using thin laminates. The significant amount of transverse normal and shear stresses along the thickness, makes the stress analysis in thick laminates more complicated in comparison with thin laminates, where plane stress assumption is applicable in most of the study cases [21]–[24]. So, two dimensional methods which have been developed so far[25]–[28], are not applicable to predict the stress behavior in laminates with higher thickness.

Finite element method has been widely used as the numerical method for stress analysis of the composite parts, either by using commercial packages as the computational tool or developing a new element and introducing different methods to calculate stiffness matrix. To validate the finite element model analytical solution or experimental tests were performed. Rao et al.[29] used a modified higher order bending theory to develop a finite element model in order to analyze thick composites with different layers sequences. Rao demonstrated close agreement with three-dimensional elasticity solution. Yildiz et al.[30] modeled a laminate using 8 node brick elements. To calculate the stiffness matrix of thick composites, the most challenging endeavor is finding the material stiffness matrix. In [30] two different averaging methods called arithmetic and weighted, were applied to find a global material matrix for a multilayered thick composite laminate. The results obtained from these two methods were compared with each other and with analytical solution results. Zimmerman et al.[31] utilized layered brick element of finite element MSC software to find the transverse normal and shear stress in a T-shape composite cross section with the thickness of 60 mm. The part is being used in aircraft landing gear assembly. Digital Image Correlation (DIC) and strain gages were the experimental methods to investigate strains and to validate the finite element simulation results.

In a study by Theotokoglou [32], finite element analysis was done using commercial software ANSYS to simulate the buckling behavior of thick laminated composite. The results were utilized to calculate the strain energy release rate due to different delamination scenarios, both in annular and axial directions. Hufenbach et al. [33] introduced an analytical method based on the first order shear theory to find the stress concentration in vicinity of a circular cutout in a thick laminated composite plate. This study showed the agreement between the results of the analytical method with both experimental tests and finite element. Kim and Hong [22] developed a finite element computer program based on a 16 node solid element to analyze a composite laminate with any number of layers and arbitrary layer sequences. This study showed that the interlaminar stresses at free edge are governed by layer orientation rather than laminate thickness. These studies indicate the popular approach in the literature for analysis of thick composite laminates. As a conclusion, the literature revealed that the layerwise theory combined with finite element analysis approach would be an appropriate method for stress analysis of thick composites which provide more accurate results comparing to other theories.

1.4.2 Bolt joint analysis

Aerospace structures are always consisting of several components which should be installed in the assembly using appropriate methods. When the structure has some composite parts, the design of the joint requires specific attention and has more complexity. The three common methods to install the composite laminates are: bonded joints, bolted joints and hybrid bolted/bonded joints. Since bolt joint is inspectable, repairable and undoable, it is more popular and practical. Some of the applications of bolt joints in aerospace industry are such as wing to fuselage joint in Boeing/MDD Harrier, Boeing/Bell V-22 Osprey, Boeing 777 and Grumman X-29 (NASA) [34].

Therefore, proper design of bolted joints is of great importance particularly for aerospace structures, where a balance between the minimum weight and desired safety factor should be reached. In the literature, studies mainly focused on the joint modeling and stress analysis of the joint [35], [36], investigation of the effect of different joint parameters on stress distribution and prediction of failure of the joint and the laminate [37]. In majority of research, the case study is a relatively thin laminate composite because of their wide range of application and less complicated modeling details. Recently, some researchers also introduced methods to investigate the stress in thick composite bolted joints. Thoppul et al. [38] did a review of the published research in the composite bolted joints until 2009. The topics have been classified in three major domains: first, the standards and methods for experimental tests of bolted joints in composites, second, design methodology, material selection and geometric effects and third failure in pinned and bolted joints.

Some studies are based on two-dimensional analysis of the laminate [39], [40] but it is shown by Ireman [41] that in vicinity of the bolt the stress field is three dimensional and significant interlaminar stresses exist at the free edges. This study proposed a three-dimensional finite element model with ABAQUS and validated the results with experimental tests done by strain gages. In an experimental approach by Khashaba et al. [42] the effect of washer size and bolt clamping torque on stiffness of the bolt joint was investigated. The results showed that in general, higher clamping torque leads to better stiffness of the joint because of higher contact pressure. Although higher contact pressure leads to stiffer joint but if the diameter of washer is smaller than a certain value, the high lateral compressive stresses beneath the washer will cause microscopic cracks around the hole edge, which can cause premature failure. Therefore, during the design process, a compensation between the joint stiffness and lateral compressive pressure caused by washer size should be taken into consideration.

In a study by Hsien-Tang Sun et al. [43], [44] a three dimensional finite element analysis was done to find the effect of clamping force, bolt stiffness and washer size on the structural behavior of composites and also failure of the joint. The simulation was done by ABAQUS, using three-dimensional layered brick elements. The contact between the washer and plate and bolt and hole is created using contact elements and the pretension load in the bolt is simulated by using thermal model. A progressive damage model was joined with the ABAQUS analysis. In this model a program written by the authors receives the results of stress analysis as input, then based on the desired failure criteria the program estimates the damage location and intensity and finally degrades the material based on the analysis. The results show, when the plate is subjected to in plane tension load, the lateral support of washer can prevent the bearing damages to spread laterally but when the crack grows outside that region it will propagate without any constraints. As the author concluded, the joint load sustainability increases by increasing clamped area.

The effect of joint parameters and stacking sequence on the bending behavior of a single lap composite joint was studied analytically by A. Olmedo et al. [45]. Sharos et al. [46] studied the effect of clamping force and bolt clearance on the force-displacement relation of a composite with single and multiple joints. McCarthy et al. [47] focused on measuring the tension force propagated in the shaft of the bolt due to clamping torque. This relation would be helpful as an input, for running finite element simulations. Finite element method was used by Wang et al. [48] to find the clamping torque and friction influence on the stress distribution in bolted T-joints composite which is used in ship industry.

The friction coefficient between clamping components plays a major role in stress distribution in the laminate during fastening the bolt (preload) and applying external load. Friedrich et al. [49] and Kim et al. [50] studied the friction coefficient in composite bolted joints and the affecting parameters such as lubrication and clamping torque. In another research done by McCarthy et al. [51] the effect of friction coefficient on contact stress distribution in composite bolted joints was investigated through several finite element simulations performed by MSC software.

Zolkiewski [52] reviewed the composite bolted joints strength test methods. The strain gages have been used to analyze the bolt joint effect in composite materials and results compared with a finite element simulation. Zhang and his collaborators [53] performed experimental tests and numerical finite element analysis on a single lap bolted composite-aluminum joint with three bolts to find the contribution of each bolt in carrying in-plane tension loads. The effect of the different bolt configurations was elaborated. Matuszewski [54] provided several guidelines, based on experimental tests, for selection of number of bolted joints and their configuration in composite materials. Several other researches were performed to analyze bolt joint composite plates. Majority of the previous studies were done using finite element simulation and experimental validation [55]–[60]. Also, several publications can be found in the literature that investigated the effect of different parameters on the structural behavior of a composite bolt joint [61]–[63].

In two studies by Cloud and his collaborators [64], [65], the strains beneath the washer were detected using Digital Speckle Pattern Interferometry (DSPI) method. To measure the strain beneath the washer, a transparent washer was manufactured from polycarbonate sheet. The polycarbonate washer should have the thickness of about 4.3 times of steel washer, to provide the same stiffness. The plate was a 0.5 inch thick laminate made of glass/epoxy. The results showed that even a small clamping force could reduce the stress concentration which occurred in the contact area between bolt and hole (due to pin tilting). Also, the strain behind the washer decreased up to 80%. The results obtained from DSPI and strain gaged installed at the surface, were in good agreement but beneath the washer there was not any data, to compare with DSPI.

In another research by Restivo [66], experimental methods using fiber optic strain gages and numerical simulation using ANSYS were utilized to find strain and stress distribution in a thick composite plate. The laminate was clamped to an aluminum plate using bolted joints. The laminate is made of 60 layers of E-glass/epoxy. To simplify the finite element analysis the orthotropic material property of the plate was measured using the tensile tests and both fiber optic and resistant gages.

1.4.3 Failure Analysis

Several publications have appeared in recent years studying the failure behavior and ultimate strength of the composite bolt joint. Different approaches were followed by researchers to study the effect of the engaging parameters on the bearing strength of single lap bolt joint [67]–[78]. Recently prediction of failure initiation and propagation in composite bolt joint subjected to static and fatigue loadings has attracted significant attention from research teams [79]–[91].

Lim et al. [92] studied the bolt joints effect on fatigue life of unidirectional laminates. The effect of different geometrical parameters on the fatigue failure of the laminate was investigated. The relation between the tension load in bolt shaft and clamping torque is found using an installed load cell. In the finite element model created by ABAQUS, the washer and the bolt have been modeled as rigid surfaces. The results revealed that the fatigue life of unidirectional laminate will increase if an appropriate clamping torque is applied.

Nassar et al. [61] focused on the effect of two bolt joints tightening condition on the failure behavior of composite plate when it is bolted to an aluminum or another composite plate. A progressive damage model is associated with finite element simulation for failure prediction. The numerical results were correlated with experimental tests. Also, in two other studies, by McCarthy et al. [93], [94] the effect of bolt clearance on the stress distribution, crack initiation and ultimate failure of multi-bolted composite structure were studied experimentally. They found that the clearance effect on crack initiation is more significant than its effect on ultimate failure.

Kradinov et al. [95] used genetic algorithm to optimize the strength of the joint. The design variables were laminate thickness, lay-up sequence and bolts configuration and size. The objective function was introduced based on the average stress failure criterion. Zhang et al. [96] investigated the bolt-hole interference effect on joint load capacity and they found that the maximum load capacity occurs at a specific interference. Liu and his team [97] worked on the finite element simulation of bolted joints in composites and modeling the damage using a user subroutine added to the finite element simulation.

In an experimental investigation by Pekbey [98], the geometric parameters such as and influence on the bearing strength was considered. Results showed that the hole-edge distance to hole diameter significantly affects the bearing strength of pin joints while width of the plate to hole diameter has a great influence on the mode of failure. Also, the authors suggested that the bearing failure can be considered as the desirable mode since it allows higher deformation and less brittle failure. Dano et al. [99] developed a finite element model to predict failure in bolted joints. They combined Hashin and max stress to introduce an appropriate criterion for failure analysis of composite joints. As it was shown by the results, agreement with experimental tests depends highly on selection of an appropriate failure criterion and proper definition of material degradation scenarios during progressive damage modeling.

Sergeev and his team [63] focused on the bolt spacing effect on the stress distribution and failure of the laminate. The utilized method was boundary condition collocation. As it is described by the author, in this method, a region with multiple internal boundaries will be segmented in to simple sub-domains and continuity of displacement components will be imposed at common boundaries. It was shown that the failure load is a function of joint geometrical configuration. Murri et al. [100] studied the tapered composite laminates fatigue behavior. A finite element model was developed to predict the delamination in the tapered composite subjected to cyclic loads. As it is mentioned by the author, delamination intended to initiate at the tapered region.

However, to the author’s best knowledge, in term of the stress analysis, very few publications are available in the literature that address the bolt joint analysis in a composite with a high thickness of about 0.75 inch. In addition, most of the studies were devoted to the single lap bolt joint under tension force. Nevertheless, there are still some relevant and interesting problems when clamping force of the joint is the only loading case. The failure of thick composite plate due to joint clamping force is one of the subjects which has been scarcely investigated in the literature.

Although, single lap bolt joint covers a wide variety of the applications, the yoke of the helicopter requires investigation of the thick composite bolted laminate under flexural bending which is not addressed by the previous researchers. Finally, it would be of great importance to predict the failure of the thick composite plate considering all the mentioned features.

This research concerns itself with the stress analysis and failure prediction in a thick composite laminate subjected to both bolt joints and flexural bending loads. Both numerical and experimental methods are used to perform stress analysis and the results obtained from stress analysis will be utilized to find the critical locations for crack initiation and the pattern of crack propagation. The results of this research can be used by the yoke designers, in order to narrow down their design space and reduce the number of iterative experimental tests.

2 The effect of the bolt joint

2.1 Bolt joint modeling methods

The literature review showed that the previous studies did not concentrate on the effect of the bolt joint itself for structural behavior of thick composite laminates. Since the bolt joints play the major role in the assembly of the yoke of helicopter and the joints are prone to failure, the bolted joints are included in the simplified model. Therefore, in the first phase of this study, the effect of bolt joint (without considering any external loading) was investigated. The main goal was to study the bolt joint and introduce a reliable model which can simulate the behavior of the bolt joint in thick composite plate. As described before, the main case study was a thick rectangular plate which consisted of 80 unidirectional layers of Glass/Epoxy. The plate has four holes at each side. The geometry of the plate is shown in Figure 2-1.

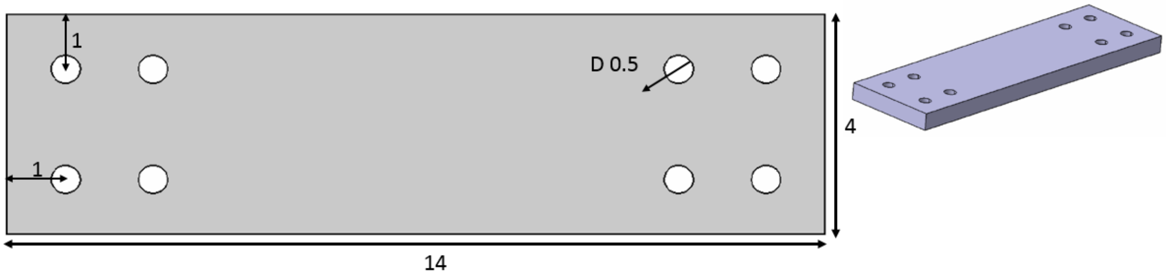

Figure 2-1: Geometry of the case study (Dimensions are in inch)

In the literature different methods are introduced to model a bolt joint [36]:

1. The bolt and the washer were not included. The applied load due to pretension is simulated as uniform pressure on the contact area between washer and plate.

2. In this model, the shaft of the bolt was simulated by a cylindrical rigid shell to prevent negative radial displacement of the points located on the hole inside area. Contact is considered between the hole and the rigid cylinder areas.
3. The washer was included in this model and the load is simulated as the uniform pressure on the contact area between bolt head and the washer. In addition, the shaft of the bolt is modeled as a solid cylinder.
4. All parts (bolt, washer and plate) are included in this simulation. The bolt and the washer are modeled as a single part, so the contact between bolt head and washer is not considered. The load is applied as a uniform pressure on the bolt head.
5. This model has the same characteristics as number 4, except that the load is simulated by creating pretension elements in the shaft of the bolt.
6. The loading is modeled by pretension in the shaft of the bolt. In addition, the bolt and washer are modeled as separated parts and the contact between bolt head and washer is being taken to account.

Table 2-1 summarized the characteristics of each of the above methods. The main goal of the first phase of this study is to provide an accurate finite element simulation method for bolt joint which would be utilized in the next phase to model the flexural bending in presence of the joints. Since the clamping pressure of the bolt joints varies by application of the bending moment, models 1 to 4 which consider the uniform pressure distribution are not applicable here. In addition, the results obtained from methods 5 and 6 showed that the contact pressure distribution between the plate and the washer is not uniform, even without any bending moment. In the first phase of study which concentrates only on the effect of bolt, method number 6 which includes more detailed features was selected.

Table 2-1: Summary of the modeling methods

Method Number	**1**	**2**	**3**	**4**	**5**	**6**
Model	(P, PH)	(P, PH) BS-R	(P, PH) BS-R W	(P, PH) (BS, BH, W)	(P, PH) (BS, BH, W)	(P, PH) (BS, BH) W
Load	Uniform pressure on plate	Uniform pressure on plate	Uniform pressure on washer	Uniform Pressure on Bolt Head	Pretension across the bolt stud	Pretension across the bolt stud
Load Schematic	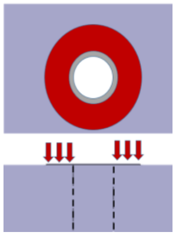		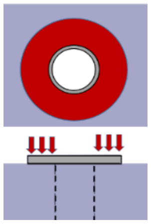	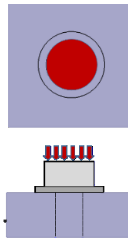	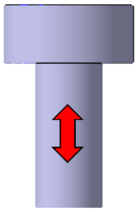	
Contact Definition	-	PH-BS	PH-BS W-P	PH-BS W-P	PH-BS W-P	PH-BS W-P BH-W
P: Plate, PH: Plate Hole, BH: Bolt Head, BS: Bolt Shaft, W: Washer, R: Rigid (P, PH) means that two components are modeled as one part.						

2.2 Numerical analysis (Finite element model) of bolt joint

For the first phase of the project, the finite element model included only the effect of one bolt joint, as it is indicated in Figure 2-2. The element 'Solid 186' was used to model all different parts. Solid 186 is a three-dimensional solid element which consists of 20 nodes and each node has three degrees of freedom which are displacements in three perpendicular directions [2]. Since this element can be used to model both homogenous and layered structures, the composite plate, steel washer and bolt were all modeled using that same element but with different options for each part. To model the composite plate, solid element has to be associated with a section to define the number of layers and each layer thickness and fiber orientation. Refer to Appendix A, for the details of Solid 186. Figure 2-3 shows the schematic of homogenous and layered SOLID186 element.

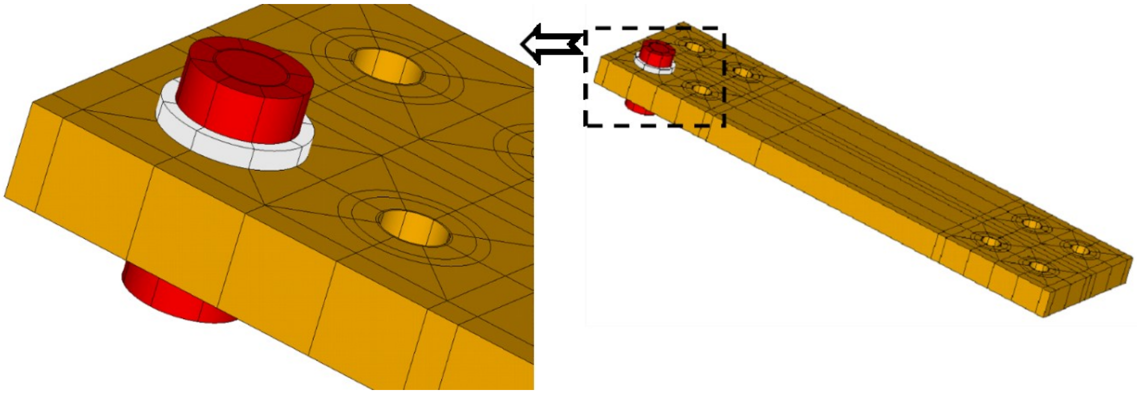

Figure 2-2: Finite element model for bolt joint

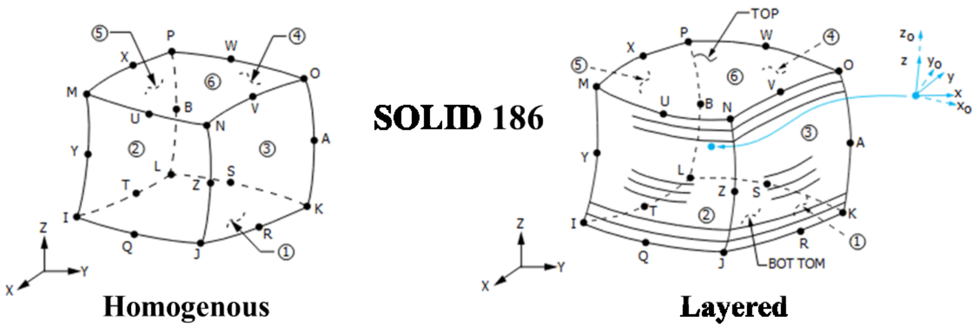

Figure 2-3: Homogenous and layered SOLID186 element [2]

As it is indicated in Table 2-1, there are several contacted areas for model number 6. TARGE170 and CONTA174 elements were utilized to define contact at corresponding areas. CONTA174 is used to represent contact and sliding between three-dimensional target surfaces and a deformable surface defined by this element. TARGE170 is used to represent various three-dimensional target surfaces for the associated contact elements [2]. Figure 2-4 shows the schematic of CONTA174 and TARGE170. As it is indicated in Figure 2-5, surface to surface frictional contact has been defined in the following regions:

- Between bolt head and washer
- Between washer and plate
- Between plate hole inside area and stud of the bolt

In order to increase the accuracy of the contact simulation and reduce the time required for convergence of the nonlinear contact analysis, a similar mesh pattern and sizing were created in the contacted areas. Figure 2-6 shows the generated mesh for different parts of the model.

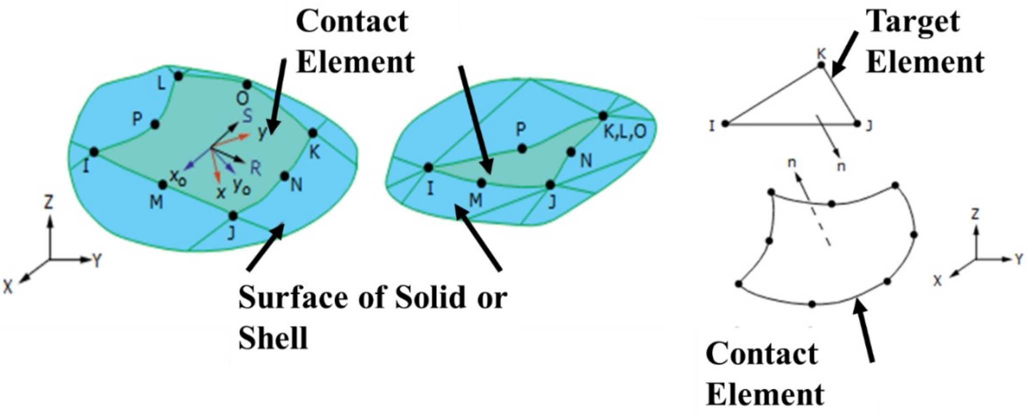

Figure 2-4: TARGE170 and CONTA174 elements [ANSYS Help]

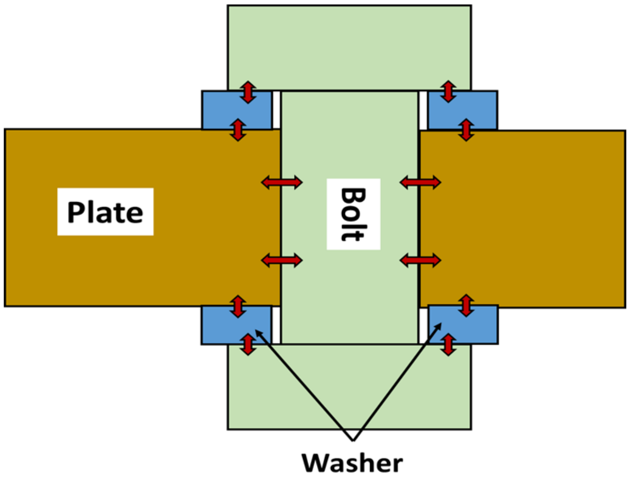

Figure 2-5: Surface to surface contact definition

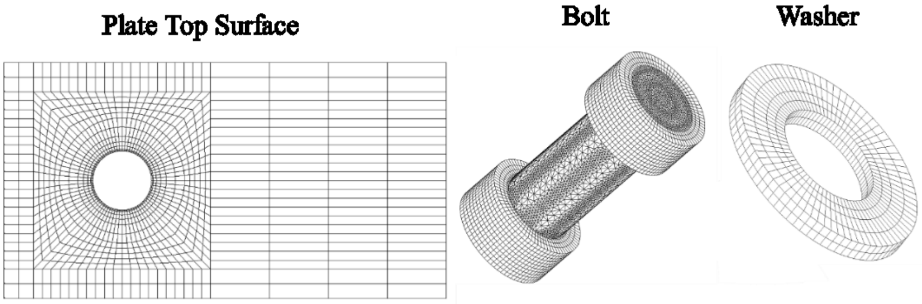

Figure 2-6: Meshing Pattern-Primary model (The parts do not have the same scale)

Since Solid186 does not have rotational degree of freedom, it is not possible to apply the clamping torque directly to the bolt head. Instead of the clamping torque, the corresponding tension force generated in the stud of the bolt should be applied. It is required to create a pretension section to model the bolt preload in ANSYS. A pretension section was created in the mid-length of the bolt shaft. The nodes of the elements located at the pretension section can collapse into each other, since the two ends of the bolt are axially constrained by the washers at the top and bottom of the plate, the total length of the bolt shaft will experience a tensional stress as what happens in real case during bolt tightening.

Since the only available information was the clamping torque which is applied on the bolt head, it was required to utilize a technic or formulation to convert the torque to the tension load in the stud of the bolt. Therefore, for the first approach, a formulation introduced by Speck [101] was utilized. Based on this formulation, the load can be obtained using Equation 2.1, where T is clamping torque, D is bolt shaft diameter and K is friction coefficient. K is suggested by Speck to be considered 0.2 for steel bolts. During experimental tests, this force is measured using a strain gage installed on the shaft of the bolt and the result was compared to the calculations. This process is explained in the following section.

$$F = \frac{T}{KD} \qquad \text{Equation 2.1}$$

2.3 Bolt preload - First experiment

This part of experiments focused on finding the relationship between bolt clamping torque and pretension force. The results of this experiment were utilized to provide similar loading situation during simulation and experiments. Figure 2-7 shows the configuration of the washer and bolt which were used for the first experimental investigation. As illustrated in this figure, the diameter of the bolt shaft was selected smaller than the hole diameter, since enough space should be provided for the strain gage wires around the bolt shaft. According to the selected bolt size, the chosen washer had an inner diameter less than the hole diameter. The inner diameter of washer was $\frac{11}{32}$ inch when the hole diameter is 0.5 inch. It will be shown later that this washer and bolt selection had a significant effect on the results.

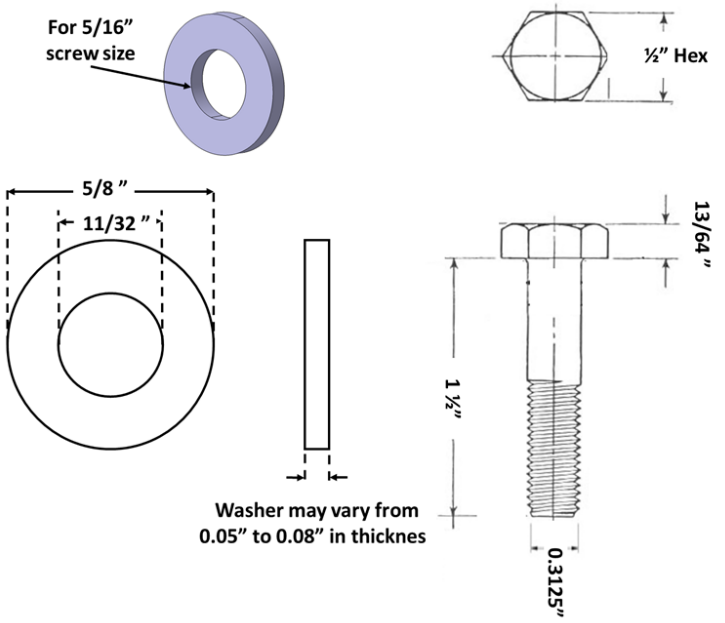

Figure 2-7: First experiment, bolt and washer specification (Parts are not to scale)

Figure 2-8 shows the axial strain in the stud of the bolt during the test process. Also, the applied clamping torque at each period is indicated in this figure. It was expected that higher clamping torque produces higher tensional strain, but as it is illustrated in the figure, at some regions by applying more torque the tension in the stud of the bolt decreased. This unexpected behavior is due to high conical deformation of washer which was observed during experiment. Since the inner diameter of washer was smaller than the hole diameter, the washer was not fully supported by the plate beneath that. Therefore, it underwent a conical deformation which totally changed the contact behavior between plate and washer and affected the tension preload in the bolt. The significant drop of strain at the final stage was due to the bolt failure.

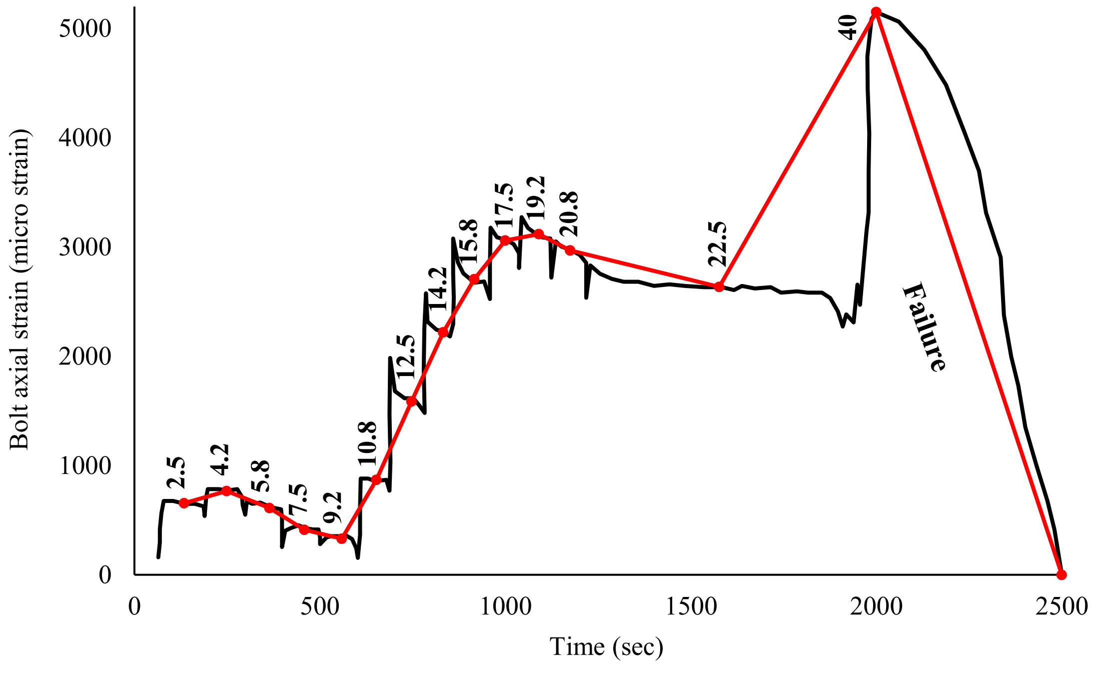

Figure 2-8: First experiment, Bolt pretension vs clamping torque

(The numbers on the graph represent clamping torque in lb-ft)

From first bolt preload experiment, it was realized that some important concepts should be reconsidered and improved to obtain a more accurate simulation results and experiment test data. These important points can be summarized as:

- To install the strain gage on the shaft of the bolt, it was required to make a lateral hole to pass the strain gage wires which made the bolt weaker. Based on the yoke application it is recommended to apply 110 lb-ft of clamping torque while in this experiment the bolt failed at 40 lb-ft. Figure 2-9 shows the failed bolt. As it is obvious from Figure 2-9, the bolt failed at the position of the drilled hole for strain gage installation.
- Using a bolt with a diameter smaller than the hole diameter was obligatory because enough gap between bolt shaft outer surface and hole inner surface should be provided for the strain gage installation. This also made the load capacity of the joint less than what was required.
- Since an appropriate washer should be matched with the bolt size, the inner diameter of the selected washer was smaller than the hole diameter. This phenomenon caused high conical deformation of the washer which changed the contact behavior between washer and the plate. As a result, the strain in the stud of the bolt dropped during several periods of the test.

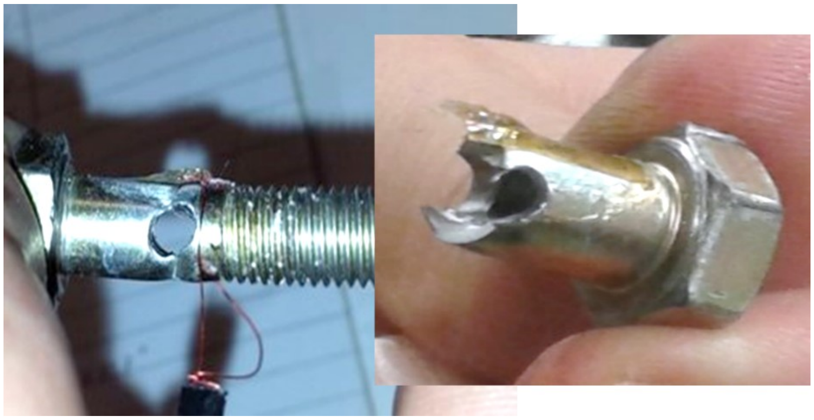

Figure 2-9: Failure of the bolt at 40 lb-ft of clamping torque, first experiment

To improve the reliability of the experiment results it was decided to utilize a ½ inch bolt which was equipped with a calibrated force transducer. The new bolt was associated with washers with inner diameter bigger than the hole diameter. This combination was called bolt preload second experiment.

2.4 Bolt preload - Second experiment

In the previous experiment a strain gage was installed manually on the stud of the bolt in order to find the pretension force, so it was required to use a bolt with a diameter smaller than plate hole which caused bolt failure at a clamping torque much lower than it was expected. The suggested torque from the supplier is 110 lb-ft and the last small bolt failed at about 40 lb-ft. To resolve this problem the bolt was replaced by a 0.5 inch bolt which has an installed force transducer inside its shaft. The bolt was provided by StrainSert Company. The data of the new bolt made it possible to read the bolt pretension load in different clamping torques directly and there was no need to convert the strain in the bolt to axial load. Figure 2-10 shows the bolt that was used previously and the one utilized for the second experiment.

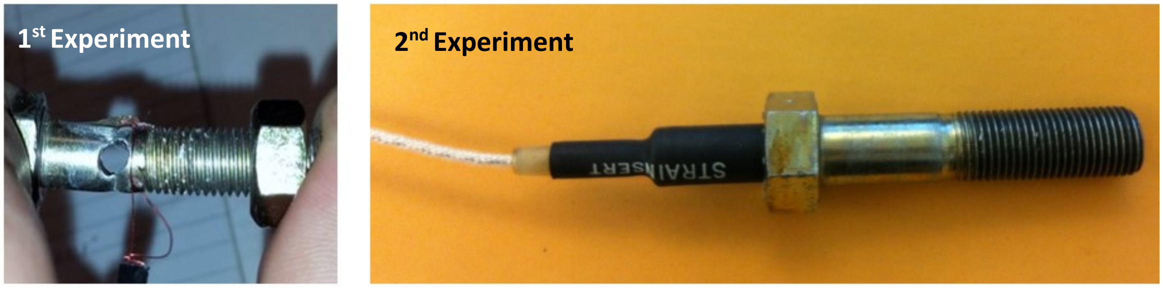

Figure 2-10: Comparison of the bolts utilized in the first and second experiments

To prevent high conical deformation of the washer and to match the washer and bolt sizes, the washer was replaced with a new one which had an inner diameter bigger than the hole diameter. The inner and outer diameter of the washer used for second bolt experimental tests were $\frac{17}{32}$ and $\frac{11}{16}$ inch respectively. In addition, the boundary condition (fixing method) was changed between first and second investigation. In order to apply the clamping torque, it is required to fix the plate at a distance far from the bolt joint (it is desired that fixing forces do not have any effect on the bolt joint). For the first experiment, the plate was fixed to the working table by two hand clamps while for the second set-up the other end of the plate was fixed to a rigid heavy steel beam using four bolt joints. The steel beam was a part of the flexural bending testing machine which will be explained later in detail. Observations revealed that the second test-set up provided a better fixing condition for the plate. Figure 2-11 compares the fixing method between two trials.

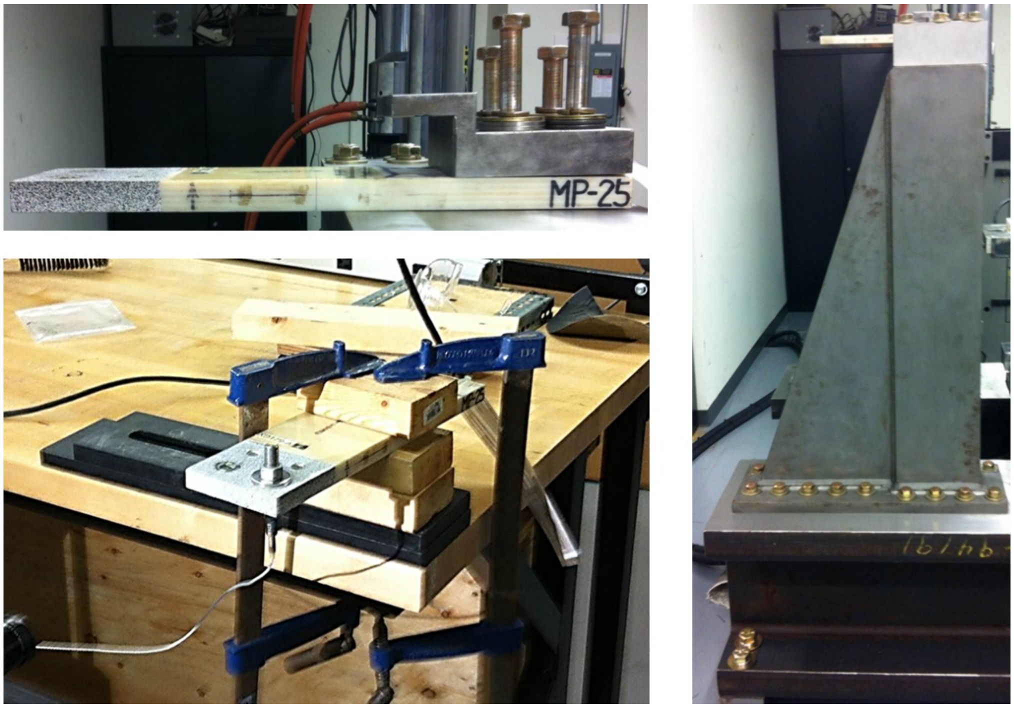

Figure 2-11: Comparison of fixing method between first and second bolt experiments

The bolt preload during the second experiment is shown in Figure 2-12. As it was expected applying a higher clamping torque increased the tension force. A closer look at this figure reveals that at the very first few seconds of each torque increment step, the force raised to a high level, but it decreased until reaching a steady value. This tension release varied between 5% to 15 % and it was higher at higher clamping torques. This behavior illustrates the viscoelastic reaction of thick composite laminates when subjected to bolt clamping forces. Right after applying a higher torque, the plate shows a higher resistance against deformation which will cause higher tension in the bolt stud. After a few seconds the washer pushes the material away in radial direction since the material beneath the washer is softer than the material above that. As a result, the material beneath the washer radiates away from the clamped area and resistance against deformation will decrease. As a consequence, bolt releases its tension up to some point. This behavior is highlighted for the clamping torque of 90 lb-ft in Figure 2-12.

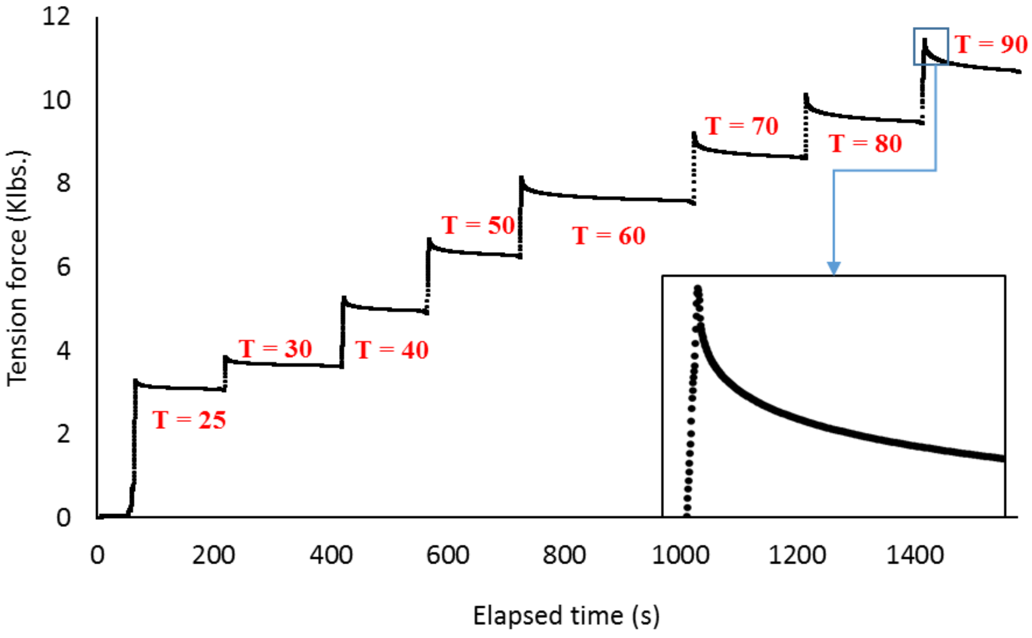

Figure 2-12: Bolt preload vs elapsed time – Second experiment

(Numbers on the graph represent clamping torque in lb-ft).

To highlight the significant viscoelastic behavior of the composite plate, the sample made of 80 unidirectional layers of glass/epoxy has been compared with an aluminum plate with the same configuration while they were both subjected to the same bolt load. Figure 2-13 identifies the difference in the relaxation of the bolt tension between aluminum and composite plate at the clamping torque of 90 lb-ft. As it can be seen in Figure 2-13, for the composite laminate, higher tension was produced in the bolt when the aluminum plate released the tension with a faster rate. The reduction in the force until reaching the steady value was 12.5 % for composite plate and 5.3% for the aluminum one.

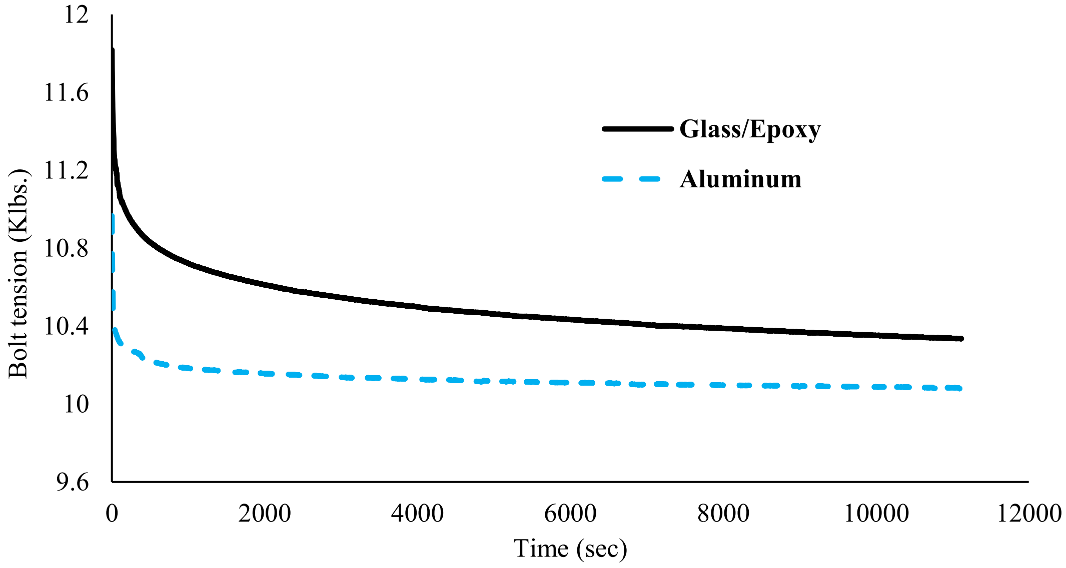

Figure 2-13: Comparison of viscoelastic behavior between plates made of glass/epoxy and aluminum at the bolt clamping torque of 90 lb-ft.

To obtain a value for bolt preload corresponding to each clamping torque, the test was performed while the load was monitored continuously during the whole test process. After application of each clamping torque, enough time was given to the bolt to reach a steady value of preload. This steady value was selected as the torque corresponding pretension force. Figure

2-14 illustrates the pretention force versus the clamping torque for three different maximums of applying torque. As it is illustrated in this figure, a linear relation was obtained with a good approximation. Based on the results, the friction coefficients (K, refer to Equation 2.1) obtained from these three experiments were 0.197, 0.194 and 0.195. The average of these values was used to calculate bolt tension load at any clamping torque desired for finite element analysis.

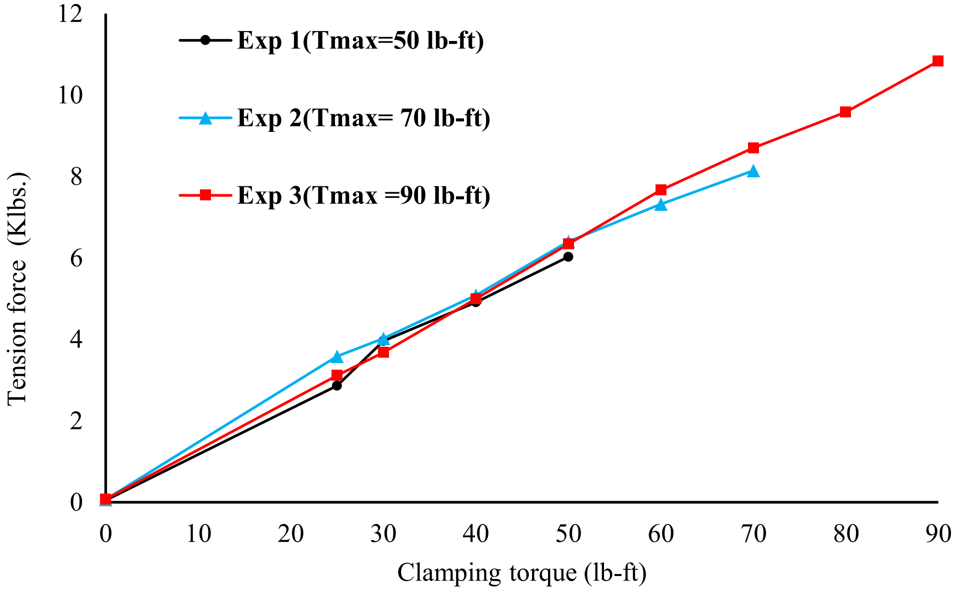

Figure 2-14: Bolt pretension vs clamping torque for the maximum torque of 50, 70 and 90 lb-ft.

2.5 Bolt analysis - Contact definition

As the main source of loading is the bolt joint, one of the major concerns during the finite element simulation was the definition of the contact in different regions. Especially the contact between composite plate and steel washer had the most significant importance. To find the friction coefficients between steel and glass epoxy, a simple friction test was done and based on the obtained results, a friction coefficient of 0.3 was selected for contact definition between the washer and the plate.

Since all parts of the system are statically in equilibrium, the pretension force in the bolt shaft should be equal to the contact force between washer and the plate. Therefore, the contact pressure between the washer and the plate was integrated over the washer area and compared to the pretension force in the bolt. At the bolt preload of 8750 lb. the contact force between washer and the plate (calculated by contact pressure integration) was 8690 lb. which represents less than 0.7% of difference. This difference could be due to the friction between bolt stud and the inner wall of the hole. This friction force can collaborate with the contact force to cancel the force applied to the washer by bolt head. Figure 2-15 shows the free body diagram of the washer and the bolt.

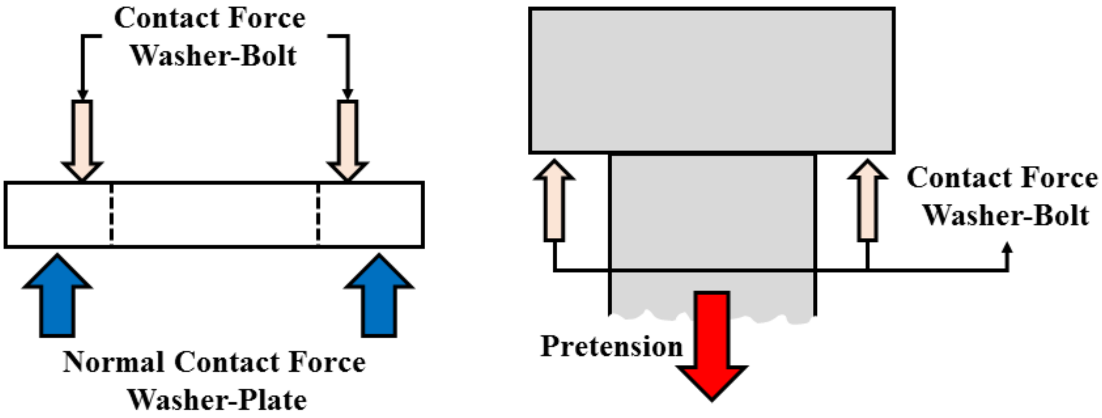

Figure 2-15: Free body diagram of bolt and washer

2.6 Bolt analysis - Material

The material of the plate was provided by Cytec Engineered Materials (FX E773/S-2 Glass). Since a range of values was proposed by material supplier for each property, a series of experimental tests was performed by Hamidi [102], to obtain the properties of the available material. The results of experimental tests are presented in Table 2-2. Comparison between the values obtained during experiment and some data provided by the manufacturer showed good agreement. For the unknown material properties, the typical data available in ANSYS Workbench 16.5 material library for S-Glass/Epoxy were utilized. Table 2-2 summarizes all the available properties from three different sources: ANSYS, experiment and supplier.

Table 2-2: Material properties for plate from three different sources [102], [103]

(Modulus are in Msi and Strengths are in ksi)

Modulus	ANSYS	Experiment	Supplier	Strength	ANSYS	Experiment	Supplier
E_1	7.25	7.2	7 - 9	σ_{11T}^{S}	246	247.7	250-280
E_2, E_3	1.16	1.86		$\sigma_{22T}^{S}, \sigma_{33T}^{S}$	5.1	8.88	
G_{12}, G_{13}	0.72	0.62		σ_{11C}^{S}	145	139	170-190
G_{23}	0.56			$\sigma_{22C}^{S}, \sigma_{33C}^{S}$	17.4	20.14	
V_{12}, V_{13}	0.3	0.28		$\tau_{12}^{S}, \tau_{13}^{S}$	11.6	15.7	
V_{23}	0.4			τ_{23}^{S}	6.7		

2.7 Bolt analysis - Strain gages

The finite element model accuracy has been verified by using two experimental approaches. In the first approach, strain gages were installed around the washer at the top surface and along the thickness of the laminate. These gages measured the strain along the fiber direction and transverse to them. Six tee rosettes strain gages (Vishay WK-06-030WT-120) were installed using M-Bond 200 Adhesive from Micro-Measurements Company. The positions of the gages were selected according to the critical points obtained from finite element analysis (where the maximum and minimum strains along fibers and in transverse directions appeared). Figure 2-16 shows the position and orientation of the strain gages.

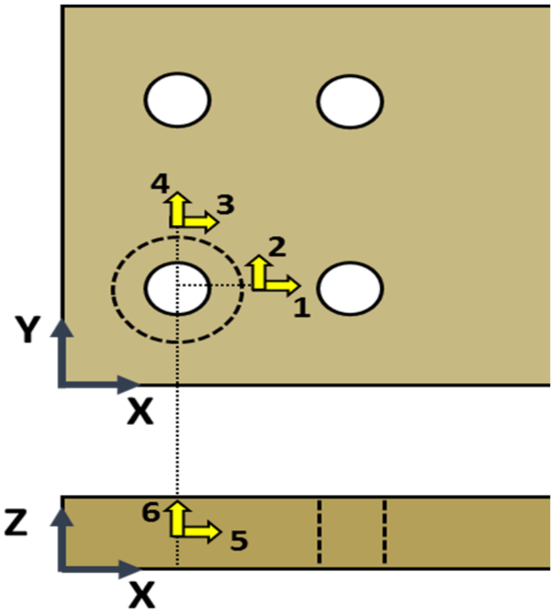

Figure 2-16: Position of installed strain gages – bolt effect investigation

Gages 1, 3 and 5 measured the strain in X (Fiber) direction and gages 2 and 4 measured the strain in Y (transverse) direction. The gage number 6 was placed to measure the strain along Z (thickness) direction. Although it was found from finite element analysis that the critical points were located at the edge of washer on the top surface, but the gages were installed considering a gap of 5 mm from the edge of the washer during experimental investigation, to prevent any damage to the gages and to provide enough space for installation. Therefore, the center point of the gages 1 to 4 were positioned at the radial distance of 0.825 in (21 mm) from the center of the hole. Gages 5 and 6 were positioned on the side surface, at the mid thickness and along the central axis of the hole. As it was mentioned before, a special bolt with an installed transducer gage was utilized to record the pretension of the bolt. The test was duplicated by using several clamping torques that varied between 25 to 70 lb-ft.

2.8 Digital Image Correlation

Digital Image Correlation (DIC) method was utilized to find strain distribution pattern around the hole on the top and side surfaces. DIC is a practical tool for full-field in-plane and out of plane strain investigation. This method is based on comparison between digital images taken before and after loading. The whole process consists of three main steps:

1) Preparing the specimen and imaging setup.

2) Capturing photos before and after load application.

3) Image processing using computer.

Digital Image Correlation method needs a properly and densely speckled sample. An airbrush was used to create the pattern. The density of the color and spraying pressure were found through several trial and errors. Based on the information provided by the DIC system supplier, the speckles should be at least 5 pixels in size and 5 pixels in spacing. However, the software does not track the actual speckle pattern but it assigns a mesh of "subsets" across the image. It is desired to have a unique speckle pattern within each subset. The software will assign a unique point to each subset and track that point for analysis. The larger a subset is, the more information it will contain and the more unique each will be. The more unique the subsets are from subset to subset, the better confidence will be achieved [104]. The Stepsize is the distance between adjacent subsets. Therefore, the subsets will have some overlaps and they will not be independent of each other. The DIC system was provided by Correlated Solution and they recommend having the Stepsize of one quarter of the subset.

The last parameter which should be considered here is filter size for strain calculation. In a simple explanation Stepsize × Filter size would be the size of the virtual strain gage utilized for strain calculation. It is mandatory to take into consideration the meshing size for finite element simulation and the settings for strain calculation during DIC process when the comparison between these two methods is being performed. As Figure 2-17 shows a speckle pattern was created on the desired surface using paint spray. Cameras with the resolution of 59 mega pixels were used to capture images. The resolution of images was 289855 dpi and the field of view was 3.1 × 2.6 in^2.

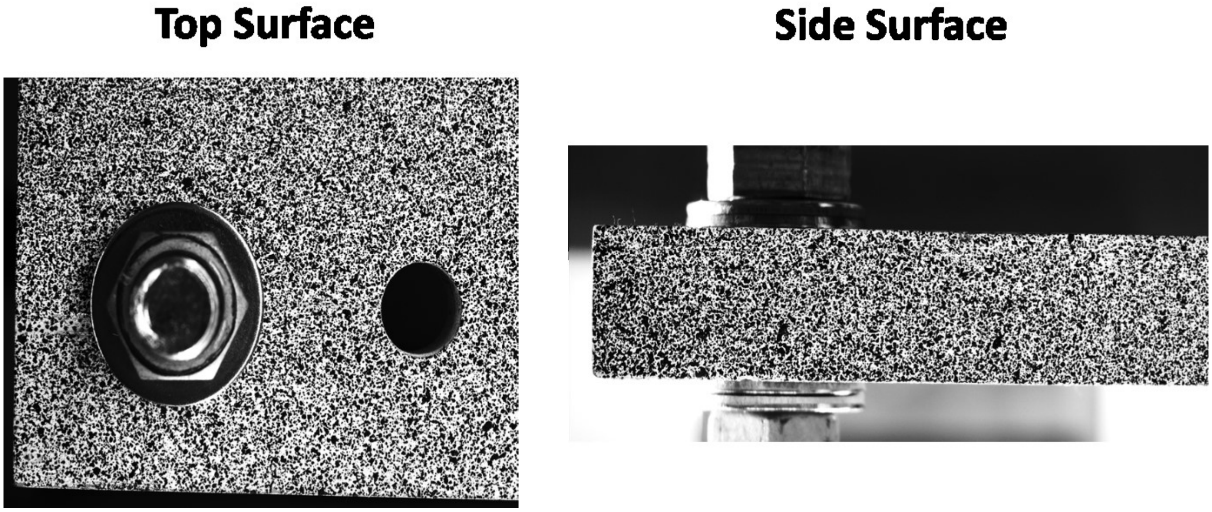
Top Surface

Side Surface

Figure 2-17: The speckle pattern washer on top and side surfaces

It is illustrated in Figure 2-18 that two cameras were installed for the upper surface and along thickness. As it was described before the other end of the plate was fixed to the heavy steel beam of the machine which was designed for flexural test (refer to Figure 2-11). The strains measured by strain gages and DIC were recorded at different clamping torques that varied between 25 to 70 lb-ft. The test did not perform at 110 lb-ft. of clamping torque which was the industrial partner recommendation to avoid any damage to the utilized bolt or the sample.

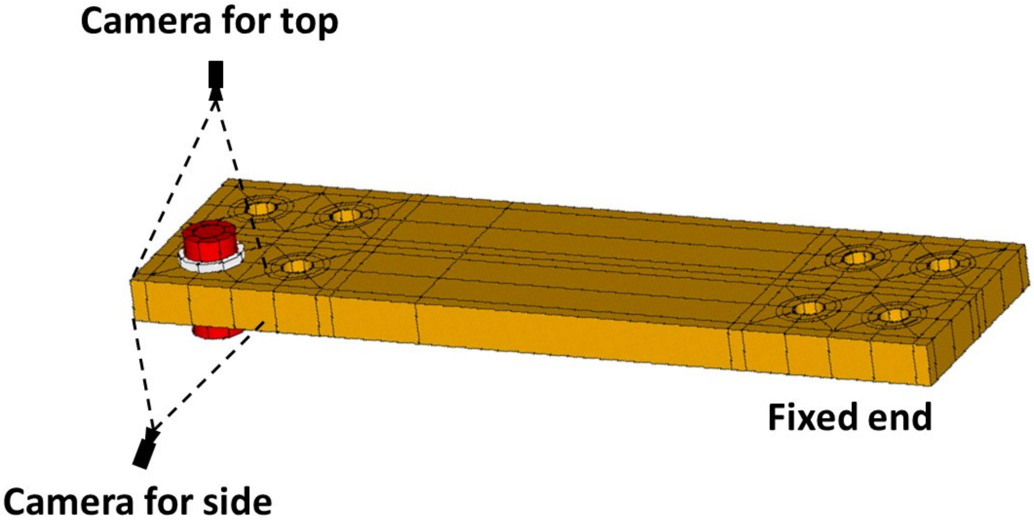

Figure 2-18: Schematic of Cameras set up for the effect of bolt joint investigation

2.9 Bolt analysis - Results

2.9.1 Bolt analysis - Strain gages vs FEA

Figure 2-19 illustrates the results obtained from strain gages installed at positions 1 to 6 (refer to Figure 2-16) for the clamping torque of 25 to 70 lb-ft. Results show that for all clamping torques the axial strain in position 1 is higher than the same strain at position 3. In the other hand, it can be observed that gage number 4 recorded higher lateral strains in comparison with gage number 2. In general, it could be concluded that lateral strains at the surface are higher comparing to axial strains (G2 > G1 and G4 > G3). This was expected since the plate is unidirectional, and the material is stronger along fibers rather than perpendicular to them. Gages 5 and 6 measured strains on the plate thickness. Since bolt clamping force is applied along the thickness of the plate and the plate is unidirectional, the strain along the thickness (gage 6) was higher compared to the axial strain (gage 5). Since no sign of failure was observed up to the clamping torque of 70 lb-ft, the relation between clamping torque and recorded strain were linear for all gages.

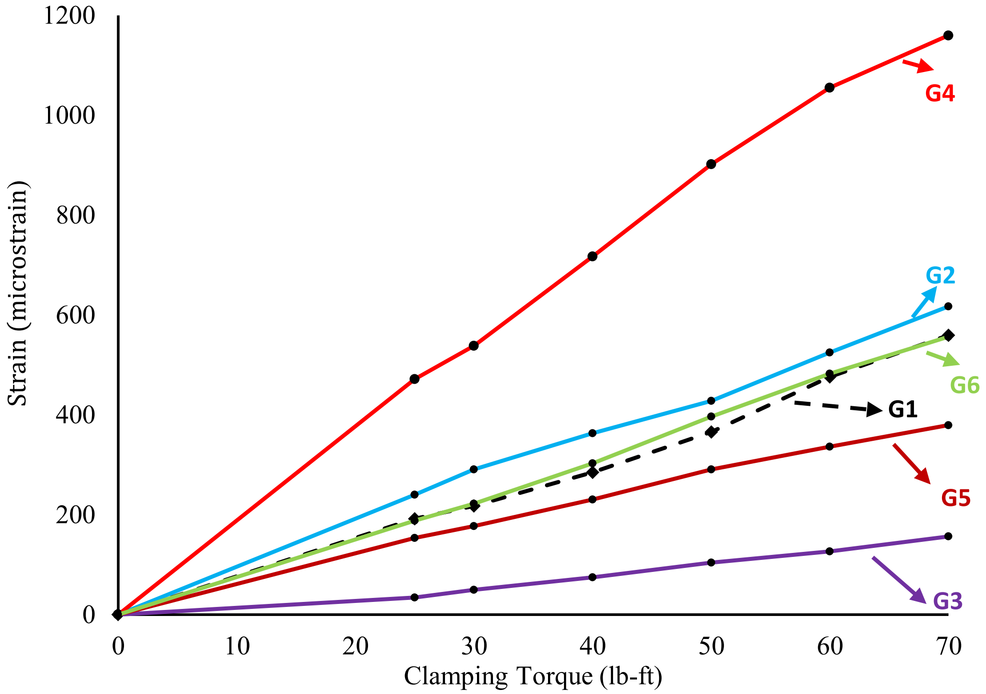

Figure 2-19: Strain gages data for the clamping torque of 25 to 70 lb-ft of the bolt joint

Figure 2-20 compares strains obtained from gages with the strains calculated by the finite element simulation. For gage number 1 (G1), maximum difference between experimental and finite element was 9% (35 micro strain) at clamping torque of 50 lb-ft. Since the sensitivity of the utilized gages was 50 micro strain and the maximum error was 35 micro strain, it can be concluded that FEA and gage values correlated very well at this position. The same investigation for gage 2 (G2) showed a maximum difference of 9% (55 micro strains) at the torque of 70 lb-ft which again represents the good correlation between results obtained at the position of gage 2. For gage 3 (G3) the amount of strain was not considerable comparing to the other positions. Although the maximum difference between experiment and FEA was 35%, it was only 35 micro strains which is less than the gage sensitivity. For gages 4 (G4) and 6 (G6) the maximum difference was less than 5% (40 micro strains) and finally for gage 5 (G5), the difference was 20% (35 micro strains). All the results revealed that the maximum difference between strain gages and finite element analysis was in the order of the gages sensitivity or less than that. This fact shows that the finite element simulation has a good accuracy in strain prediction within the gage sensitivity.

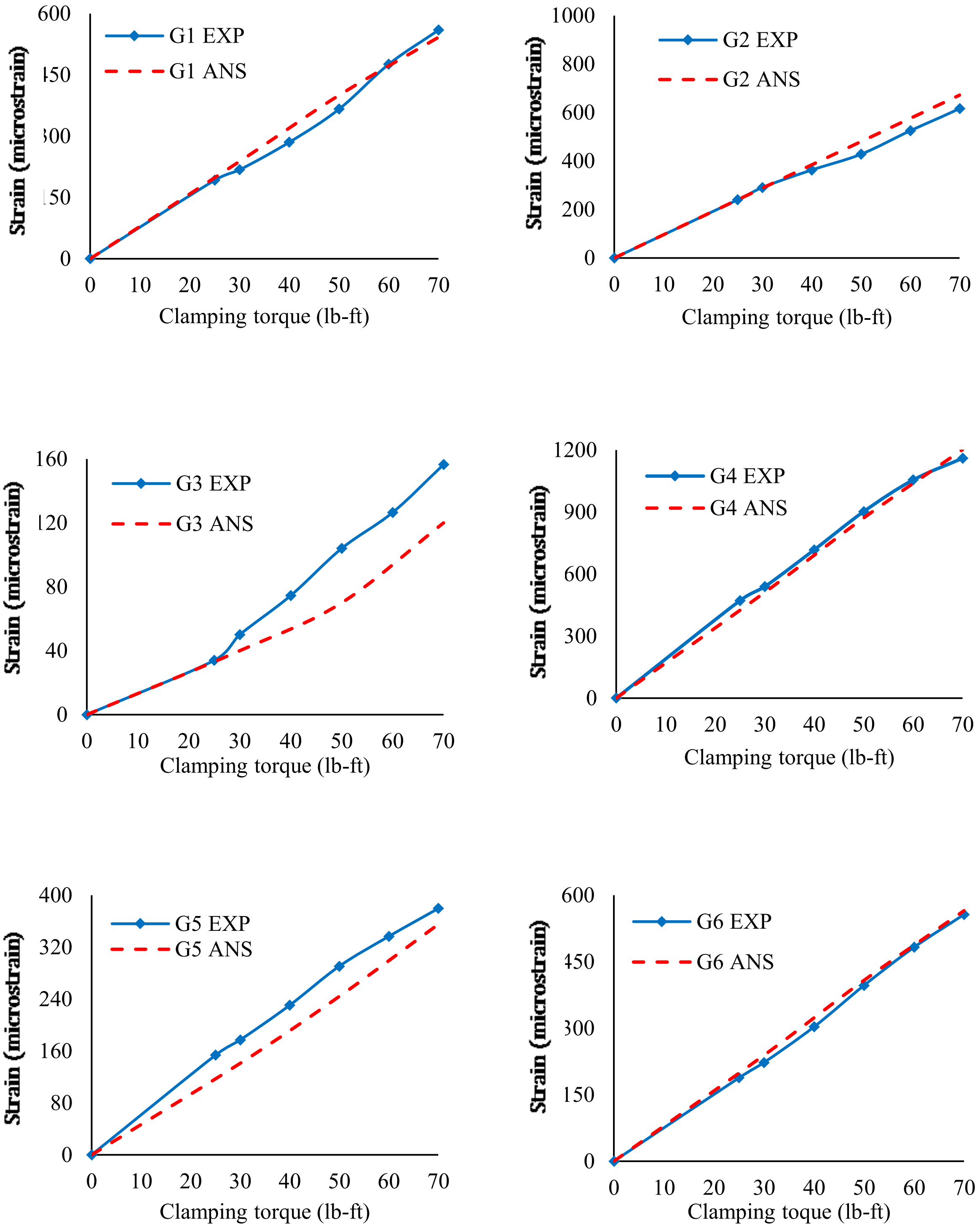

Figure 2-20: Comparison between strains obtained from FEA and strain gages – bolt analysis

2.9.2 Bolt analysis - DIC vs FEA

Strains fields obtained from finite element simulation and DIC methods were compared. The results showed that the model can analyse the thick composite plates subjected to the clamping forces induced by the bolt and calculate the strains with good accuracy. Results obtained from DIC showed that structure encountered a very small rigid body motion during the test, which caused discrepancies between DIC and ANSYS fields of deformations. Switching between the first and second test setup of the bolt experiment (refer to Figure 2-11), extensively eliminated the rigid body motion. However, strain is not influenced by rigid body motion. As it is compared in the following part, the strains obtained from FEA and DIC both follow the same strain distribution pattern and indeed strain values.

The strains obtained at clamping torque of 70 lb-ft are considered here to elaborate the achieved agreement between experiment and numerical investigations. Figure 2-21 illustrates the areas under consideration to compare FEA and DIC results at the top surface. In this figure, the red dotted line indicates the position of the outer edge of the washer. Figure 2-22 illustrates the distribution pattern of the axial strain (along the fibers, X direction) at the upper surface between holes number 1 and 2 obtained from finite element and DIC analysis. Distribution of the transverse strain (perpendicular to the fibers, Y direction) between holes 1 and 3 is illustrated in Figure 13. Comparison between strain distribution patterns obtained from ANSYS and DIC reveals a good qualitative agreement on the top surface between experimental and numerical approaches.

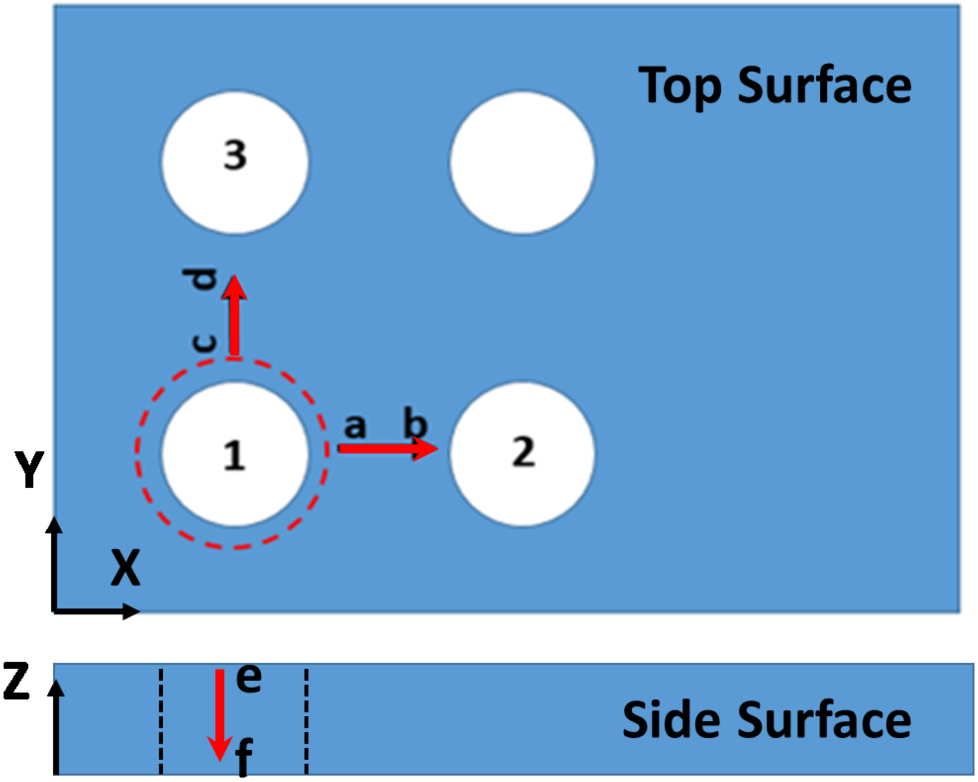

Figure 2-21: The area of interest for FEA and DIC comparison

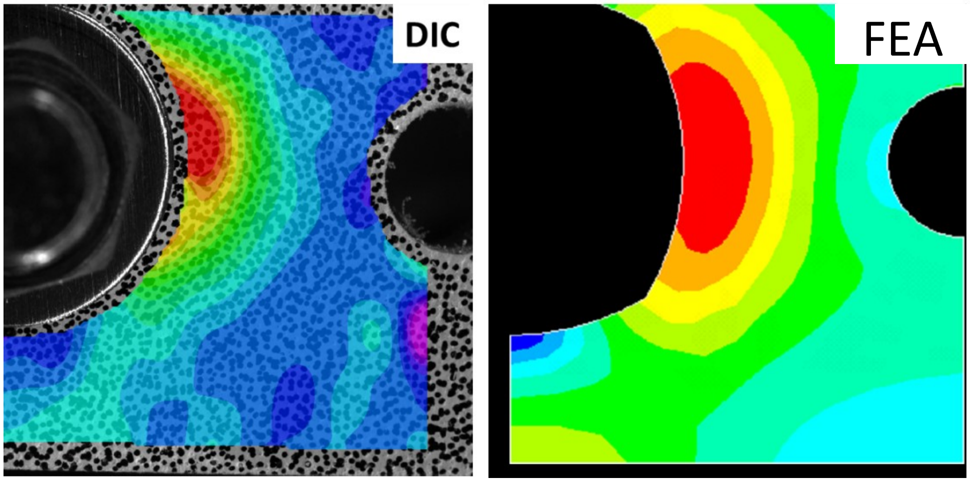

Figure 2-22: Axial strain (along the fibers) on the area between hole 1 and 2 (refer to Figure 2-21)

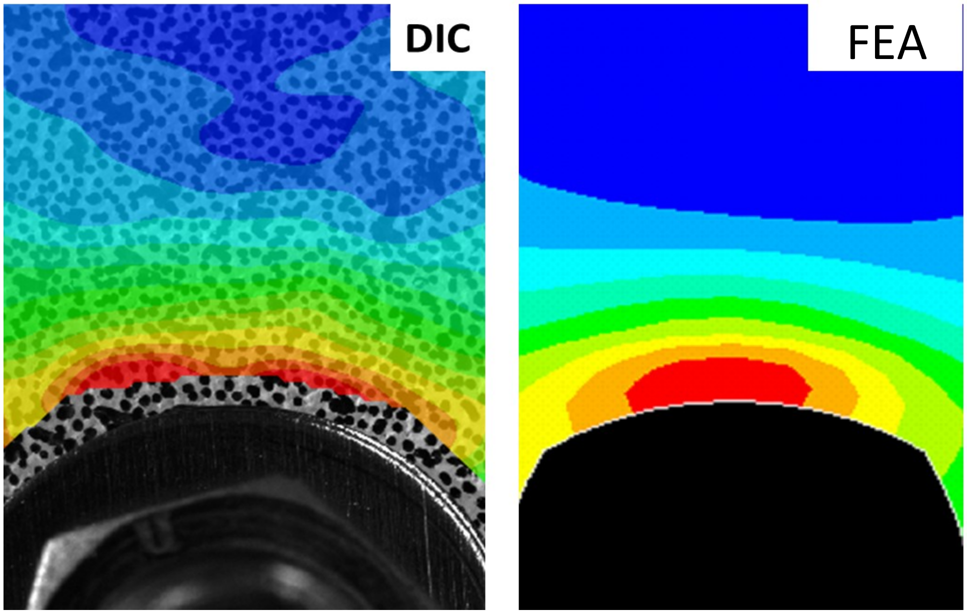

Figure 2-23: Transverse strain (perpendicular to the fibers) on the area between hole 1 and 3 (refer to Figure 2-21)

To compare ANSYS and DIC qualitatively two paths were defined on the top surface of the plate around the washer. Path “ab” which is between hole number 1 and hole number 2 and path “cd” which passes from hole number 1 to hole number 3. Both the selected paths pass through the center of the hole number 1 (refer to Figure 2-21). The axial strain was extracted from both FEA and DIC along line “ab” and normalized by the maximum number obtained which was 1200 microstrain. The normalized axial strain along “ab” is demonstrated in Figure 2-24. Similarly, normalized strains transverse to the fibers are plotted along line “cd” in Figure 2-25. The transverse strain was normalized by 2120 microstrain which was the maximum number obtained from results. It is obvious from Figure 2-24 and Figure 2-25, not only finite element model correlates qualitatively with DIC results but also the strain quantities obtained from these two approaches are in good agreement at the top surface of the plate.

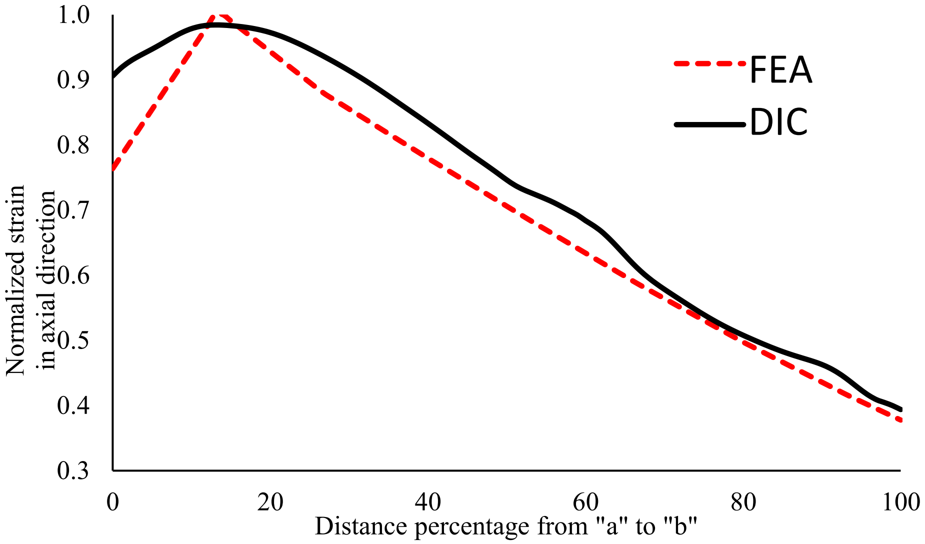

Figure 2-24: The normalized axial strain along “ab”

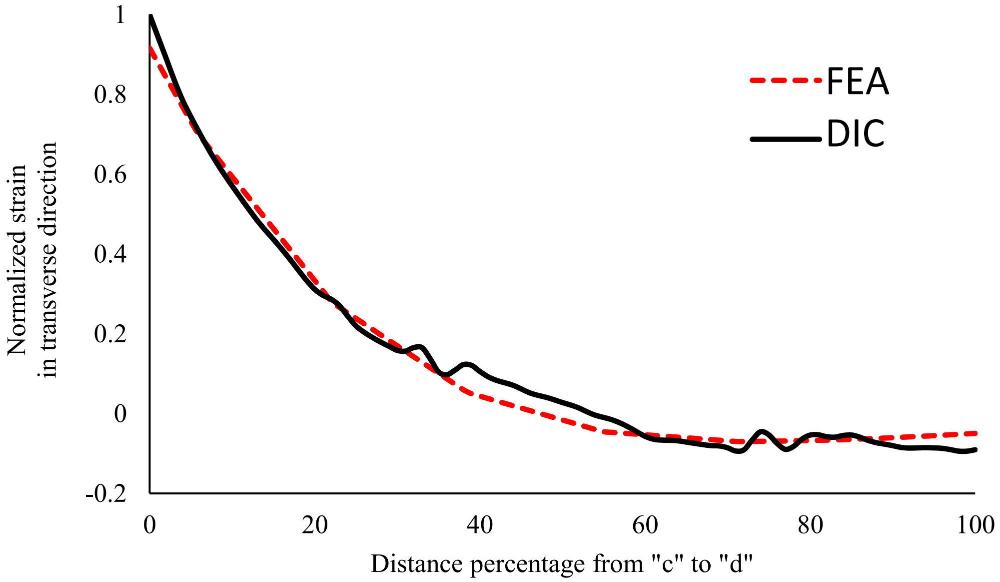

Figure 2-25: The normalized transverse strain along “cd”

Finally, the last comparison was performed on the strain along the thickness of the plate on the side surface. Figure compares the strain pattern obtained from DIC and FE on the side surface inside the area on interest (refer to Figure 2-21). As it is obvious from the figure, ANSYS and DIC results agreed on the transverse strain distribution pattern on the side surface. For quantitative comparison, transverse strain e_{zz} calculated by simulation and measured using DIC are plotted along line “ef” (refer to Figure 2-21) in Figure 2-27. As this figure illustrates, although both methods agree on the strain distribution behavior, the agreement obtained about the amount of strain on the top surface is not observable for the thickness side. Figure 2-27 shows the normalized e_{zz} (values are normalized by 910 microstrain which is the maximum obtained from analysis) along the length of line “ef”. The difference between maximum values obtained from FE and DIC is 25% for strain along thickness on the side surface.

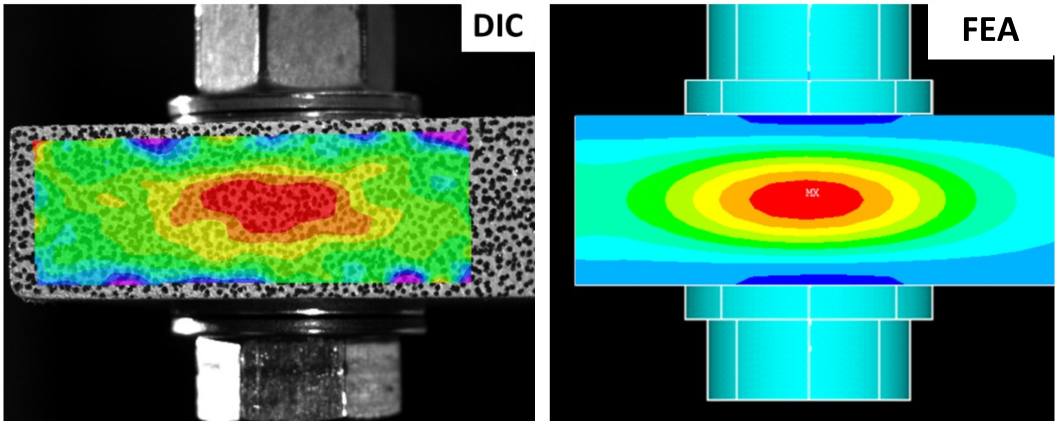

Figure 2-26: Transverse strain (along thickness, e_{ZZ}) on the side surface

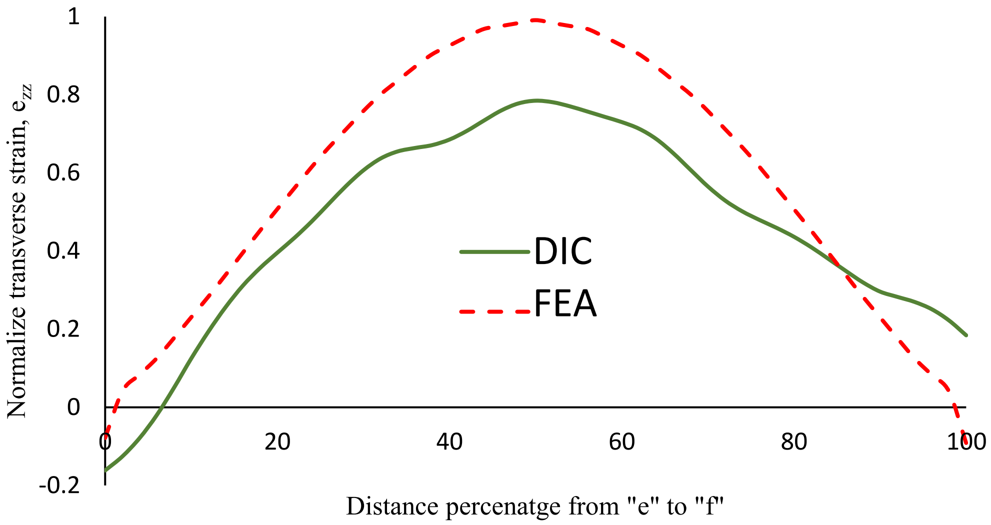

Figure 2-27: Normalized transverse strain (along thickness, e_{ZZ}) along line “ef” (refer to Figure 2-21)

2.10 Bolt analysis - Thickness effect investigation

In this part of the study the effect of the thickness on interlaminar stresses distribution in unidirectional glass/epoxy laminates in presence of bolt joints is investigated. Since the effect of thickness was the main subject of study here, the interlaminar stress distributions should be compared between plates with different number of layers. All the simulated plates had unidirectional layup sequence. The number of elements along the thickness of each plate was defined equal to the number of the layers of the plate to avoid the stresses along the thickness to be affected by the mesh sizing in this direction.

In bolt effect simulation the joint is the major source of the load and the washers are responsible to transfer the load from bolt to the laminate at the top and bottom surfaces. It was intended to produce models which can be practically used, therefore, plates with different thicknesses were associated with different joints with suitable characteristics.

Table 2-3 summarizes the configuration of created models. The hole diameter, “D” is selected based on the available bolts in the market which can tolerate a pretension force of 8700 lb since all the analysis performed considering the same pretension of 8700 lb. It is clear that the same pretension force will result in different clamping torques based on the bolt size. The distance of the hole center to the edge of the plate, “e” is considered to be twice of the hole diameter. The washer sizes (inner diameter “Din” and outer diameter “Dout”) were selected based on the market availability. In addition, it was desired to keep almost the same Din/D and Dout/D ratios in different configurations. As Table 2-3 represents the ratio of Dout/D varied between 2.04 to 2.25 and the ratio of Din/D changed between 1.04 to 1.10. Refer to Figure 2-28 for geometry definitions.

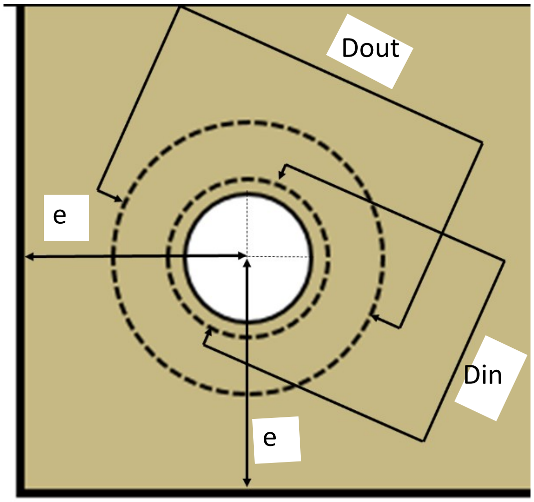

Figure 2-28: Geometry definition for thickness study

Table 2-3: Different configurations used for modeling

NOL	t (inch)	e (inch)	D (inch)	Dout/D	Din/D	WTH (inch)	T (lb-ft)
80	0.72	1	0.5	2.12	1.06	0.0975	70
70	0.63	1	0.5	2.12	1.06	0.0975	70
60	0.54	0.875	0.4375	2.11	1.07	0.0655	62
50	0.45	0.875	0.4375	2.11	1.07	0.0655	62
40	0.36	0.75	0.375	2.17	1.08	0.0655	53
30	0.27	0.625	0.3125	2.20	1.10	0.0655	44
20	0.18	0.5	0.25	2.25	1.04	0.04	35
10	0.09	0.5	0.25	2.25	1.04	0.04	35
2	0.018	0.276	0.138	2.04	1.09	0.025	20

NOL: number of layers, t: thickness of composite plate, e: distance between hole center and plate edge (refer to Figure 2-28), D: hole diameter, Dout: washer outer diameter, Din: Washer inner diameter, WTH: washer thickness, T: Required clamping torque.

The coordinate system of Figure 2-29 was defined for interpretation of the results. To indicate the Z coordinate, the percentage of thickness has been utilized. Points S1 to S3 on X axis and T1 to T3 on Y axis were selected to compare the interlaminar stresses distribution along the thickness between plates with different thicknesses. As it was expected, results showed that for these points, the interlaminar normal stress, Sz, is more significant comparing to the other normal stresses. In addition, for the points located on X axis the dominant shear stress was Sxz, while for the points on the Y axis the significant shear stress was Syz. Since normal stress, Sz, was similar for the points on X and Y axis, it is represented only for the points located on X axis. The positions of the points are illustrated in Figure 2-29. Points S1 and T1 were positioned at the inner edge of the washer, points S2 and T2 were on the midline between inner and outer edge of the washer and points S3 and T3 were on the outer edge of the washer. Figure 2-30 illustrates the normal stress (Sz) and shear stress (Sxz) along X axis and shear stress (Syz) along Y axis on the top surface for plates with 2, 40, and 80 layers. The horizontal axis of Figure 2-30 is the radial distance to the hole center (R, refer to Figure 2-29) divided by the hole diameter. As it can be seen in the graphs of Figure 2-30, all the stresses due to washer on the top surface vanished at the radial distance of 1.25 times of hole diameter from the hole center. Therefore, two additional points (S4 and T4) were selected at the radial distance of 1.25 times of the hole diameter in axial (X) and transverse (Y) axis, to investigate the stresses outside the clamped area. These two points are also indicated in Figure 2-29.

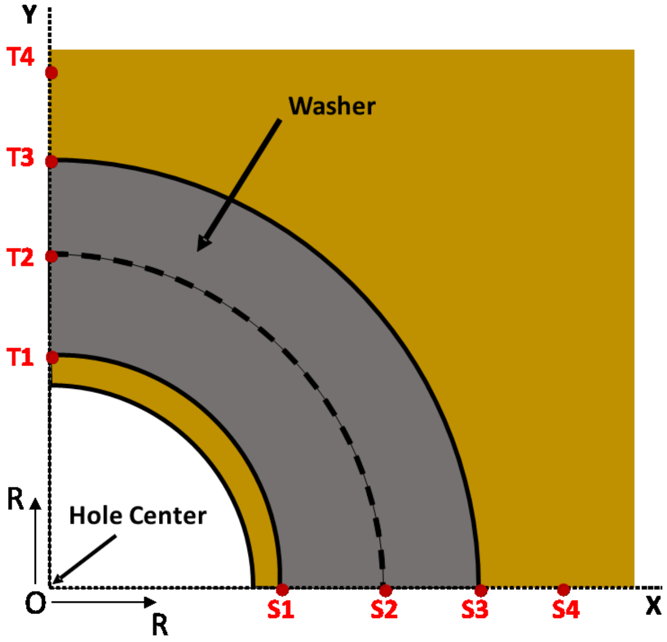

Figure 2-29: Position of the selected points

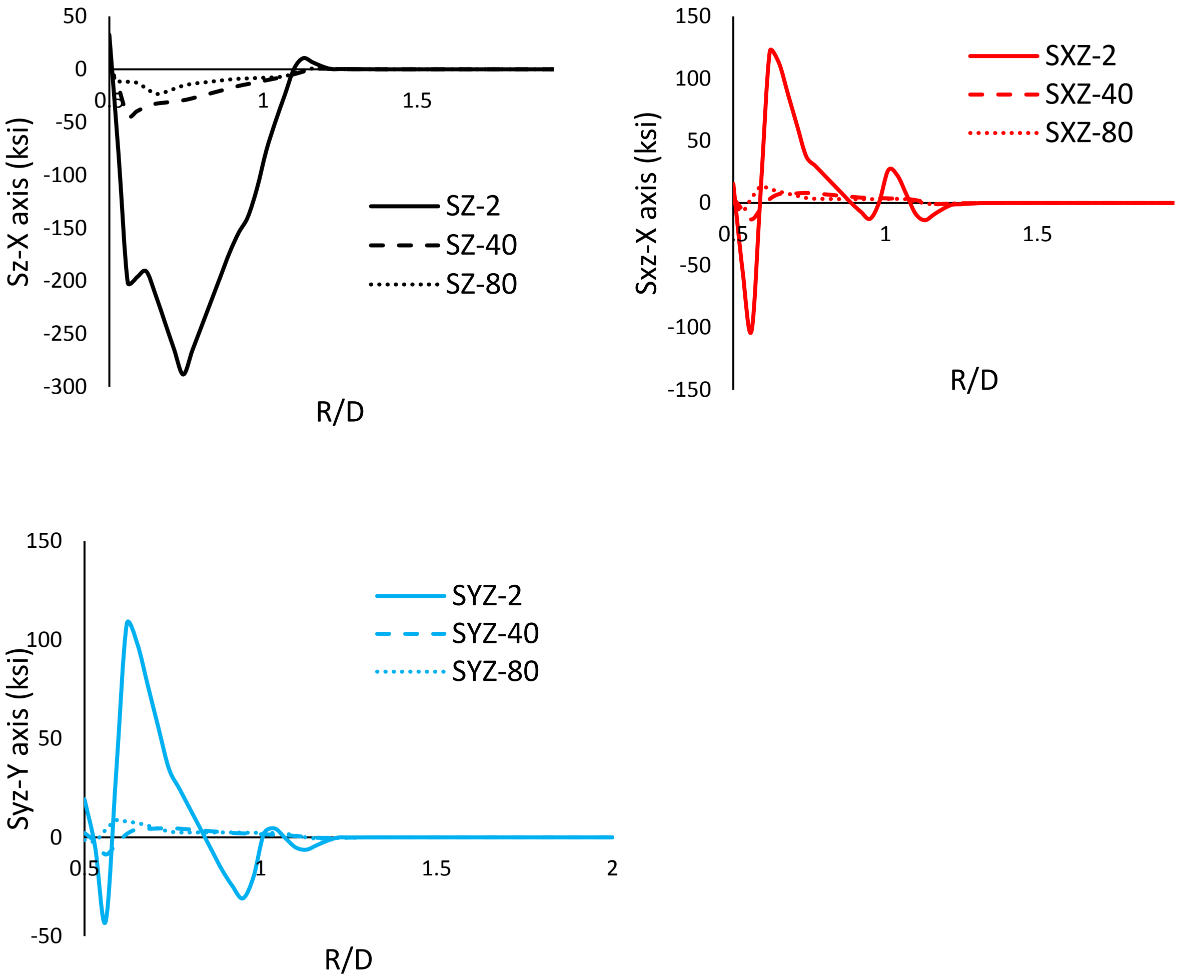

Figure 2-30: Distribution of normal and shear stresses on the top surface

2.11 Bolt Analysis – Interlaminar stresses

Figure 2-31 shows the distribution of the interlaminar stresses Sz, Sxz and Syz along the thickness of the laminates (from top surface to the half thickness) at inner edge of the washer (points S1 and T1, refer to Figure 2-29). Since a symmetric loading condition exists according to the mid-thickness plane, and the plate is unidirectional, the results are presented only over half of the thickness. Following observations were noticed at the inner edge of the washer (points S1 and T1, refer to Figure 2-29):

- The difference in stresses distributions between plates consisting of 2 and 10 layers is more significant than the plates with 10 or more number of layers.
- All three interlaminar stresses are significantly higher for the thinnest plate.
- As it was expected from the symmetry of the loading, the interlaminar stresses (Sxz and Syz) merged to zero at mid-thickness for all plates with different thicknesses.
- In general, as the plate thickness increases the interlaminar stresses intend to show a uniform distribution over a greater percentage of the thickness.
- The plate with 2 layers showed linear distribution of the interlaminar stresses along the thickness.
- All plates experience compression on the top surface at the inner edge of the washer (0% of the thickness) except plates with 10 and 20 layers. It seems that for these two plates a change of stress behavior happened at the first top layer (5% of thickness for 20 layers plate and 10% of thickness for 10 layers plate) for all interlaminar stresses.
- In mid-thickness (50% of the thickness) the interlaminar normal stress (Sz) reduces by increasing the number of layers.

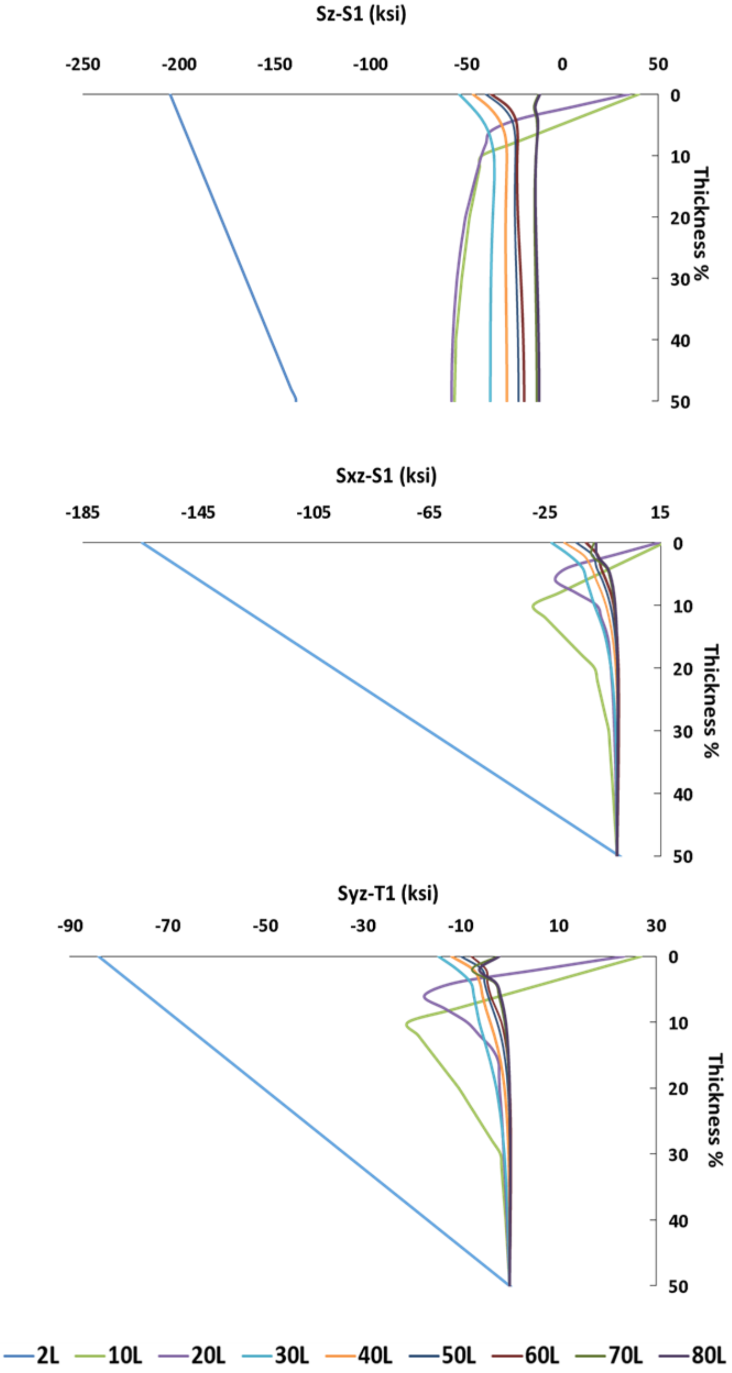

Figure 2-31: Interlaminar stresses distributions along the thickness at the inner edge of the washer

Figure 2-32 illustrates the interlaminar stresses distributions along the thickness for the point located between the inner and outer edges of the washer (points S2 and T2, refer to

Figure 2-29). As it is obvious from this figure, the thinnest plate showed a significantly different distribution comparing to all the other laminates. For plates with 10 and 20 layers the change in the stresses behavior which was observed at the inner edge of the washer did not occur for this point. Like the first point located at the inner edge of the washer, the interlaminar normal stress (Sz) reduces by increasing the number of layers.

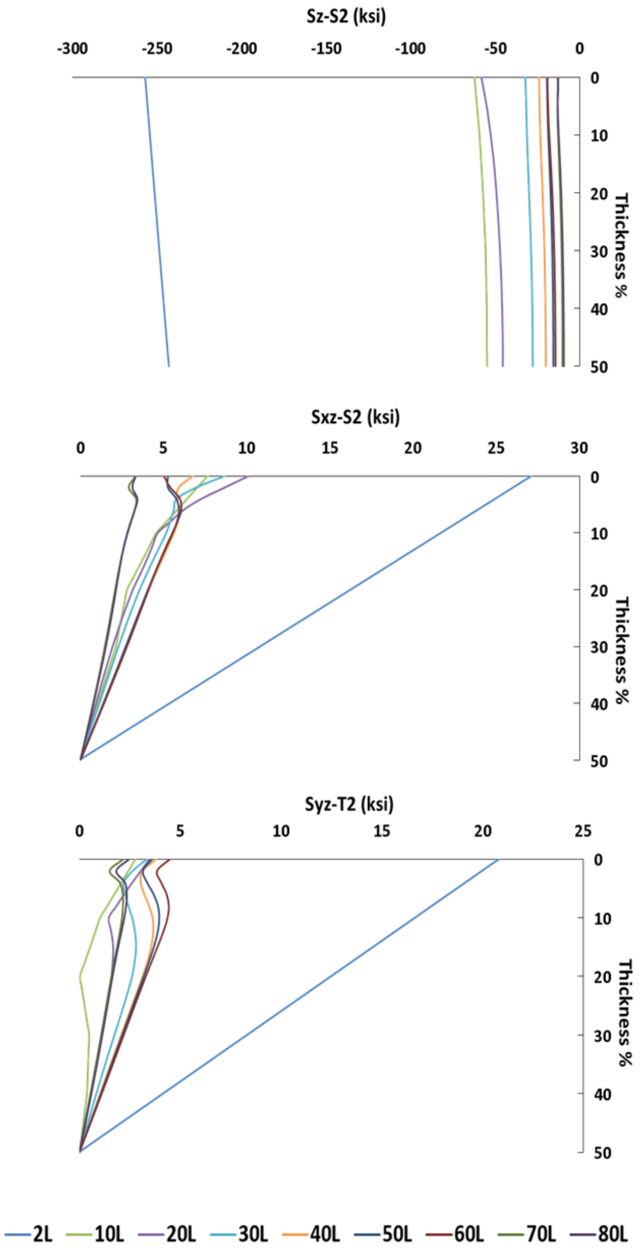

Figure 2-32: Interlaminar stresses distributions along the thickness at the location between inner and outer edges of the washer

In Figure 2-33, the distributions of the stresses at the outer edge of the washer (points S3 and T3, refer to Figure 2-29) are shown. Similar to what was observed at the previous two points, the behavior of the plate with 2 layers is significantly different from other plates especially for the normal stress (Sz). Results showed that the trends of the stress variation changed first between 10 and 20 layers and second, between 50 and 60 layers. For example, the compressive normal stress (Sz) reduced from 2 to 10 layers, then increased between 10 and 20 layers. From 20 up to 60 layers, there is a constant reduction in compression stress (Sz), while at 60 layers it increased and finally for 70 and 80 layers the distribution changed totally.

The stress distributions at the radial distance equal to 1.25 times of the hole diameter are shown in Figure 2-34. As it can be observed from this figure, the stresses distributions out of the contacted region is completely different from what was observed for the points located inside the clamped area. For interlaminar normal stress (Sz), there was a transition from tension to compression stresses between plates consisting of 10 and 20 layers. As it is obvious from Figure 2-34, the maximum normal stress occurred at the mid-thickness for all plates. The interlaminar stresses do not follow a predictable trend of variation with respect to the number of layers. For example, the interlaminar stress, Sxz, increases between 10 and 20 layers and then decreases up to 60 layers and then increases again from 60 to 80 layers. It can be identified that at this point, Sz and Sxz at the top surface vanished for plates with 40 to 80 layers while only plate with 2 layers had zero Syz at this radial distance.

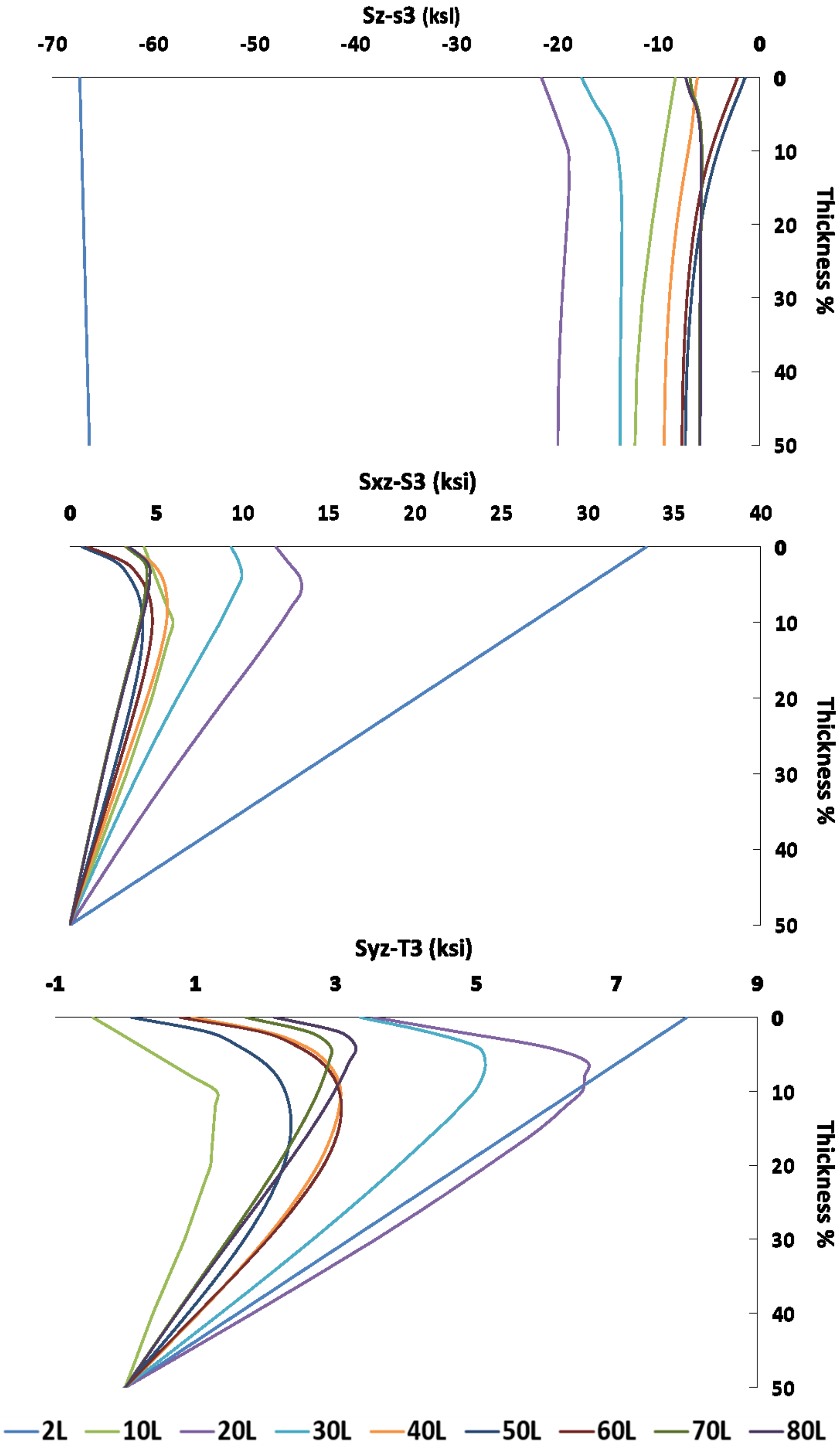

Figure 2-33: Interlaminar stresses distributions along the thickness at outer edge of the washer

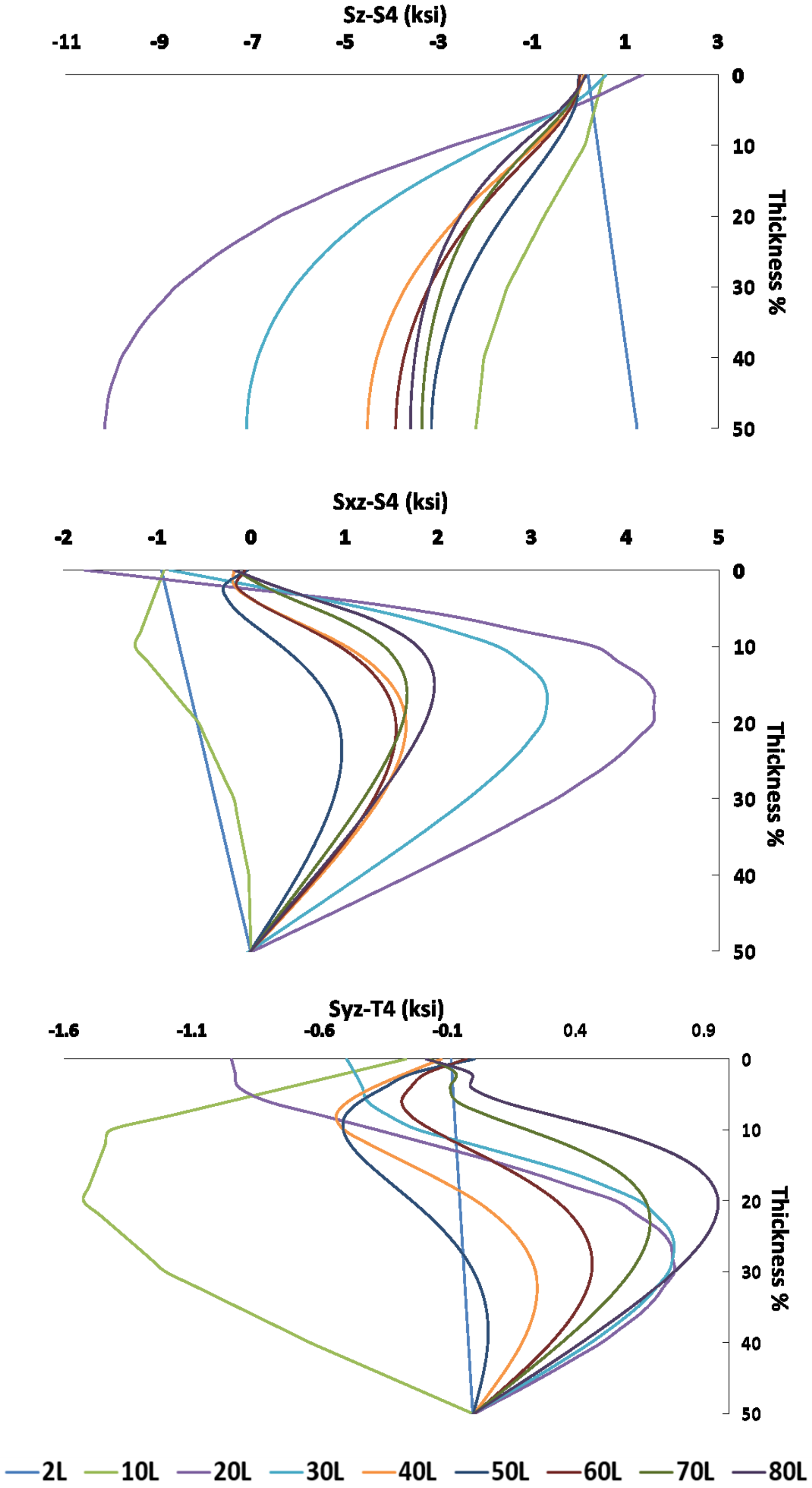

Figure 2-34: Interlaminar stresses distributions along the thickness at radial distance of 1.25 × hole diameter

Although some trends observed for the distribution of the interlaminar stresses along the thickness, considering the stress behavior at each point did not provide any general conclusion on the effect of number of layers on interlaminar stresses. Some local trends are as following:

- For all selected points the plate with 2 layers showed totally different interlaminar stress distribution.
- At the inner edge of the washer plates with 10 and 20 layers showed a different stress behavior while this phenomenon was not noticeable in other points.
- For both points located at inner edge of the washer and between inner and outer edges, the compressive stress at mid-thickness reduced by increasing the thickness of the plate.
- At the outer edge of washer, a change in stresses variation trend was obtained between plates with 10 and 20 layers and 50 and 60 layers.
- At the point located outside of the clamping area the stress distributions were totally different. Sz and Sxz vanished at the distance of 1.25×Diameter of the hole for plates with 40 or more layers while Syz was zero only for thinnest plate at this radial distance.

Although the thinnest plate showed totally different stress behavior comparing to other plates, it is necessary to elaborate that the difference is due to number of layers or the joint configuration. To elaborate the effect of the thickness and joint configuration, an additional analysis was done for plates with 2 to 10 layers. Figure 2-35, shows the distribution of normal stress (Sz) along the thickness at point S1 (refer to Figure 2-29) for plates with 2 to 10 layers.

In this analysis plates were categorized to two groups, group 1 consists of two laminates with 8 and 10 layers and a bolt with 0.25 inch of diameter while group 2 includes 4 plates with 2 to 8 number of layers and a smaller bolt with the diameter of 0.138 inch. It is noticeable that the plate with 8 layers was analyzed for both joint configurations. Table 2-4 summarizes the analysis.

Table 2-4: Characteristics of the plates – Second thickness effect analysis of bolt joint

Group	NOL	t (inch)	e (inch)	D (inch)	Dout/D	Din/D	WTH (inch)	T (lb-ft)
1	10	0.09	0.5	0.25	2.25	1.04	0.04	35
	8	0.072						
2	8-2	0.072	0.276	0.138	2.04	1.09	0.025	20
	5	0.045						
	3	0.027						
	2	0.018						

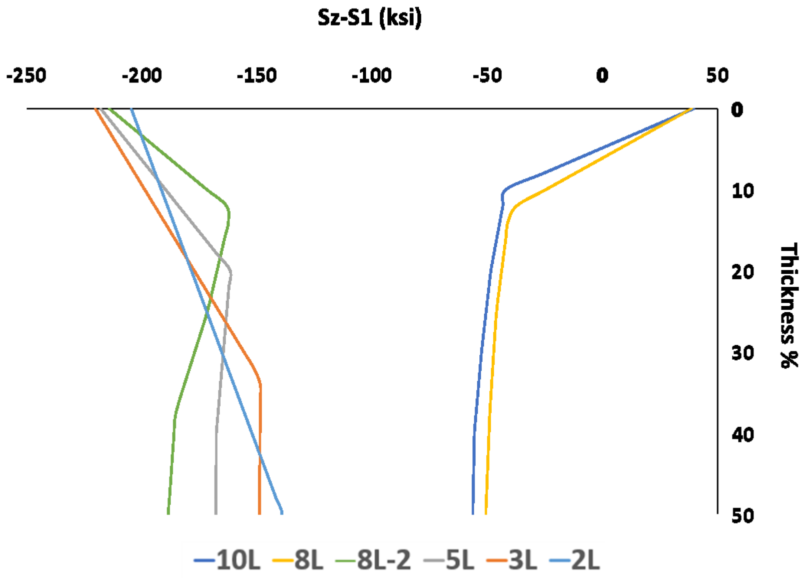

Figure 2-35: Normal stress distribution along the thickness – Second thickness effect analysis of bolt joint

As it is clear from Figure 2-35, the plates with the same joint characteristics showed similar stress distribution trend along the thickness. The same comparison was performed for interlaminar normal and shear stresses at the other points and similar behavior was observed. Considering Figure 2-32 to Figure 2-34, it can be concluded that the similarity between plates with the same bolt and washer configuration is observable also for the plates with more than 10 layers. Although in the first analysis the joint configurations were selected in a way to keep the ratios of washer outer diameter to hole diameter and washer inner diameter to hole diameter in a limited range, it was observed that even a small change in washer and bolt size can affect the stresses and change their distribution completely. It can be concluded that the effect of washer and bolt configuration on the interlaminar stresses is more significant than the effect of the thickness of the plate.

3 Flexural Bending

3.1 Flexural bending - Model simplification

Figure 3-1 shows the schematic of the yoke of the helicopter. In the real case, the yoke is a thick tapered composite beam which is connected to the other parts of the assembly using bolt joints. Considering all aspects of the yoke of the helicopter, will make the study very complicated both analytically and experimentally. Therefore, the geometry and loading conditions of the real yoke were simplified such that the major aspects will be saved but also the complexity of the investigations will be reduced both analytically and experimentally. The simplified model can be tested experimentally utilizing less complicated equipment and procedures. In addition, the finite element model includes all major aspects of the actual part and can be validated by the tests results. Therefore, it was desired to introduce an experimentally validated finite element model which can predict the structural behavior of the thick composite plate in presence of bolt joints while it is subjected to flexural bending.

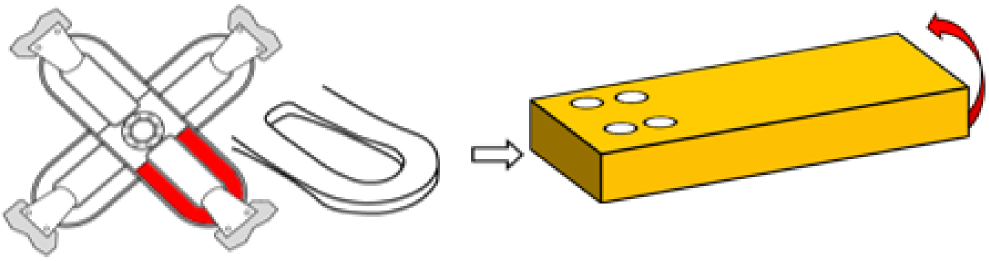

Figure 3-1: The yoke of the helicopter simplification

In the previous chapter, the model of the bolt joint in thick composite plates was presented and the accuracy of the joint simulation method was verified through experimental technics. In the present chapter, the previous model will be improved to include the external loading of flexural bending. As it was described before the simplified model is a thick composite plate with bolt joints. Considering the thick composite plate as a simplification of the helicopter main rotor yoke geometry, the testing equipment was designed to fix one end of the plate and apply a bending moment to the other end via bolted joint connections. In addition, different fixtures were designed for the loading end of the plate to provide different loading conditions. The details of testing machine and fixtures configuration will be explained in the next section.

3.2 Flexural bending - Test setup

A CAD model of the testing machine which was used to perform the flexural bending tests is shown in Figure 3-2. The set up was designed by Heer [105] and installed in the Concordia Centre for Composites material characterization lab. A displacement-controlled MTS 244 Series hydraulic actuator was utilized to apply force at the loading end. This actuator is equipped with MTS Series 249G2 swivel ball-joints at both ends. The ball joints provide necessary freedom for the actuator ends to pivot and ensure that the loading of the actuator remains axial during operation. As it is illustrated in both Figure 3-2 and Figure 3-3, the other end of the plate is fixed to the heavy steel cross-beam of the testing machine by four 1/2-13UNC-2A bolts.

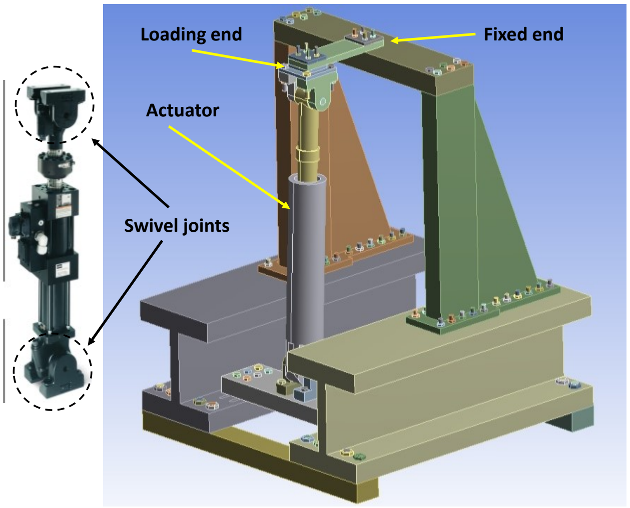

Figure 3-2: Schematic of flexural bending machine

Two different adapters were designed for the loading end to connect the sample to the upper swivel ball-joint of the actuator. Figure 3-3 shows the setup assembly and the clamped-clamped and cantilever adapters. The clamped-clamped adapter includes a 1-inch thick steel block and four 1/2-13UNC-2A bolts which attach the loading end of the sample to the actuator swivel joint. A 1-inch thick steel block was also installed on the top surface at the fixed end of the plate in both clamped-clamped and cantilever configurations. The dimensions of the steel blocks are illustrated in Figure 3-3. For the cantilever setup the loading end adapter was modified. In the cantilever setup the adapter holds the end of the sample between two cylindrical faces which are fastened together by two 5/16-18UNC-2A bolts. The cantilever adapter was utilized to mitigate the axial force inside the plate due to the clamping of the loading end.

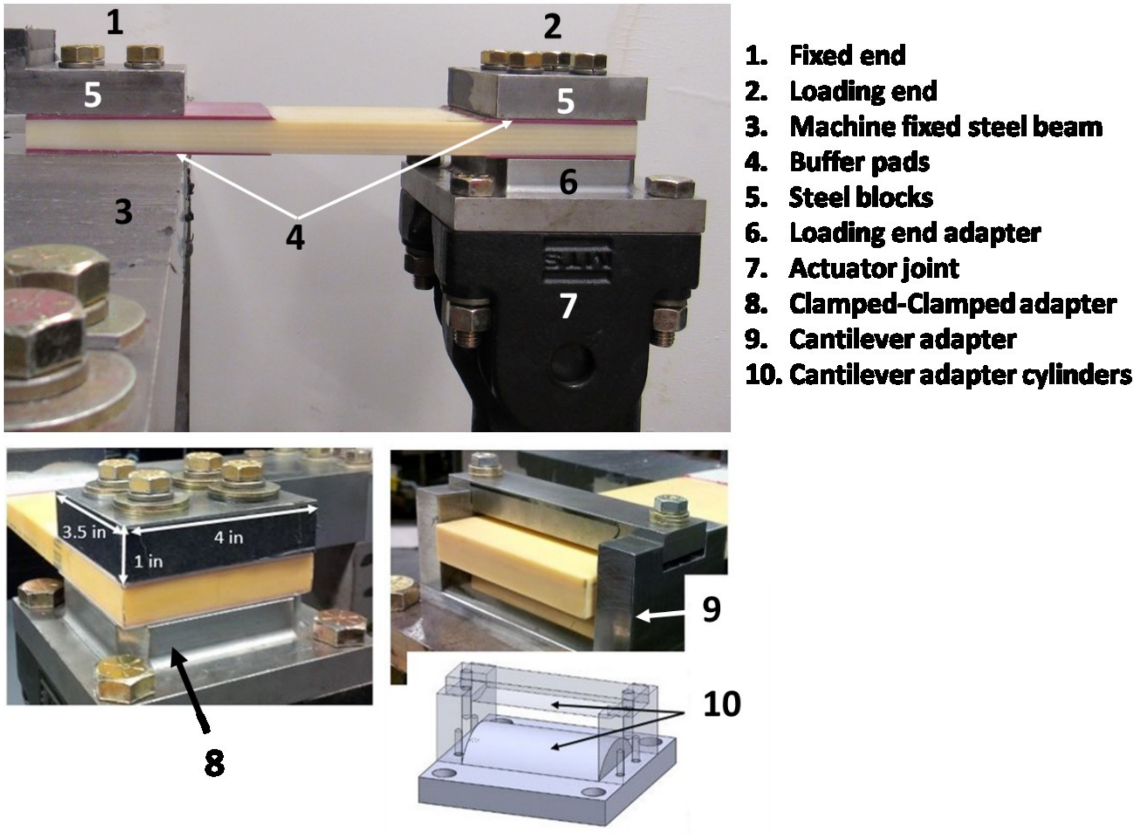

Figure 3-3: Clamped-clamped vs Cantilever setups

For the clamped-clamped model, buffer pads were bonded to the top and bottom surfaces of the laminate at both fixed and loading ends. The buffer pads were made of G-7 Garolite and were adhered to the main plate using 163-2 adhesive film from 3M. The buffer pads width was equal to the width of the plate while the fixed end of the sample had longer buffer pads than the loaded end as it is indicated in Figure 3-3. Buffer pads were installed to avoid the direct contact of the steel plate with the composite laminate. It is noticeable that the cantilever model does not have the buffer pads and bolt holes at the loading end.

3.3 Flexural bending - Sample manufacturing

The samples were manufactured using CYCOM E773 glass/epoxy prepreg from CYTEC, the majority of which were made according to the procedure proposed by the industrial partner of the project. Figure 3-4 shows the sample geometry which was obtained from Bell Helicopter describing the clamped-clamped specimen. For the clamped-clamped configuration, only unidirectional samples were tested while for cantilever, unidirectional and cross-ply samples were analyzed. Most of the experiments were done on the samples with 80 layers of the mentioned glass/epoxy. In addition, some other plates with different number of layers were manufactured and tested to validate the finite element model for different number of layers and to investigate the effect of thickness. The results of the analysis will be discussed later.

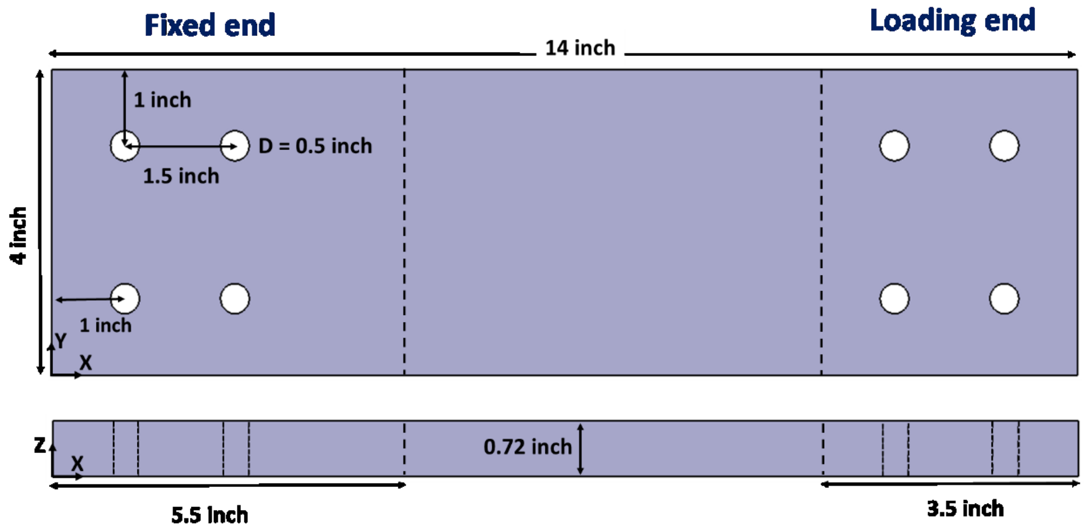

Figure 3-4: Specimen geometry

3.4 Flexural bending - Finite element model

The major concern about the finite element analysis was adequate flexibility of the model to perform further parametric studies. Therefore, the finite element simulation was coded fully parametric using APDL language programming instead of direct model development in ANSYS. The written code provides the ability to define and establish further parametric studies, which is an asset during the design process. Components and the related characteristics were simulated to correspond exactly to the experimental testing setup as much as possible. This is critical when the model validation should be obtained by experimental tests. In this section, the details of parametric simulation will be reviewed.

3.4.1 Model Geometry

As it was explained before, two different setups were considered for the experimental tests, the clamped-clamped setup and cantilever setup. Therefore, two different models had to be simulated during finite element analysis. Table 3-1 reviews the components modeled for each of the above configurations.

Table 3-1: Components of Clamped and Cantilever models

Setup Component	Clamped-clamped model	Cantilever model
1. Bolt	Four at each end (eight total)	Four at fixed end only
2. Washer	Four at each end (eight total)	Four at fixed end only
3. Steel plate	One at each end (two total)	One at fixed end only
4. Big buffer pad	Two at fixed end	Two at fixed end
5. Composite plate	One	One
6. Small buffer pad	Two at loading end	None
Note:	The steel cross-beam at the fixed end of the sample and the adapter for bolting the loaded end were modeled as rigid plates for analysis.	

Figure 3-5 shows the different components created in ANSYS and compares the clamped-clamped and cantilever configurations. During the simulation of each part the corresponding component in the experimental setup was considered. Since the critical component in the simulation is the composite plate, modeling all the details related to the other components will increase the complexity and running cost of the simulation. Therefore, the whole fixed end cross-beam of the machine was replaced with a rigid surface during simulation. Also, the adapter at the top of the actuator for clamped-clamped model was modeled as a rigid plate. These simplifications, not only maintain the accuracy of the results obtained for the composite plate but also reduce the running time.

For the sake of simplicity, the adapter at the loading end of cantilever setup was not included in the model. Instead of modeling the whole cantilever adapter, the vertical displacement was applied directly to the plate. The mechanism of loading will be discussed in more detail later. As it can be seen in Figure 3-5, a specific pattern was followed to partition different components. The specific partitioning pattern provides the designer with full control on meshing pattern and sizing. Since a mesh with overlapping nodes for contacted areas will improve the accuracy of contact modeling and leads to faster convergence of the nonlinear contact analysis, the same mesh pattern and sizing were applied on contacted areas. To provide this situation, mapped mesh method should be utilized instead of free mesh. Therefore, critical contacted areas were partitioned to similar four-sided regions to make each section appropriate for mapped meshing.

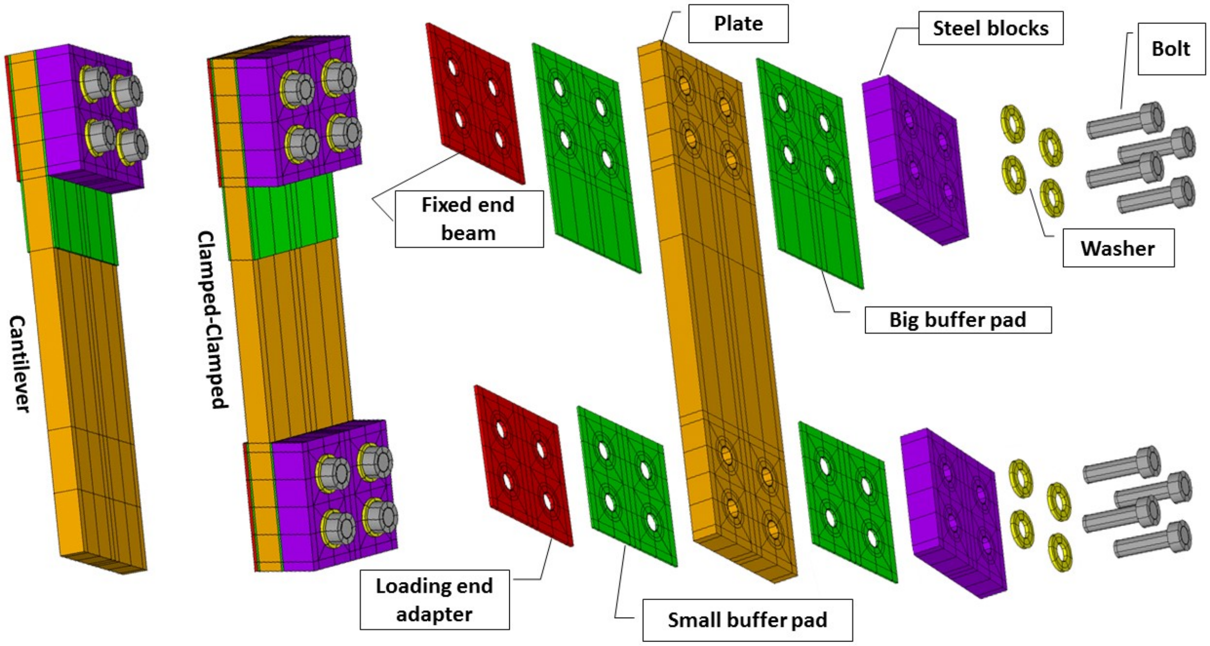

Figure 3-5: Finite element parts

To mesh the created geometry, the layered solid element was utilized. The Solid186 element in ANSYS 16.2 is a three-dimensional brick element consisting of 20 nodes. Each node has three degrees of freedom which are displacements in three orthogonal directions. This element can be used to mesh both isotropic and orthotropic materials [2]. Plates with two different layer sequences were investigated during the experimental test and the finite element simulation. At a first step, the study subject was a laminate with a unidirectional layup sequence of $[0]_{80}$. For the second step, the study case was changed to a laminate with a symmetric cross-ply layup sequence of $[0/90]_{20S}$. To use the solid element for meshing the layered components, a section should be defined and associated with each element. Here, the section represents number of layers and their orientation for each element. As an example, for the laminate with 80 layers, a 4 layers section was defined, and 20 elements were created along the thickness which results in totally 80 layers along the thickness of the laminate.

For the unidirectional plate, the section was the same for each element through the thickness of the laminate while for cross-ply layup, two different sections were associated for the top and bottom halves of the plate. The elements located at the upper half of the plate were associated with a section defined as $[0/90]_2$, while the bottom half was meshed with a $[90/0]_2$ section. For example, for the cross-ply laminate with 80 layers, the layup sequence is $[0/90]_{20S}$. To model the mentioned cross-ply laminate, ten layers of $[0/90]_2$ is created on the half top part and ten layers of $[90/0]_2$ in the half bottom part. In ANSYS, the reference for layer orientations is the element coordinate system X axis. It is noticeable that during the meshing process, it is critical to align the X-direction of all elements parallel to the plate's X-direction (refer to Figure 3-4). Using the meshing pattern, which was discussed earlier, the plate was meshed by 94480 solid elements (refer to Figure 3-7).

3.4.2 Material Properties

Since the exact material properties were not readily available, the first ANSYS analysis used the material properties that were defined in the material library of ANSYS Workbench 16.2. Meanwhile, experimental tests were underway to find more accurate numbers for material properties [102]. The material properties were modified according to these experimental results and simulations were duplicated.

In Table 3-2 the material properties from the various sources is represented. For the plate, the values are compared with the available data from the manufacturer’s data sheet. As mentioned previously, the simulation was performed fully parametric. The incorporated parameters are as follows:

Length and width of the laminate
Number of layers
Layers thicknesses
Layers orientation
Material properties (For all modeled parts)
Hole diameter
Bolt and washer size

The designer can change any of the above parameters to perform a parametric study. The joints characteristics were defined according to Figure 3-6. To simplify the modeling, the bolt head hexagonal shape was converted to a cylinder with the same height and the hexagonal shape of the bolt head cross section was converted to a circle with the same area.

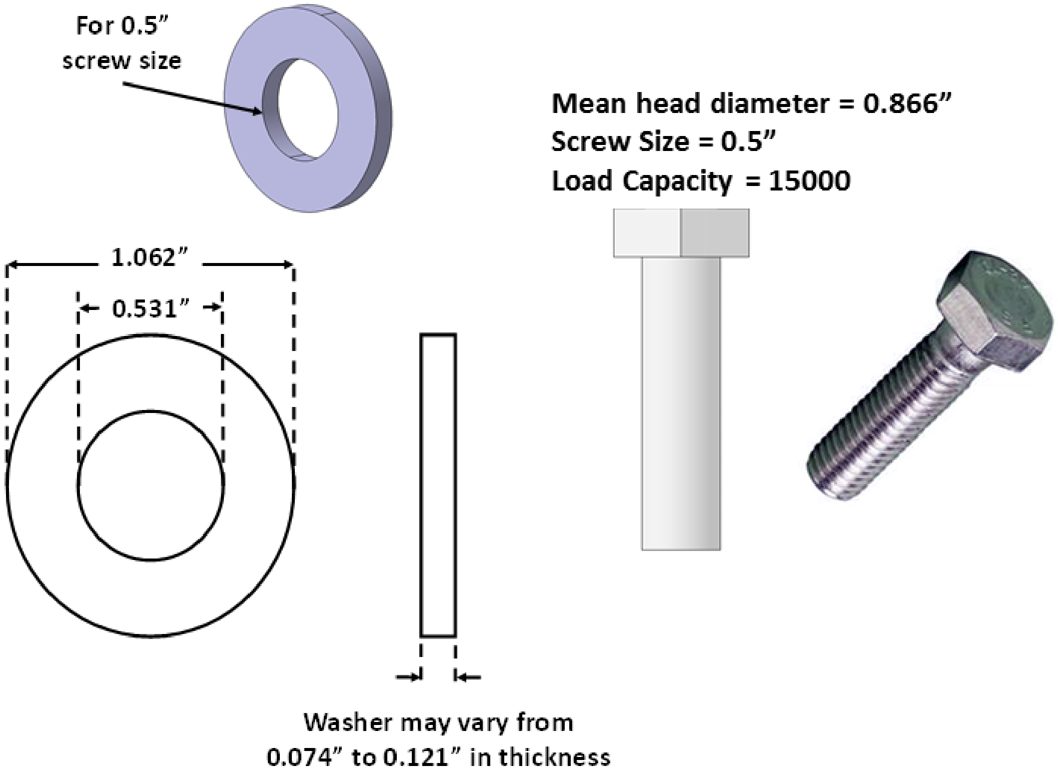

Figure 3-6: Washer and bolt geometry

Table 3-2: Material properties

		Glass/Epoxy					
		E_1	$E_2 = E_3$	v_{23}	$v_{12} = v_{13}$	G_{23}	$G_{12} = G_{13}$
Plate	**ANSYS**[*]	7.25 (Msi) 50 (GPa)	1.16 (Msi) 8 (GPa)	0.4	0.3	0.56 (Msi) 3.8 (GPa)	0.73 (Msi) 5 (GPa)
	Experiment [102]	6.95-7.52 (Msi)	1.73-2.01 (Msi)		0.28	-	0.62 (Msi)
	Technical Data Sheet[**]	7-9 (Msi) 48-62 (GPa)	1-2 (Msi) 7-14 (GPa)	Not available			
Washer, Bolt and Steel plate		**Steel**					
		E		**v**			
		29 (Msi) 200 (GPa)		0.30			
Buffer pads[***]		**Garolite (G-7)**					
		E		**v**			
		1.6 (Msi) 11 (GPa)		0.25			

[*] ANSYS workbench 16.0 material library

[**] www.cytec.com-CYCOM E773 Epoxy Prepreg Data Sheet (Page 4)

[***] http://www.boedeker.com/ilamg_p.htm

Solid186 element with the isotropic features, was incorporated to mesh the washer, bolt, buffer pads, steel plates, and the rigid plates which represent the fixed and loading ends. The washer, bolt and steel plate are all made of steel with the properties mentioned in Table 3-2.

To model the end plates as rigid, a material with a very high stiffness (100 times that of steel) was associated with these parts. The properties of the buffer pads, bolt, and washer materials are all represented in Table 3-2. As it was described in analysis of the bolt joint, the solid element does not have the rotational degree of freedom and it is not possible to apply the clamping torque directly to the bolt head. Therefore, a pretension section was defined for each bolt joint to apply the pretension force in the stud of the bolt. For more information about the relation between the clamping torque and pretension force of the bolt refer to section 2.4.

3.4.3 Contact Considerations

Buffer pads were made of ultra-high temperature G-7 Garolite from McMaster-Carr. Two different buffer pads were utilized. The big buffer pads $(4 \times 5.5\ in^2)$ were attached to the top and bottom surfaces of the plate on the fixed end and the small ones $(4 \times 3.5\ in^2)$ were glued to the loading end of the plate only for clamped-clamped model. The material properties of the buffer pads were presented in Table 3-2. The fixed beam of the testing machine was replaced with a rigid plate in the model to reduce the complexity of the analysis and the number of elements. Figure 3-7 illustrates the mesh pattern for various parts of the model. It is noticeable that similar meshes were created with overlapping nodes for the areas which are in contact with each other to improve the accuracy of the contact analysis. The steel and rigid plates are not shown in Figure 3-7.

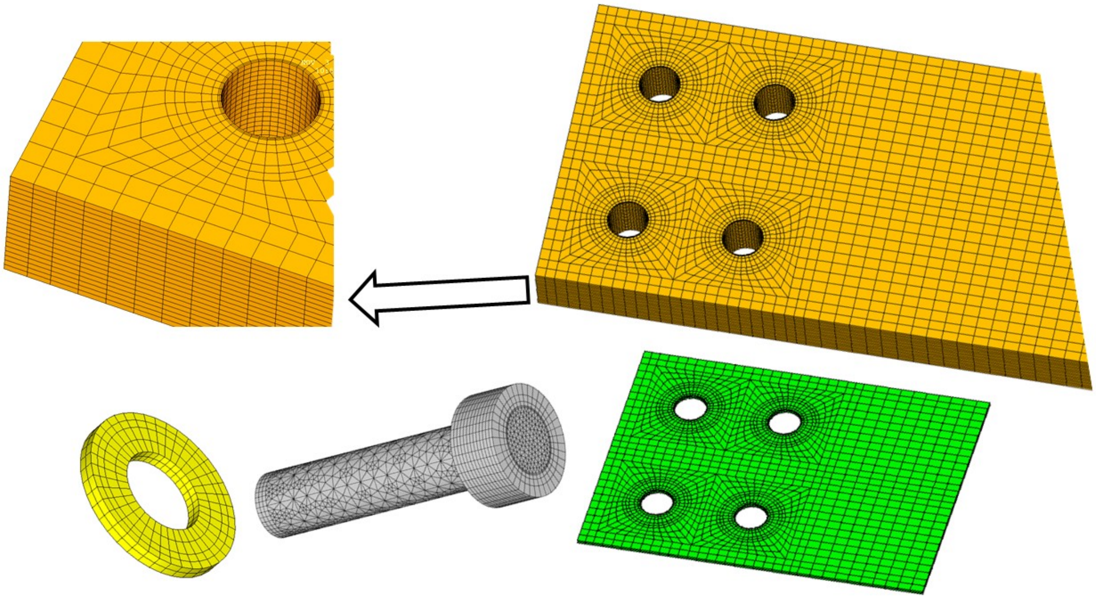

Figure 3-7: Mesh pattern for laminate, buffer pads, washers and bolts (parts not shown to scale)

Surface to surface contact elements were created at the contacted regions. In this case, it is necessary to define a contact surface and a target surface. Stiffer and bigger surfaces are normally considered as the target surface. In ANSYS, the CONTA174 element is designed to simulate contact behavior. Sliding happens between a target surface and a deformable surface defined by contact element. The TARGE170 element is used to simulate various three-dimensional target surfaces for the associated contact elements [2]. In ANSYS different contact behaviors can be simulated between target and contact surfaces. In this simulation, two different contact behaviors were considered according to the characteristics of the existing model. For certain areas, a bonded contact was defined. In a bonded contact, the nodes of the target and contact surfaces are attached to each other, so at the contact area no separation or sliding is possible. The other type of contact behavior defined in this simulation was frictional contact. In frictional contact, separation, collapsing and sliding can occur between contacted surfaces (contact and target). Table 3-3 summarizes the type of defined contact between different mating parts.

Table 3-3: Contact behavior definition

	Bolt	**Washer**	**Steel Plate**	**Buffer Pad**	**Plate**	**Rigid Stand**
Bolt	-	bonded	-	-	frictional	-
Washer	bonded	-	frictional	-	-	-
Steel Plate	-	frictional	-	frictional	-	frictional
Buffer Pad	-	-	frictional	-	bonded	frictional
Plate	frictional	-	-	bonded	-	-
Rigid stand	-	-	-	frictional	-	-

3.4.4 Loading Mechanism

One of the most challenging endeavors of the simulation was modeling the loading mechanism. As previously described, the actuator is equipped with a swivel joint at both ends. As the hydraulic pressure increases, the piston will extend in axial direction. As the actuator pushes the sample, the end of the sample rotates under deflection, the adapter linkage between the specimen and actuator (which remains perpendicular to the sample because of the bolt joints) causes rotation of the whole actuator around the joint located at the bottom (Joint 1 in Figure 3-8). This interaction is illustrated in Figure 3-8 for the clamped-clamped model. Therefore, the simulation of the loading mechanism in the clamped-clamped model should include the axial extension of the piston and rotation of both swivel joints at both ends of the actuator.

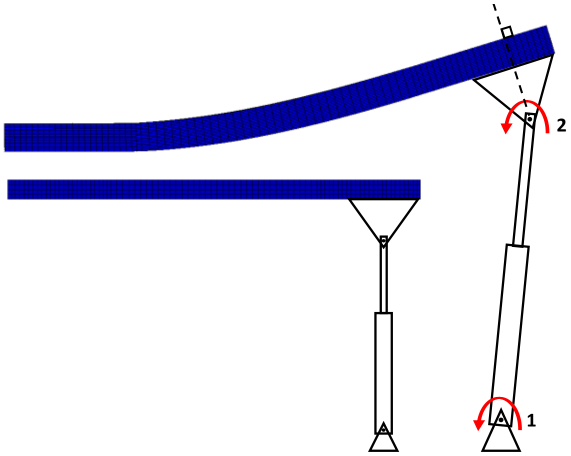

Figure 3-8: The movement mechanism of actuator for the clamped-clamped model (not to scale)

Link180 is a three-dimensional link element that was utilized to simulate the loading mechanism of the clamped-clamped model. Four rigid links modeled the swivel joint at the moving end of the actuator and is represented as point 2 in Figure 3-8. In this figure, the triangular part between point 2 and sample represents the ball-joint and adapter plate. Since this region is clamped to the plate by bolted joints and a steel plate, the dashed line that passes through the triangle center remains perpendicular to the plate (refer to Figure 3-8). These four equal rigid links which modeled the connection between plate and actuator are shown in Figure 3-9. The distance between the pivot point of the swivel ball-joint and the base of the specimen was measured, and the length of the above links was selected to accurately represent the real testing condition.

The next step is to model the actuator axial extension. Another link element was created with the actuator initial length. The actuator link (between point 1 and point 2 in Figure 3-9), contains only a specific thermal expansion coefficient, acting axially, as the material property. In this scenario, applying an appropriate temperature increment on the actuator link, will control the link axial elongation. It should be mentioned that in real test case, the system controls the axial displacement of the piston. In Figure 3-9, point 1 is fixed in all three directions but the actuator link can rotate at both ends. Here is an example of proper temperature increment calculation:

$$Thermal\ expansion\ coefficient\ of\ the\ actuator\ link = \alpha = 0.010226\ \frac{1}{℃}$$

$$Initial\ length\ of\ the\ actuator\ link = L_0 = 38.5$$

$$Imposed\ temperature\ on\ the\ actuator = \Delta T = 1\ ℃$$

$$Actuator\ axial\ elongation = \Delta L = L_0 \alpha \Delta T = (38.5)(0.010226)(1) = 3.937\ inch$$

$$= 10\ mm$$

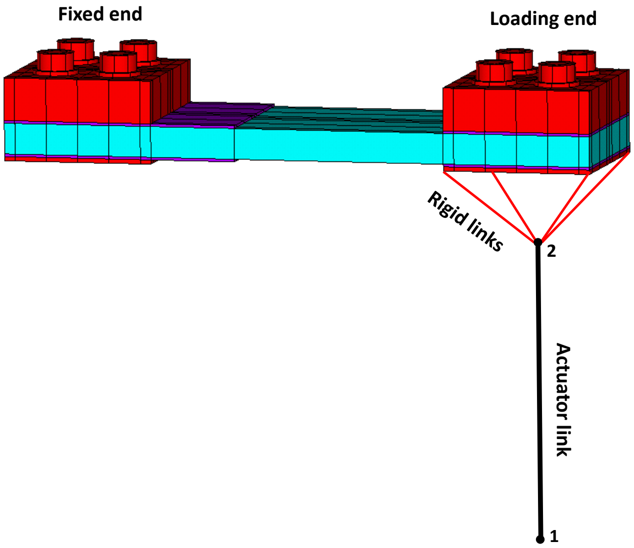

Figure 3-9: Loading mechanism simulation for clamped-clamped model (not to scale)

To verify the accuracy of the simulation of the actuator mechanism for clamped-clamped model the actuator axial load recorded during experiment is compared to the load in the actuator link modeled in finite element simulation. Table 3-4 compares the load in the actuator at two different actuator axial elongations obtained from model and experimentally from the load cell in the actuator. As it is obvious from this table, the simulation and experimental data correlate with a good accuracy which shows the validity of the loading end simulation approach.

Table 3-4: Actuator axial load – simulation vs experiments

Actuator axial elongation (mm)	**Actuator Force (N)**		**Difference %**
	Experiment	**Simulation**	
10	4890	5026	3 %
25	10700	11005	3 %

AS described before, the configuration of the loading end was changed in testing the cantilever sample. Due to the interaction between the cylindrical surfaces of the cantilever adapter (refer to Figure 3-3) and the sample loading end, it would be too computationally intensive to perform an exact simulation. Therefore, to reduce the complexity of the model, the loading mechanism of the cantilever configuration was not included in the finite element simulation and the displacement was directly applied to the sample. Figure 3-10 shows the position of the load line at which the displacement was applied in cantilever model. However, the displacement was applied to the bottom surface of the plate.

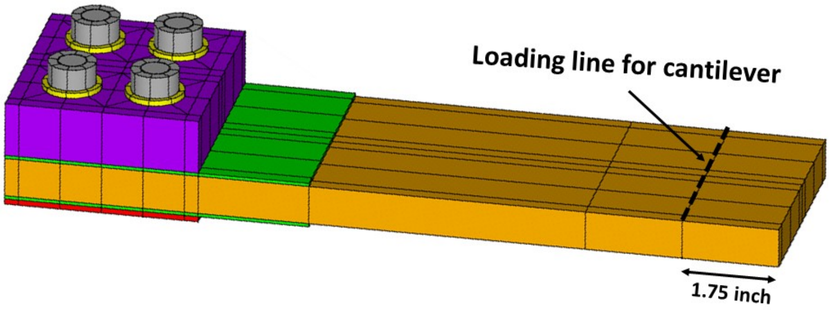

Figure 3-10: Loading line position in cantilever model

3.5 Flexural bending - Experimental verification

To verify the numerical model, experiments were carried out on three groups of specimen configurations and layup sequences: unidirectional clamped-clamped, unidirectional cantilever, and cross-ply cantilever. Like the bolt joint investigation, both strain gages and digital image correlation approaches were implemented to validate the finite element model. In the first approach, several strain gages were attached on the top and the side surfaces of the sample. At the top surface axial strain gages measured axial and transverse strains, while the side surface had stacked T-gauges to find shear strain. Figure 3-11 shows a model of a strain gage array on the (a) top and (b) side surfaces of the sample.

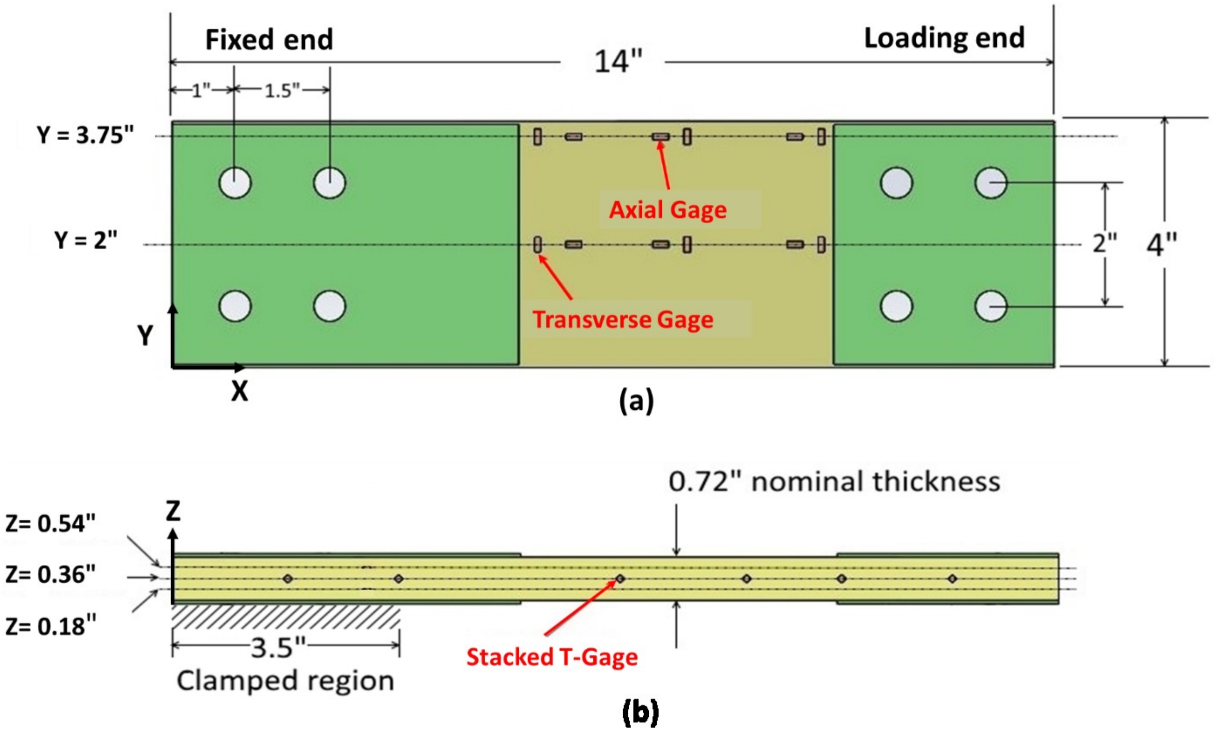

Figure 3-11: Position of the strain gages on the top and side surfaces

Since the strain gages measure strain at points, digital image correlation method was utilized to obtain the full field strain distribution on the surfaces. Digital image correlation (DIC) is a nondestructive and noncontact method to measure both in plane and out of plane deformations on the surfaces. From the available full-field deformations, it is possible to estimate normal and shear strain fields. DIC compares images which are taken from the specimen before and after loading. Obviously, the accuracy of the results depends highly on the quality of the images.

To obtain trustable results from DIC, it is necessary to apply an appropriate black and white speckle pattern to the target surface. In general, a good speckle pattern has evenly distributed but random black and white regions. Two main areas were considered for comparison of the obtained results between FE and DIC. Figure 3-12 illustrates the areas of interest. First area was located on the top of the plate and extended from the edge of the large buffer pads to an X-position of 9.5 inches on the sample. The second area on interest was selected on the thickness side of the plate and included the location of maximum shear strain (obtained during finite element analysis).

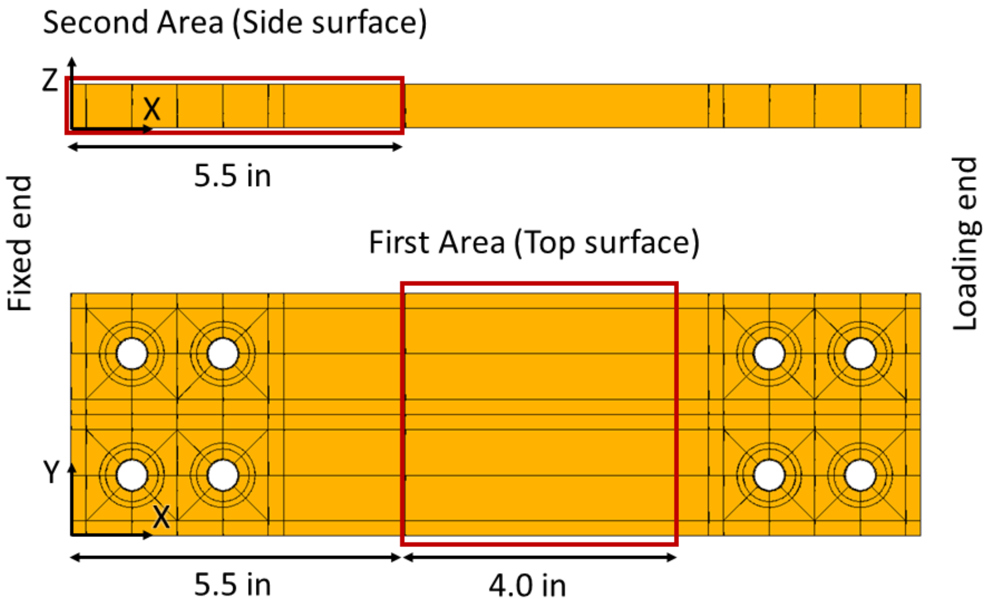

Figure 3-12: Position of the areas of interest on the side and top surfaces of the sample

The next step is to fix a set of stereo cameras which will be carefully calibrated to each other's position and relative to the target surface. For the present study, two cameras were set for each of top and side surfaces of the plate. This camera setup would provide the in plane and out of plane deformations distribution on both surfaces. Figure 3-13 illustrates the DIC test setup.

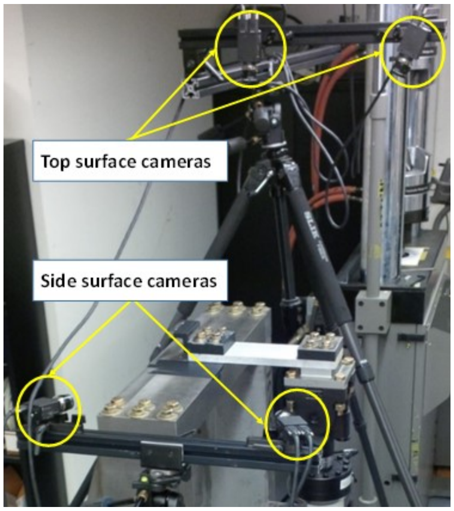

Figure 3-13: Camera setup for DIC of flexural bending model

To obtain deformation and strain field from DIC, a reference image is taken with no load applied on the sample, then more images are taken at desired load levels. The images are then transferred to an analysis software, where the reference image is divided into square subsets of pixels to keep track of the displacement of the speckles through the images. The subset should be defined such that the area of each subset square contains a speckle. A step (in terms of number of pixels) is also defined to determine the number of pixels between each displacement calculation. This correlates to the distance between nodes in finite element analysis (FEA). The smaller the step size, the finer the strain resolution. Finally, a filter size can be set which dictates over how many steps the software averages the strain values for smoothing out noises. The step number multiplied by the filter size determines the diameter (in pixels) of a circle over which the strain is averaged. This circle area is synonymous to the mesh size in FEA. Similarly, to FEA, where a larger mesh gives a smoother strain calculation, albeit at the expense of strain resolution, having a large step X filter number will also give smoother results with lower strain resolution. The best practices in setting up the DIC system and obtaining strain results will not be discussed here. For further information in this regard refer to [106].

3.5.1 Experimental Procedure

Once the sample was prepared for strain gages or DIC investigations, the following procedure was followed:

1. Installing the sample on the test setup with steel clamping plate(s) in place and finger tightening the bolts at the fixed end.
2. Placing the actuator low enough so there is no contact between actuator head and the sample.
3. Setting strain gages to zero or capturing the reference image for DIC.
4. Setting the load cell of the actuator to zero.
5. Tightening the bolts at the fixed end in a cross pattern to 110 ft-lbs (which is suggested by the industrial partner).
6. Moving the actuator up until the point that the adapter meets the sample.

7. Installing the steel block for clamped-clamped or the adapter for cantilever on top of loading end of the sample.
8. For clamped-clamped, tightening the bolts of the steel block with a torque of 110 ft-lbs and for cantilever, torque the bolts of the adapter to 42 ft-lbs.
9. Checking the actuator load cell, if it shows a non-zero value then the position of the actuator should be adjusted to have a zero force in load cell.
10. Capturing the data from strain gages or taking the photos on DIC.
11. Applying displacement-controlled loading to the sample up to the desired displacement level.

Details of the experimental investigation can be found in [107].

3.6 Flexural bending - Results

3.6.1 Flexural bending - FEA vs strain gages

To validate the model, the sample was tested at the actuator displacement of 10 mm and the strain data was recorded. These experimental results were compared to the strain values obtained from simulation at the same loading level. To represent the data, a coordinate system according to Figure 3-12 was defined. To provide a better demonstration of the results, the Z coordinate will be introduced by the percentage of the thickness. In that case, 0% corresponds to Z=0 and 100% corresponds to Z=Thickness of the plate. The strain gages were installed only on the unidirectional clamped-clamped sample according to Figure 3-11. Figure 3-14 compares the axial strain (e_{xx}) at the top surface recorded by the strain gauges to the ANSYS prediction at the similar locations. Figure 3-15 shows the same comparison but for the transverse strain (e_{yy}) at the top surface. It can be seen from these two graphs that FE results correlated well with the gages recorded data for the top surface while the correlation is better for axial strain comparing to transverse strain.

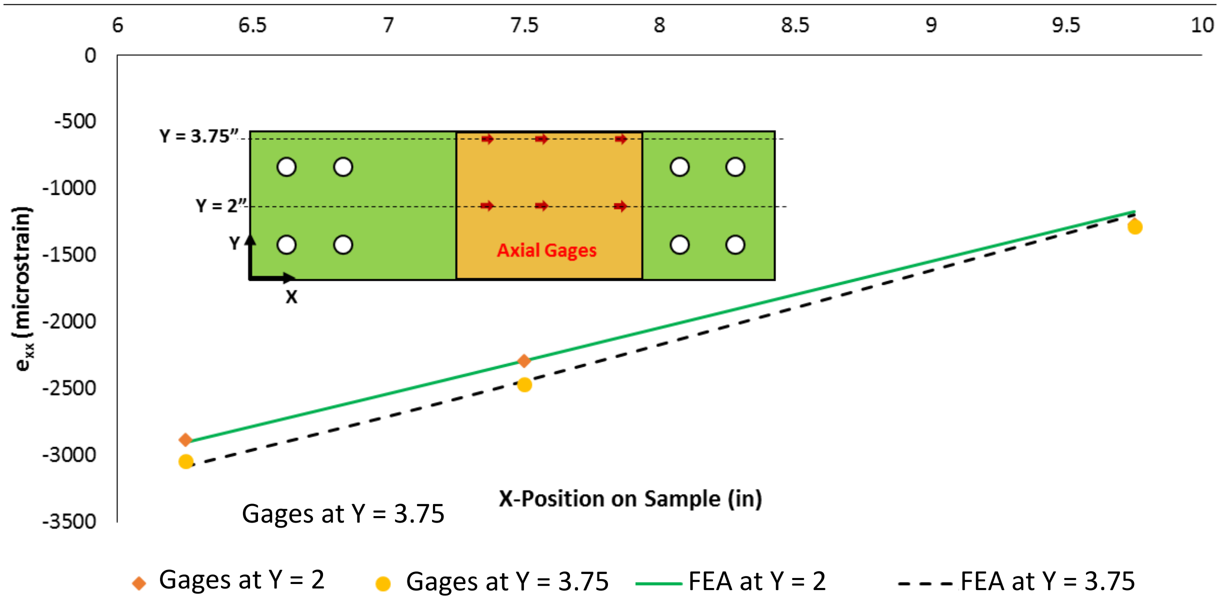

Figure 3-14: Comparison of axial strain on the top surface, FEA vs Gages (unidirectional clamped-clamped)

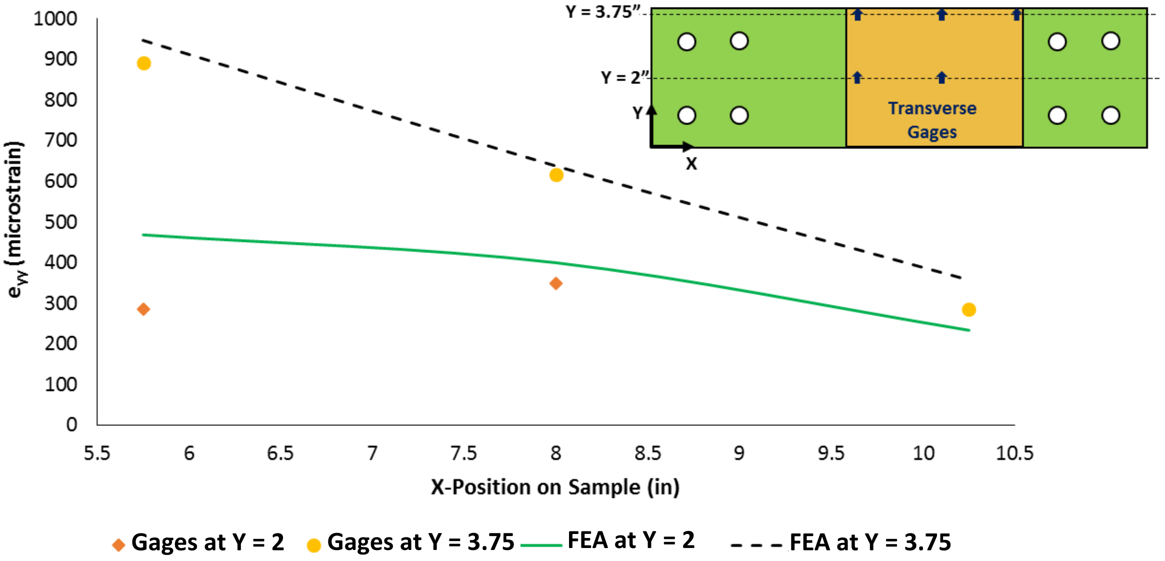

Figure 3-15: Comparison of transverse strain on the top surface, FEA vs Gages (unidirectional clamped-clamped)

For more validation, the strains on the side surface are compared between FE and strain gages. Figure 3-16 shows the shear strain (e_{xz}) at different axial positions on the side surface of the laminate and compares the data recorded by the strain gages with the results obtained from simulation. It is obvious from this figure that ANSYS results correlates very well with the experimental results obtained from the gages. For the final comparison, the axial strains on the side surface were compared for the same axial position but at different thickness. As Figure 3-17 illustrates two axial strain gages were installed at the position of X=5.5 in, Z= 25% and Z=75%. Similar to what was observed for shear strain on the side surface, the model calculated the axial strain on the side surface with a good correlation with the experimental data obtained from strain gages. Although the correlation between strain gages and FEA results was promising, to validate the results not only at points but over a full field distribution, gages results were examined by DIC.

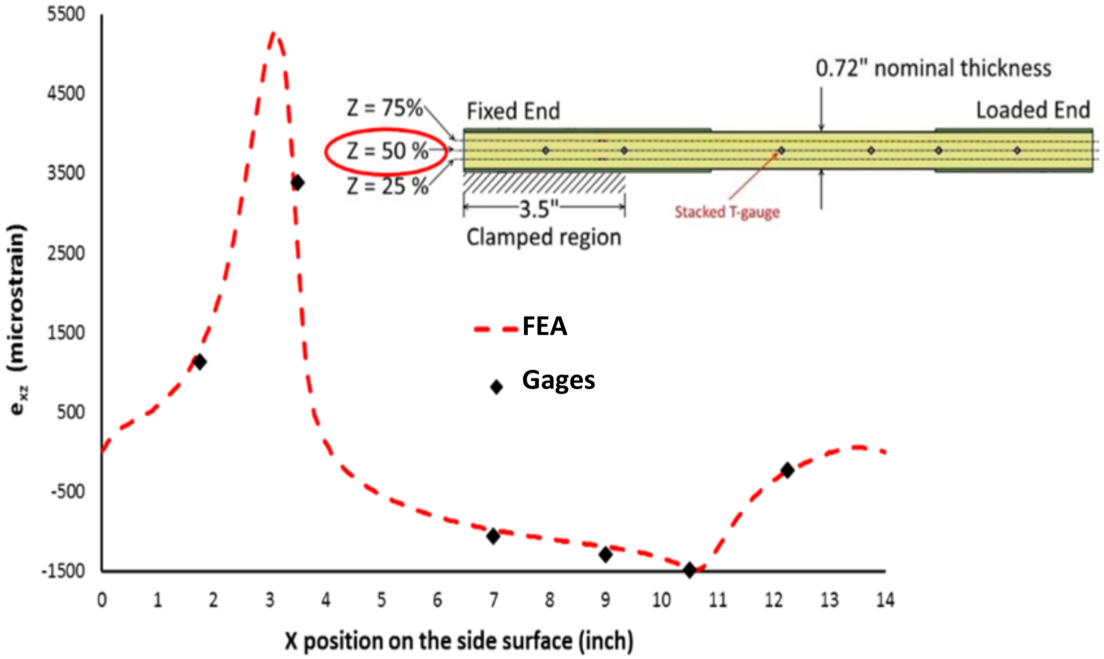

Figure 3-16: Comparison of shear strain (e_{xz}) on the side surface, FEA vs Gages (unidirectional clamped-clamped)

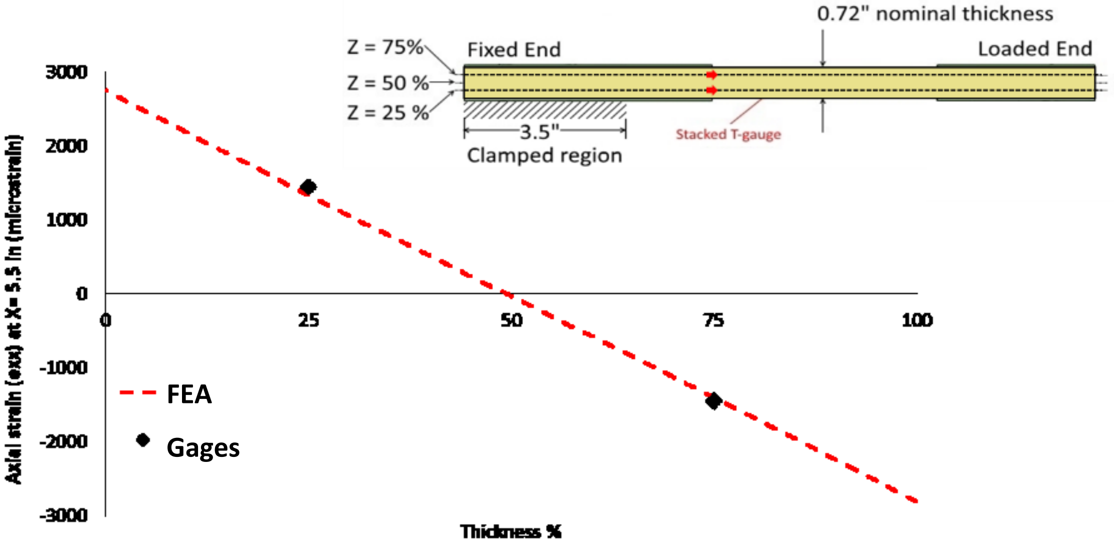

Figure 3-17: Comparison of axial strain (e_{xx}) on the side surface, FEA vs Gages (unidirectional clamped-clamped)

3.6.2 Flexural bending - FEA vs DIC

3.6.2.1 Unidirectional clamped - Top Surface

In this section, the results of the simulation of the clamped-clamped unidirectional model will be compared with the DIC data. Figure 3-18 shows the out-of-plane displacement (U_Z) distribution obtained from ANSYS and DIC on the top surface over the area of interest according to Figure 3-12. It is clear from this figure that numerical results correlated very well with the experimental data qualitatively with a very similar displacement distribution pattern obtained from both approaches. For quantitative comparison, the distribution of the displacement (U_Z) along line AB (refer to Figure 3-18) was extracted from FEA and DIC and is shown in Figure 3-19. According to the graph presented in Figure 3-19, the maximum difference between FE and DIC results along line AB is 11% which shows the good quantitative correlation in terms of the main deflection between two approaches.

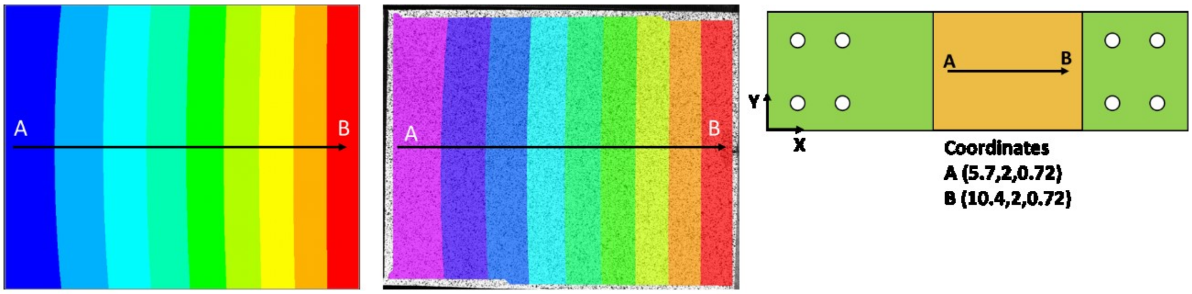

FEA DIC

Figure 3-18: Comparison of out-of-plane displacement (U_Z) for unidirectional clamped-clamped model

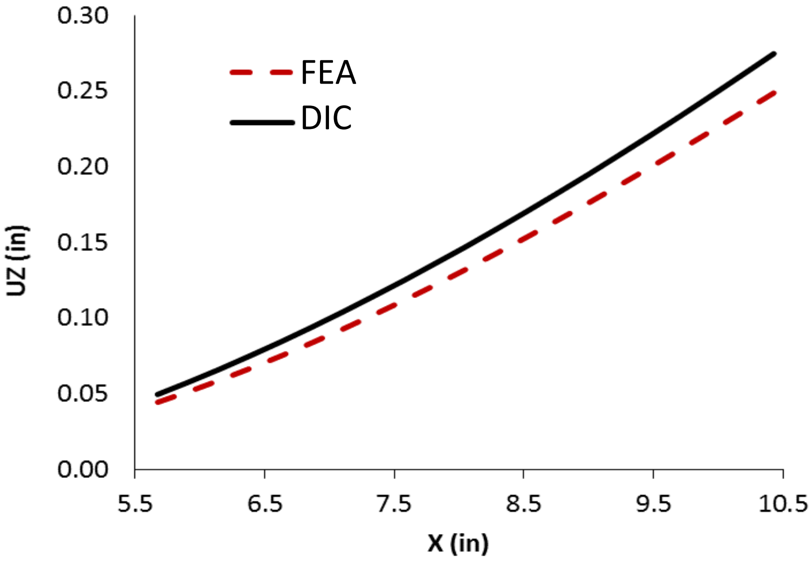

Figure 3-19: Out-of-plane displacement (U_Z) along line AB of Figure 3-18

To evaluate the accuracy of the simulation in terms of the strain distribution and calculation, different strains were investigated on the areas of interest (refer to Figure 3-12).

Figure 3-20 represents the distribution of the axial strain (e_{XX}) on the top surface of the plate. Also, the values of e_{XX} along line AB is compared between numerical and experimental approaches in the graph of Figure 3-21. The graph illustrates a very close correlation between analysis and experiment since the maximum difference was only 9%. For further validation, the same analysis was repeated for both transverse strain and in-plane shear strain over the top surface. Figure 3-22 compares the transverse strain (e_{yy}) distribution pattern obtained from DIC with ANSYS results. As it can be seen, both approaches represent similar distribution pattern of transverse strain on the top surface. Figure 3-23 shows the quantitative comparison of the transverse strain (e_{yy}) along line CD (refer to Figure 3-22). The results, seen in Figure 3-23, showed the maximum error happened at the regions with lower strain was 146 microstrain. Although in terms of percentage of difference this may seem like a large discrepancy, it should be considered that the accuracy of the utilized DIC system was about 50 microstrain which is indicated by the error bars in Figure 3-23 and Figure 3-25. Therefore, especially at low strain levels, such a difference should not be significantly considered. For the final comparison on the top surface of unidirectional clamped-clamped model, the in-plane shear strain (e_{XY}) distribution pattern is shown in Figure 3-24 with the distribution along line EF represented as a graph in Figure 3-25. These figures illustrate that the in-plane shear strain distribution and magnitude correlate well between FEA and DIC. It is noticeable that the error of 50 microstrain associated with the strains obtained from DIC should be considered when it is desired to validate the accuracy of the shear strain prediction on the top surface (refer to Figure 3-25 error bars).

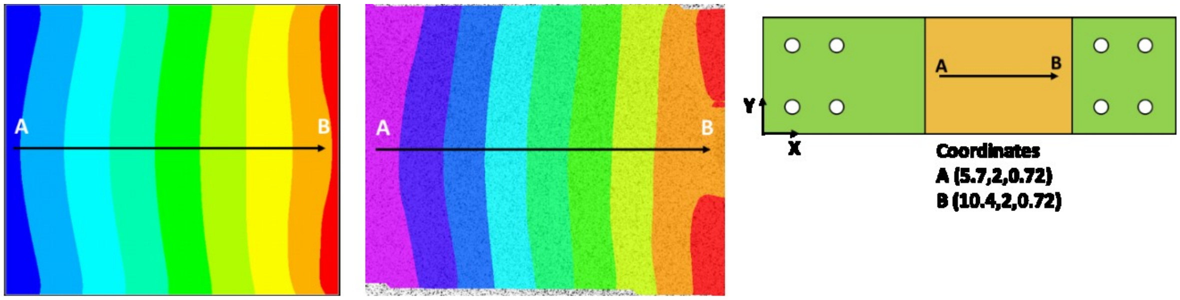

FEA DIC

Figure 3-20: Comparison of axial strain (e_{xx}) on top surface of unidirectional clamped-clamped model

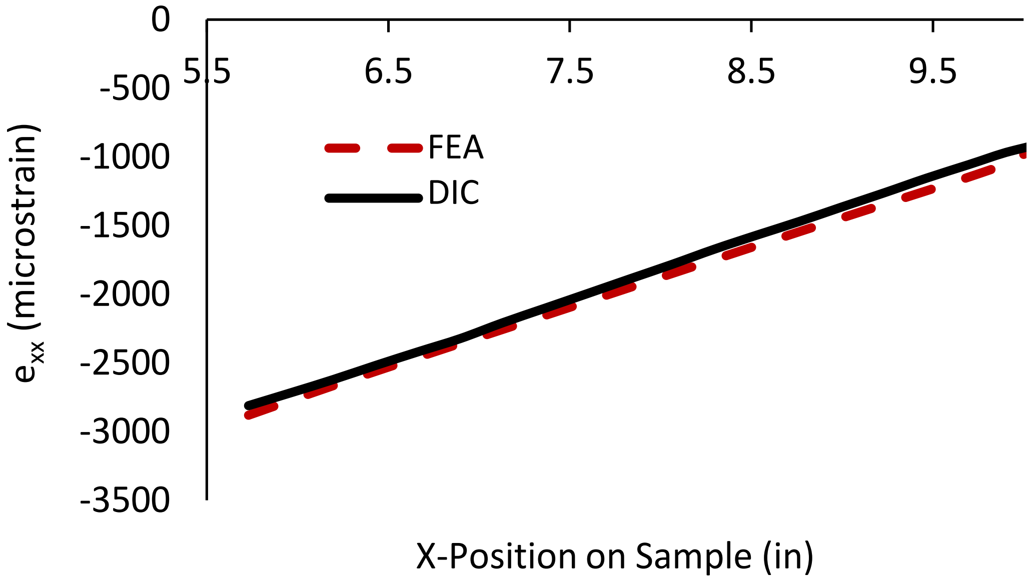

Figure 3-21: Axial strain (e_{xx}) along line AB of Figure 3-20

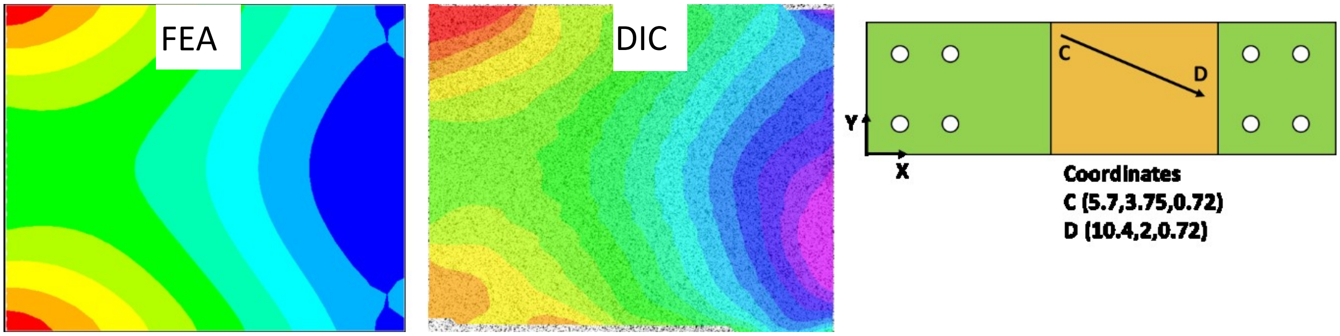

Figure 3-22: Comparison of transverse strain (e_{yy}) on top surface of unidirectional clamped-clamped model

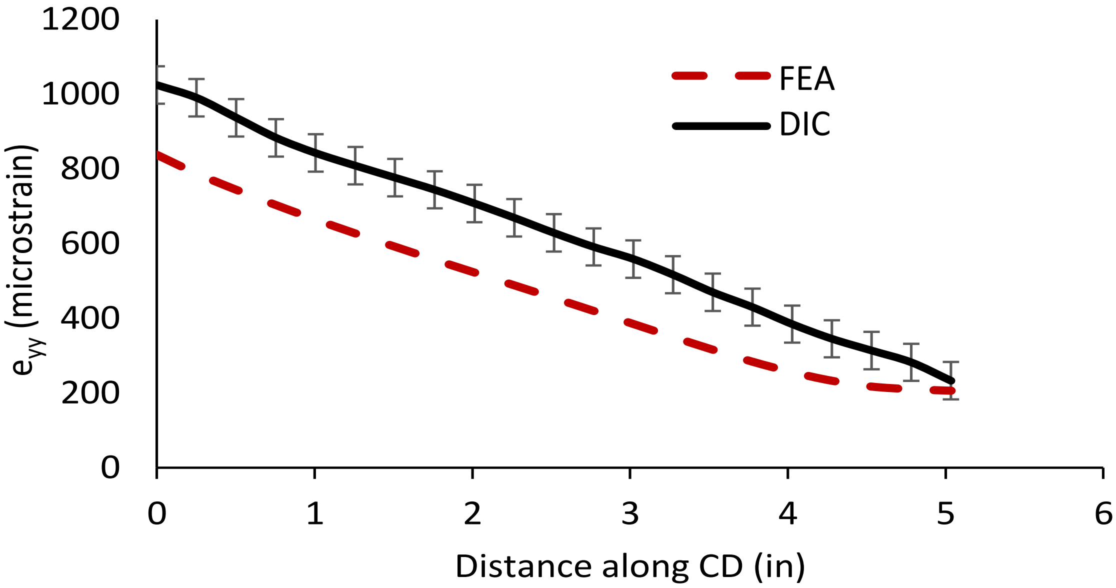

Figure 3-23: Transverse strain (e_{yy}) along line CD of Figure 3-22

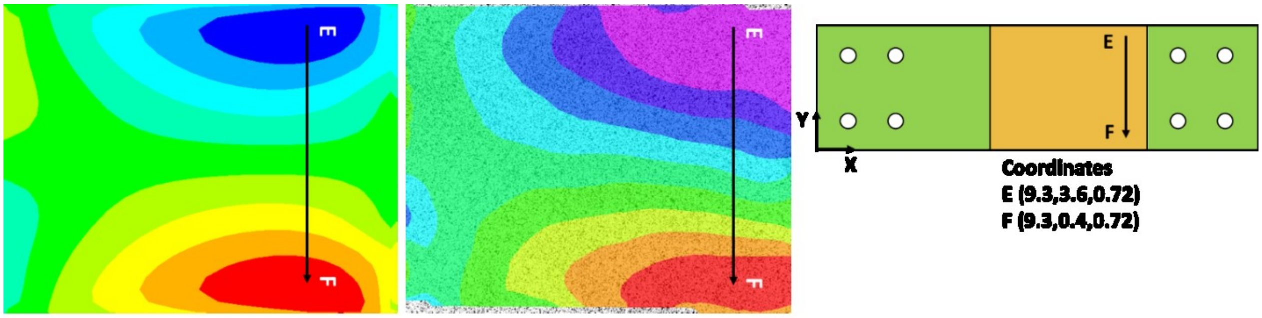

FEA DIC

Figure 3-24: Comparison of the in-plane shear strain (e_{xy}) on top surface of unidirectional clamped-clamped model

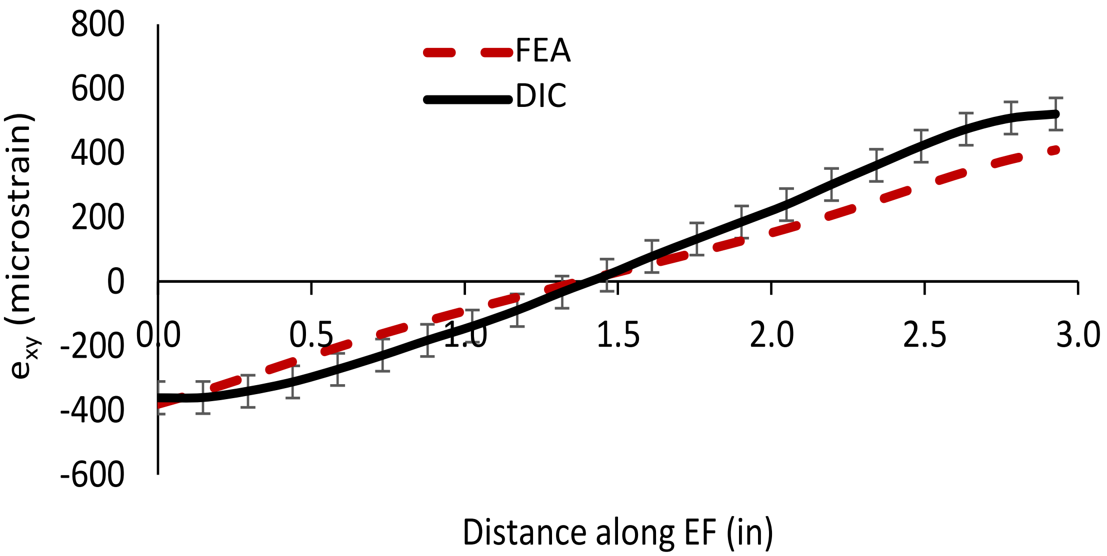

Figure 3-25: In-plane shear strain (e_{xy}) along line EF of Figure 3-24

As it was expected from finite element model a symmetric distribution of the transverse (e_{YY}) and in plane shear (e_{XY}) strains were obtained (refer to Figure 3-22 and Figure 3-24) while some asymmetricities were found in the corresponding DIC patterns. This can be due to improper alignment of the plate with the test setup and variations in surface geometry which would influence more the shear and transverse strains than axial one. Once DIC was employed, is was found that tightening the bolts will cause a slight lateral rotation in the sample (about Y axis). This resulted in a slight twisting of the sample (about the X-axis) while being subjected to the bending. Despite the best efforts to mitigate this phenomenon, it was not completely avoidable because of manufacturing and drilling processes of the plate and the holes. As such, this may have a contribution in some of the discrepancies between ANSYS and DIC results in transverse and in plane shear strains.

3.6.2.2 Unidirectional Clamped - Side surface

The same comparison performed on the top surface was duplicated also for the side surface. Results showed that the critical strains on the side surface are axial (e_{XX}) and interlaminar shear (e_{XZ}). Figure 3-26 and Figure 3-28 show the distribution of e_{xx} and interlaminar shear strain (e_{xz}), respectively, over the area of the interest on the side surface (refer to Figure 3-12). The area of interest was selected based on preliminary ANSYS results that indicated this region includes the location of maximum shear strain. As it was expected during upward bending, compressive strains appeared at upper half and tensile strains at lower half of the laminate thickness. The axial strain distribution along line GH from Figure 3-26 is illustrated in Figure 3-27. It can be observed that finite element simulation is in a close correlation with the DIC experiment data. The difference between maximum axial strains (e_{XX}) on side surface obtained from the two approaches was 7%. Figure 3-29 shows the distribution of shear strain (e_{xz}) along line IJ from Figure 3-28. These figures reveal that the model and the experimental data match both qualitatively and quantitatively. The maximum interlaminar shear calculated by ANSYS was 5752 microstrain while DIC data recorded 5734, which corresponds to a difference of less than 0.5%. It can also be seen in Figure 3-29 that the model prediction about the position of maximum interlaminar shear strain on the side surface correlates with what was observed during DIC test. When it came to measuring shear strain with the strain gauges, the difficulty in properly applying the gauges resulted in many malfunctioning ones. As such, extra care was taken to ensure is was done correctly. The results will be discussed in the following.

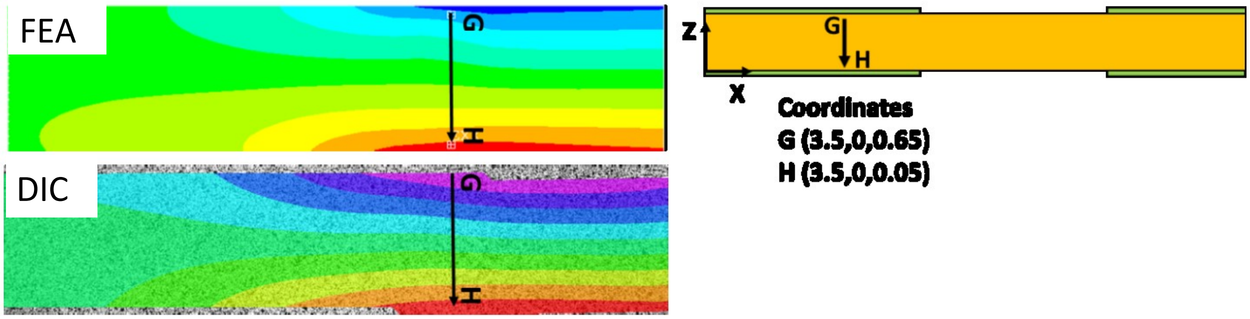

Figure 3-26: Comparison of through thickness axial strain (e_{xx}) of the unidirectional clamped-clamped model

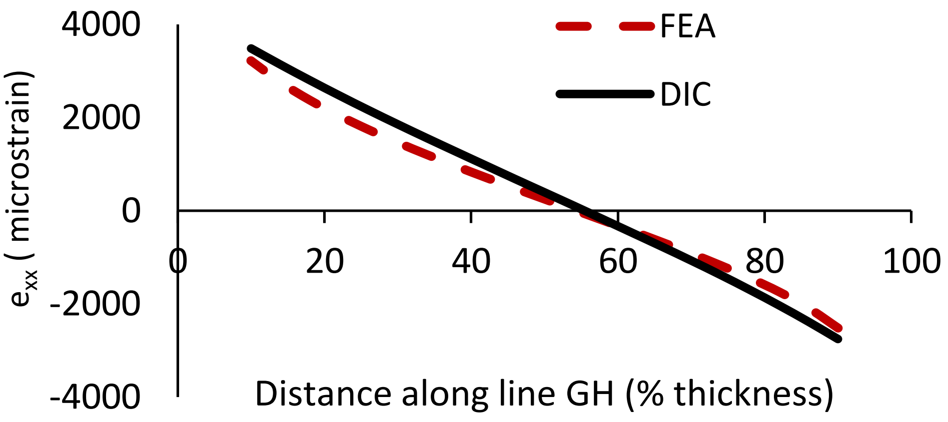

Figure 3-27: Axial strain (e_{xx}) along line GH of Figure 3-26

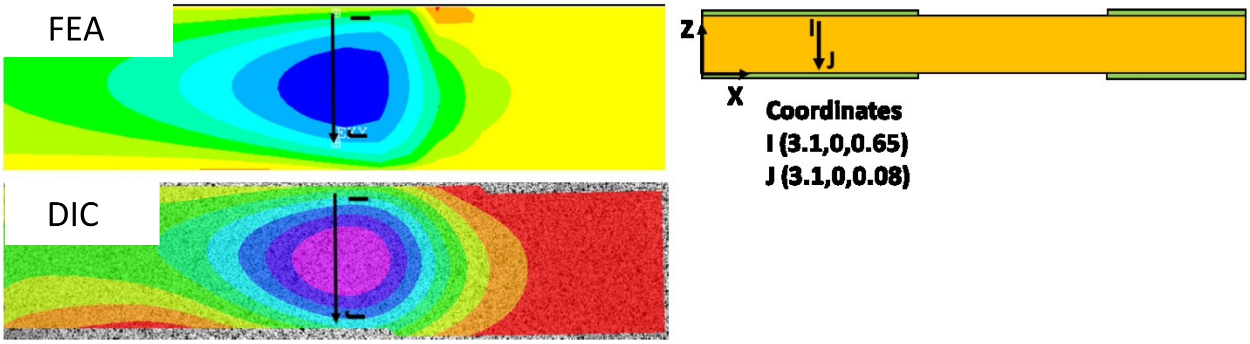

Figure 3-28: Comparison of the through thickness shear strain (e_{xz}) of the unidirectional clamped-clamped model

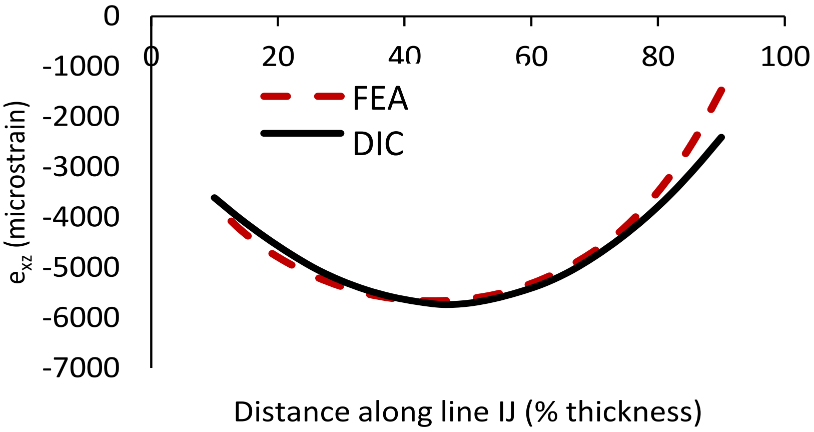

Figure 3-29: Shear strain (e_{xz}) along line IJ of Figure 3-28

3.6.2.3 Unidirectional Clamped – Ultimate strains

Since the points at which the ultimate strains were calculated by analysis were not necessarily located in the areas of interests where DIC data was available, the maximum and minimum strains at top and side surface were obtained based on the DIC results. Then they were compared to the corresponding value of the strain calculated by FEA at the same position. To locate the exact position in the model that corresponds to the position of ultimate strain found in DIC, the area considered by DIC (in terms of pixels) was mirrored to the same area in ANSYS (in terms of inch). Table 3-5 and Table 3-6 summarize the ultimate strain values obtained from DIC and their locations at the top and side surfaces. These tables also compare ultimate strains obtained from DIC with the corresponding FE calculation at the same position. In addition, the maximum difference between ANSYS and DIC results corresponding to each strain is represented in the same tables. Figure 3-12 introduces the coordinate system used to represent the position of the points. It can be obviously concluded that the correlation between the results are much better at higher strains and in areas where the strains are critical. As part of the DIC evaluation process, one T-gauge was placed on the thickness side of the sample on the midplane at an X-position of 3.1 inches. This was where model predicted the maximum shear strain. The strain gauge registered 5800 microstrain, which is very close to both the FEA and DIC results in Table 3-6.

Table 3-5: Ultimate strains at the top surface, unidirectional clamped-clamped

	e_{xx}				**e_{yy}**				**e_{xy}**	
	Minimum		**Maximum**		**Minimum**		**Maximum**		**Maximum**	
Position (in)	**X**	**Y**	**X**	**Y**	**X**	**Y**	**X**	**Y**	**X**	**Y**
Position (DIC)	5.8	2.0	10.4	2.0	10.3	1.22	5.7	3.9	8.0	0.4
Strain-DIC	-2976		-513		188		1024		520	
Strain-FEA	-2916		-592		227		838		405	
% Difference	2.02		15.4		20.7		18.2		22.1	

Table 3-6: Ultimate strains on the thickness side, unidirectional clamped-clamped

	e_{xx}				**e_{xz}**	
	Minimum		**Maximum**		**Maximum**	
Position (in)	**x**	**z**	**x**	**z**	**x**	**z**
Position (DIC)	3.6	0.72	3.6	0.06	3.1	0.33
Strain-DIC	-3090		3486		5734	
Strain-FEA	-2956		3227		5660	
% Difference	4.3		7.4		1.3	

3.6.2.4 Unidirectional cantilever

The unidirectional cantilever model accuracy validates by following the same method as represented before for unidirectional clamped-clamped model. Figure 3-30 illustrates the out of plane displacement (U_Z) distribution on the top surface and along the line (AB). As it can be seen there is a good correlation between the main displacement profile between DIC and FEA results. For the sake of brevity only the main strains were compared between DIC data and ANSYS results in this section. Figure 3-31 shows the axial strain (e_{xx}) on the top surface of the laminate. The maximum difference between experiment and simulation at the top surface is less than 8% for axial strain. Similar to the clamped-clamped model, it was found that transverse (e_{yy}) and in plane shear (e_{xy}) strains have more deviation from the experimental test results, but considering the accuracy of the DIC calculations which is ±50 micro strain, showed that the results are still in good agreement with DIC. The results of transverse and in plane shear strain on the top surface are not presented here.

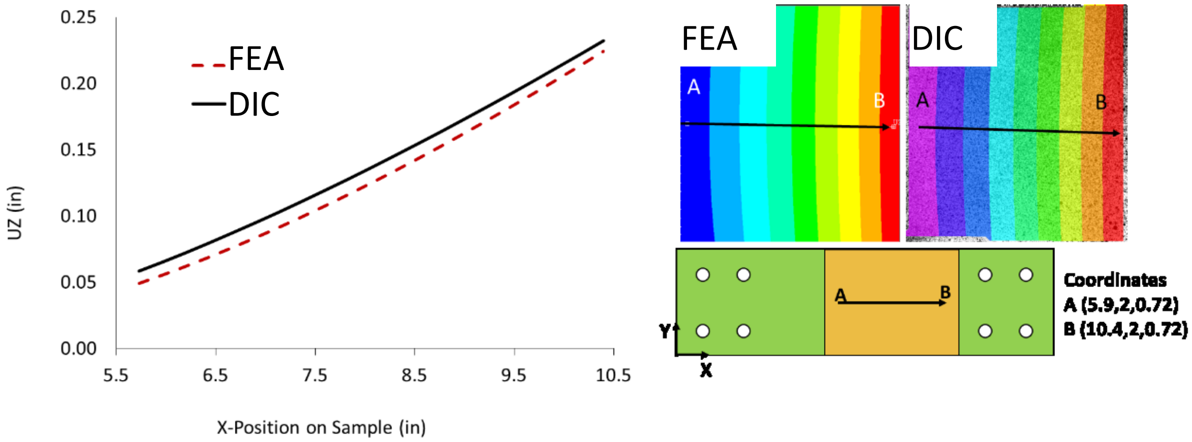

Figure 3-30: Comparison of out-of-plane displacement (UZ) for unidirectional cantilever model

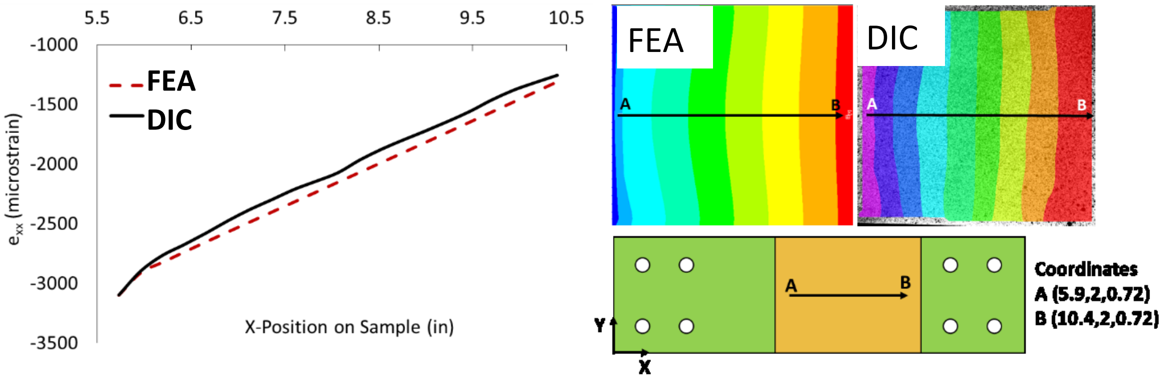

Figure 3-31: Comparison of axial strain (e_{xx}) on top surface for unidirectional cantilever model

For the thickness side of the unidirectional cantilever model, the strain distribution on the side surface and along the corresponding lines are shown in Figure 3-32 and Figure 3-33. The axial strain matches very well with experiment. While for the interlaminar shear strain, the perfect correlation obtained in clamped-clamped model (refer to Figure 3-29) was not achieved here, but the difference between the ultimate values was 15% which still shows an acceptable correlation.

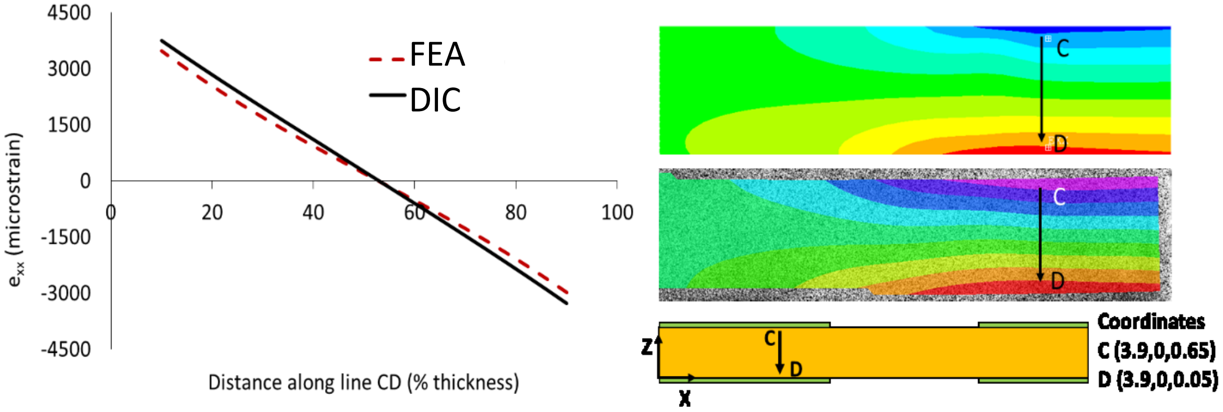

Figure 3-32: Comparison of axial strain (e_{xx}) on thickness surface for unidirectional cantilever model

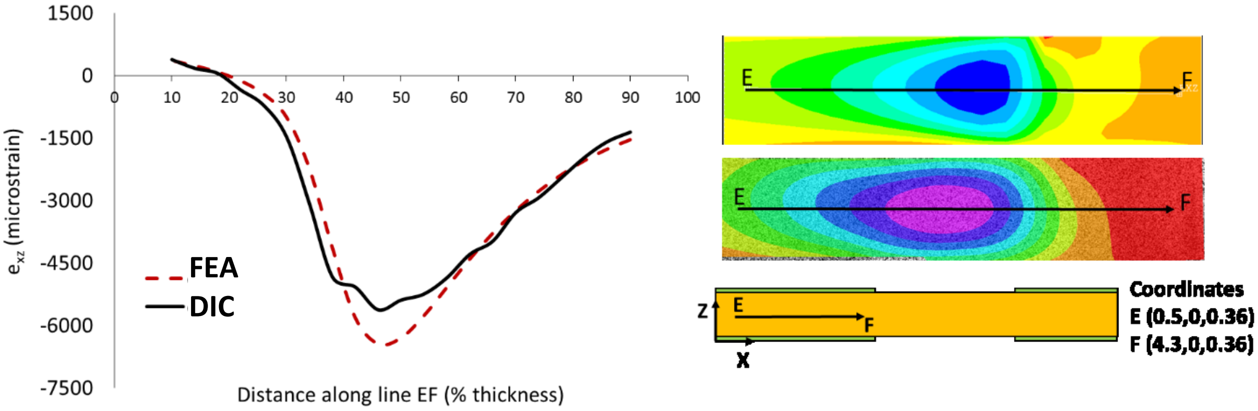

Figure 3-33: Comparison of interlaminar shear strain (e_{xz}) on thickness surface for unidirectional cantilever model

Table 3-7 summarizes the ultimate strain results obtained from DIC for each critical strain on both top and side surfaces and compares them to the strain at the same position calculated by FEA. Once again, a very good agreement was obtained for the high-level strains except for the shear strain on the surface side which showed acceptable correlation.

Table 3-7: Unidirectional cantilever ultimate strains

	e_{xx} (Top)				**e_{xx} (Side)**				**e_{xz} (Side)**	
	Minimum		**Maximum**		**Minimum**		**Maximum**		**Maximum**	
Position (in)	X	Y	X	Y	X	Z	X	Z	X	Z
Position (DIC)	5.6	2.0	10.4	2.0	3.5	0.68	3.5	0.07	2.9	0.36
Strain-DIC	-3097		-1256		-3273		3750		5622	
Strain-FEA	-3099		-1312		-2990		3473		6443	
% Difference	0.06		4.5		8.6		7.4		14.6	

3.6.2.5 Cross ply cantilever

A cross-ply laminate with the same number of layers was selected for further investigation. The laminate was manufactured using the same material as indicated for unidirectional plates. The layer sequence of this laminate was $[0/90]_{20S}$. The model was modified to create the desired layer sequence. In this section, only the top surface axial strains (e_{xx}), and side surface axial (e_{xx}) and shear strains (e_{xz}) are compared between FEA and DIC results due to their higher significance. Figure 3-34, Figure 3-35, and Figure 3-36 illustrate the axial strain at the top, axial strain along the thickness and interlaminar shear strain on the thickness side, respectively. It is obvious from these figures the that results obtained from ANSYS and DIC correlate very well with each other for cross ply cantilever model. Table 3-8 compares the ultimate values obtained from experimental and finite element analysis for the main strains mentioned above.

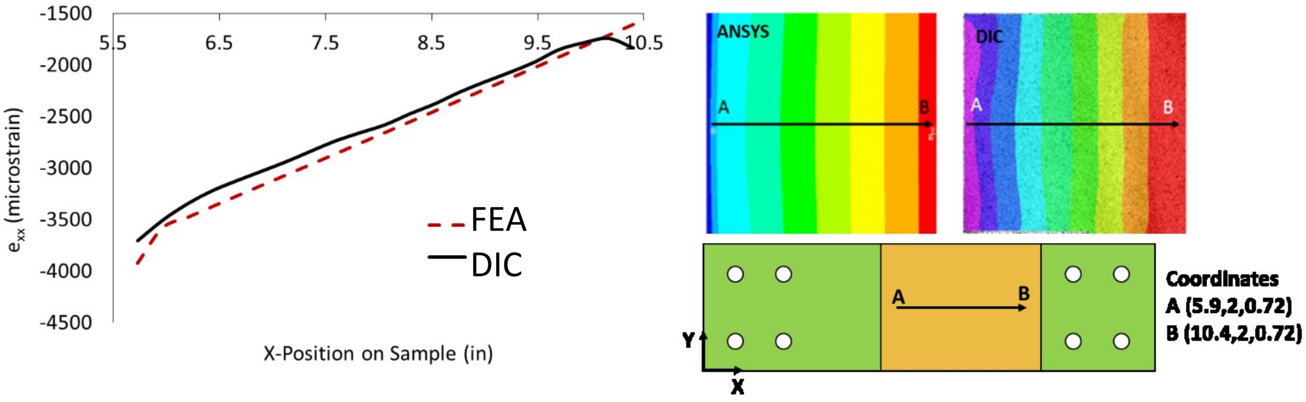

Figure 3-34: Comparison of axial strain (e_{xx}) on top surface for cross-ply cantilever model

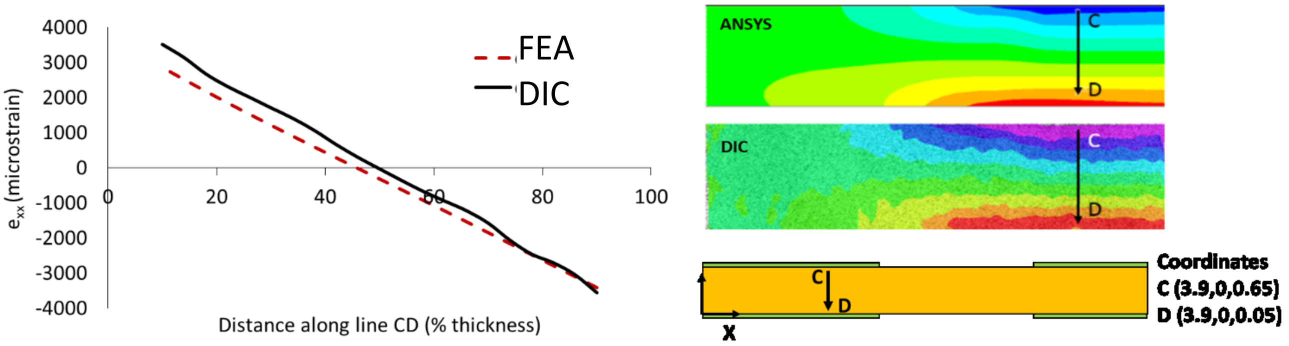

Figure 3-35: Comparison of axial strain (e_{xx}) on thickness side for cross-ply cantilever model

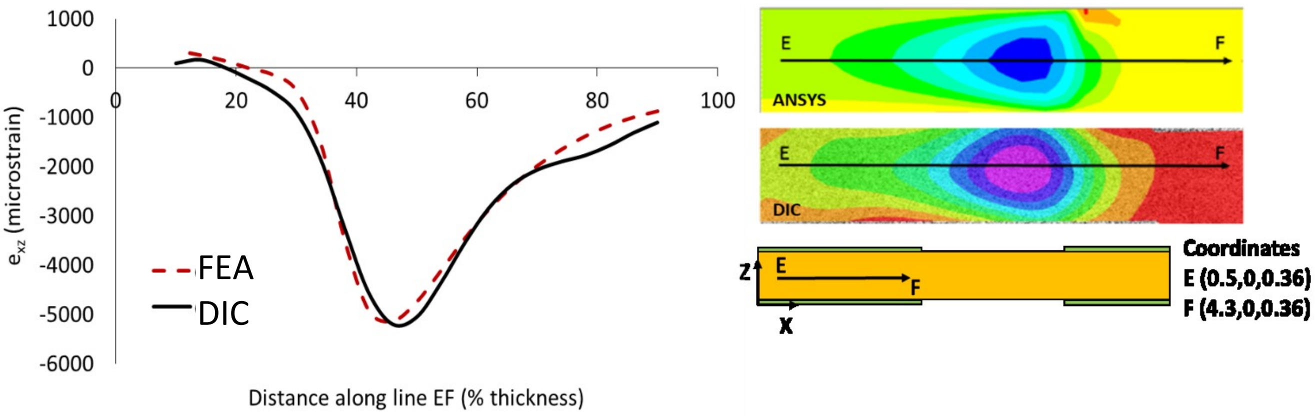

Figure 3-36: Comparison of interlaminar shear strain (e_{xz}) on thickness side for cross-ply cantilever model

Table 3-8: Ultimate strain comparison for cross-ply cantilever model

	e_{xx} (Top)				e_{xx} (Side)				e_{xz} (Side)	
	Minimum		**Maximum**		**Minimum**		**Maximum**		**Maximum**	
Position (in)	X	Y	X	Y	X	Z	X	Z	X	Z
Position (DIC)	5.6	2.0	10.2	2.0	3.9	0.68	3.9	0.09	3.1	0.42
Strain-DIC	-3706		-1742		-3558		3515		5197	
Strain-FEA	-3921		-1605		-3406		2866		5132	
% Difference	5.8		7.8		4.3		18.4		1.25	

Results showed a good correlation both qualitatively and quantitatively, between strains obtained from numerical analysis and DIC experimental data, as well the installed strain gauges.

As DIC is more practical in areas with higher strains, for the regions with ultimate strains the difference between DIC and ANSYS was less than 5% for most of the cases, which is a significant achievement in terms of the correlation with experiments. DIC also provides the benefit of full field strain measurement over the spot measurements provided by strain gauges. The proposed model accuracy in terms of strain prediction is higher for main strains (E.g. axial strain e_{xx} and interlaminar shear strain e_{xz}). For the regions with lower strain (less than 500 microstrains), the correlation is not as good compared to the other areas. However, by considering the accuracy of the DIC (about 50 microstrain), the results are still in an acceptable agreement with DIC. In addition, a slight twisting of the sample about the Y-axis due to a very small misalignment of the holes (caused by holes drilling), may have contributed to some of the discrepancies between ANSYS and DIC, such as the lack of symmetry in the top surface strain distributions recorded by DIC.

The model is able to predict the strain in both cantilever and clamped-clamped boundary conditions. In addition, it was validated in both unidirectional and cross-ply layup sequences. The FE model required some simplifications in terms of geometry and load application to be able to be run within a reasonable time frame. These must be taken into consideration when analyzing the results, especially for failure. Comparison of the axial strain at the same position between cross ply and unidirectional plates revealed that the cross-ply samples behaved expectedly less stiff than the unidirectional counterparts by about 30%.

Due to the nature of the sample manufacturing process (i.e. vacuum bagging parts instead of cavity moulding), the sample did not have perfectly parallel surfaces from resin bleeding from the corners. This may be another source of discrepancy between FEA, DIC, and strain gauge results.

3.7 Flexural bending - Thickness investigation

To examine the feasibility of the proposed finite element model for the plates with different number of layers, unidirectional plates with 20, 40, and 60 layers were manufactured. These plates were tested using the cantilever configuration and digital image correlation were utilized to find the strain distribution on the surface. In the following the results obtained from FEA and DIC will be compared.

Figure 3-37 shows the out of plane displacement (U_Z) and axial strain (e_{xx}) on the top surface for the plate consisting of 20 unidirectional layers at 10 mm upward displacement of the actuator. Although the out of plane displacement correlated well between ANSYS and DIC for the 20 layers plate, the axial strain did not show a good agreement. This fact illustrates that the model can predict the behavior of the plate in Z direction while for the axial direction it is not feasible. Since the plate is thin, it is affected highly by the cantilever fixture at the loading end which is not included in the finite element model. The cantilever fixture effect changes the axial displacement of the sample (the displacement in X direction). This phenomenon was also observed when the axial displacements on the top surface obtained from FEA and DIC were compared. The difference between the results in axial direction was higher at the locations closer to the loading end.

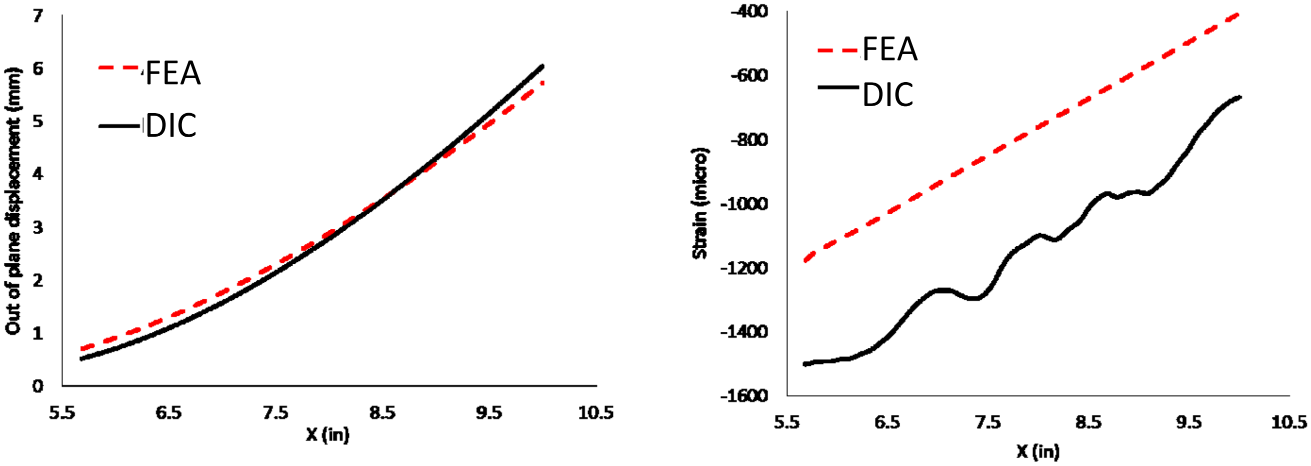

Figure 3-37: Validation for 20-layer unidirectional plate (U_Z and e_{xx} on the top surface)

Figure 3-38 illustrates the out of plane displacement and axial strain on the top surface of the unidirectional sample with 40 layers. As it can be seen the out of plane displacement correlates better close to the fixed end. Similar to what was observed for 20-layer plate, the effect of the cantilever fixture (which is not considered in the finite element model) is more evident at higher X position (closer to the loading end of the plate). Results obtained for axial strain distribution showed a better correlation between FEA and DIC for 40-layer plate comparing to the plate consisting of 20 layers. The accuracy of the DIC for strain calculation (± 50 micro strain) is shown as error bars in Figure 3-38.

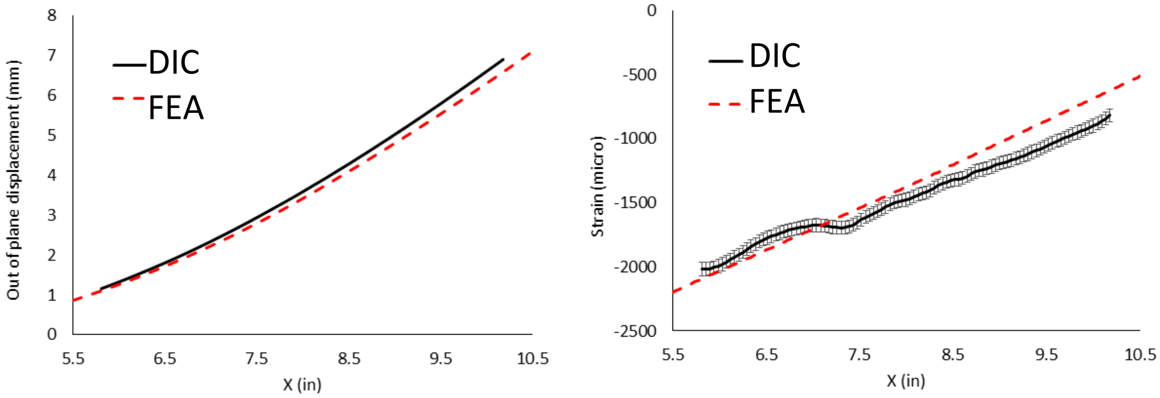

Figure 3-38: Validation for 40-layer unidirectional plate – Top surface

Unfortunately, the 20-layer plate thickness was not enough to provide the detectable results in thickness side. For 40-layer sample, the distribution of the interlaminar shear strain (e_{xz}) along the thickness and around the front lane bolt joints is shown in Figure 3-39. It is obvious from this figure that the ANSYS and DIC results agreed very well qualitatively. The maximum shear strain obtained from FEA was 2900 micro strains while from DIC it was obtained as 2650 micro strains. Comparing the maximum shear strain values represents less than 10% of difference which reveals a good quantitative agreement.

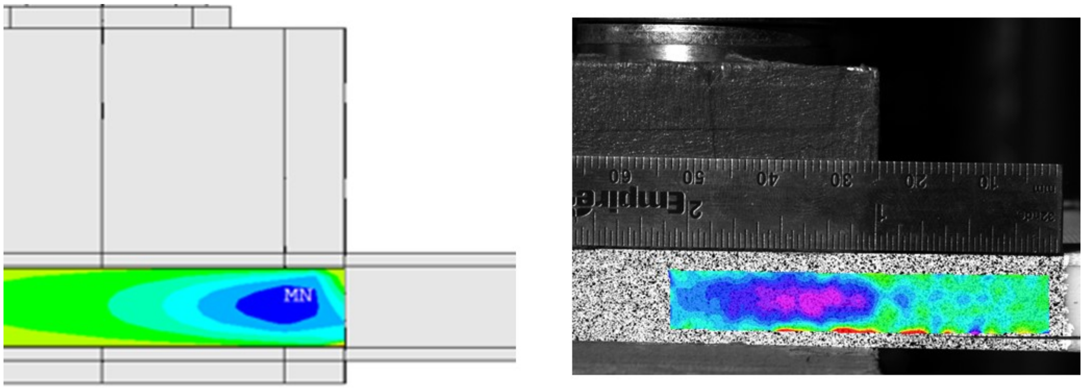

Figure 3-39: Validation for 40-layer unidirectional plate – Side surface

The same analysis was repeated for the 60-layer plate. Figure 3-40 shows a good correlation of the axial strain distribution on the top surface. Also, the maximum difference of the out of plane distribution on the top surface is less than 10%. Figure 3-41 illustrates the qualitative comparison of the interlaminar shear strain (e_{xz}) on the side surface between ANSYS and DIC. The maximum shear strain on the side surface was obtained 3900 micro strain from DIC and 4300 micro strain from FEA which represents 10% of discrepancy.

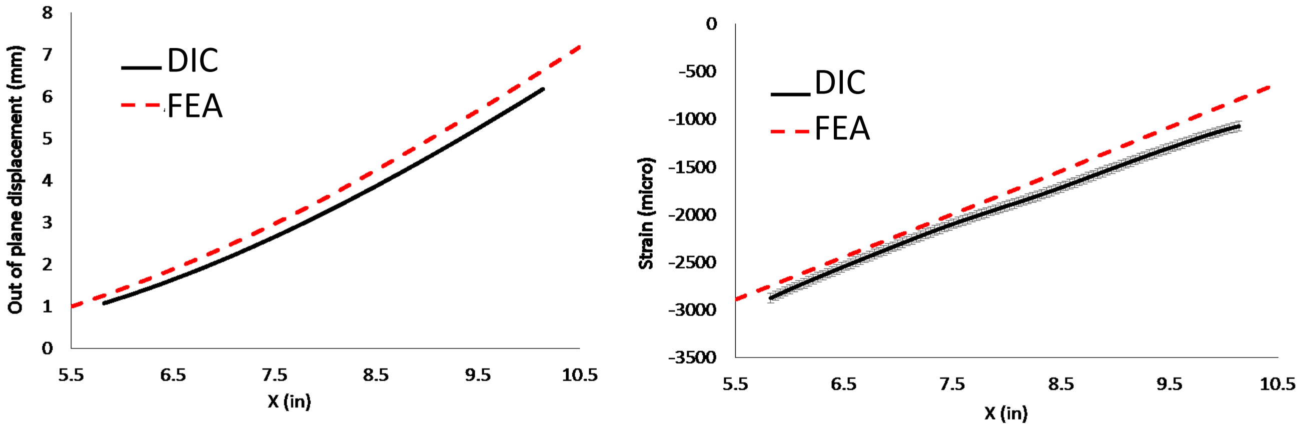

Figure 3-40: Validation for 60-layer unidirectional plate – Top surface

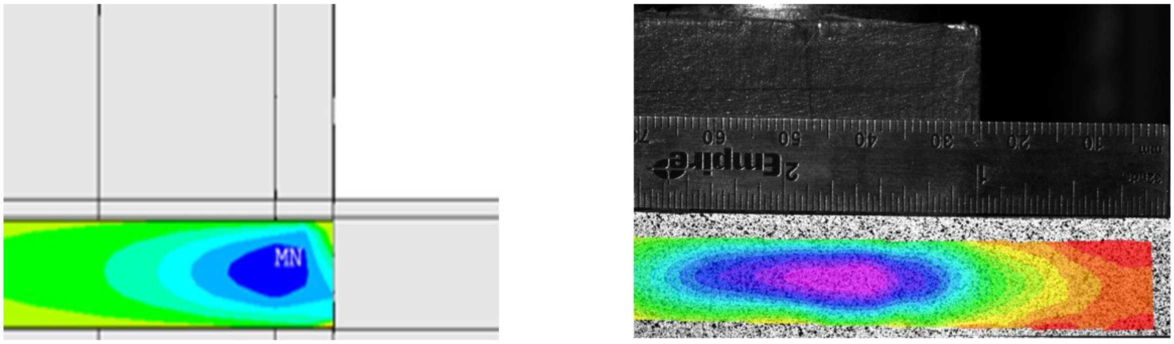

Figure 3-41: Validation for 60-layer unidirectional plate – Side surface

To summarize, the model is able to simulate the structural behavior of the plates with different thicknesses. As it was obtained from the results for cantilever unidirectional samples, the effect of the loading fixture which is not simulated in the finite element analysis, causes some discrepancies between numerical results and experimental data. This discrepancy was higher for the points located closer to the fixture (loading end). Also, the thinner plates are more sensitive to the loading mechanism affects.

4 Failure Analysis

4.1 Failure Modeling

A Progressive Damage Model (PDM) was developed in this study to predict failure initiation and propagation in the plate subjected to different loading and boundary conditions. The process of progressive damage modeling is illustrated in Figure 4-1. PDM starts with the stress analysis of an initial model to find the state of stress at each element. Once the local state of stress is identified for each single element of the model, an appropriate failure criterion should be utilized to distinguish the elements which are already failed at the present loading condition within the whole model.

There are different failure criteria for composite materials in the literature[108]. Hashin criterion was introduced as a three dimensional failure criterion for unidirectional fiber composites[109]. It was established in terms of quadratic stress polynomials. In this study a Hashin-type failure criterion was utilized. Table 4-1 summarizes the Hashin and the utilized Hashin-type (as it was reported by Shokrieh et al[110]) failure criteria. In Table 4-1, σ_{ij} represents the local state of stress at each element and the denominators are the respective strength. Since a full three-dimensional finite element model was developed, a local state of stress would be provided at each element.

The advantage of Hashin-type failure criterion is the ability to distinguish between different failure modes. It will provide the designer with additional information about the failure mechanism and the dominant stress or stresses which contribute to the final failure. The main differences between the Hashin-type criterion and the original Hashin criterion are:

1. The Hashin-type criterion can be applied to all orthotropic materials while Hashin criterion is only suitable for unidirectional fiber composites.
2. The Hashin-type criteria has an additional failure mode (Table 4-1, Failure mode 5) which was suggested by Lessard [111] to consider the effect of in-plane shear stress.

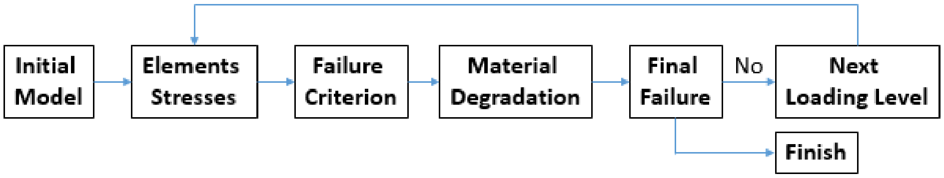

Figure 4-1: The Progressive Damage Model process

Table 4-1: Hashin vs Hashin-type failure criteria

Failure Mode		Criteria	
1	Matrix tensile	Hashin	$\frac{1}{Y_T^2}(\sigma_{yy}+\sigma_{zz})^2+\frac{1}{S_T^2}(\sigma_{yz}^2-\sigma_{yy}.\sigma_{zz})+\frac{1}{S_A^2}(\sigma_{xy}^2+\sigma_{xz}^2)\geq 1$
		Hashin-type	$(\frac{\sigma_{yy}}{Y_T})^2+(\frac{\sigma_{xy}}{S_{xy}})^2+(\frac{\sigma_{yz}}{S_{yz}})^2\geq 1$
2	Matrix compressive	Hashin	$\frac{1}{Y_C}[(\frac{Y_C}{2S_T})^2-1](\sigma_{yy}+\sigma_{zz})+\frac{1}{4S_T^2}(\sigma_{yy}+\sigma_{zz})^2+\frac{1}{S_T^2}(\sigma_{yz}^2-\sigma_{yy}.\sigma_{zz})$ $+\frac{1}{S_A^2}(\sigma_{xy}^2+\sigma_{xz}^2)\geq 1$
		Hashin-type	$(\frac{\sigma_{yy}}{Y_C})^2+(\frac{\sigma_{xy}}{S_{xy}})^2+(\frac{\sigma_{yz}}{S_{yz}})^2\geq 1$
3	Fiber tensile	Hashin	$(\frac{\sigma_{xx}}{X_T})^2+\frac{1}{S_A^2}(\sigma_{xy}^2+\sigma_{xz}^2)\geq 1$
		Hashin-type	$(\frac{\sigma_{xx}}{X_T})^2+(\frac{\sigma_{xy}}{S_{xy}})^2+(\frac{\sigma_{xz}}{S_{xz}})^2\geq 1$
4	Fiber compressive	Both	$(\frac{\sigma_{xx}}{X_C})\geq 1$
5	Fiber-Matrix shear out	It was introduced by Lessard [111].	
		Hashin-type	$(\frac{\sigma_{xx}}{X_C})^2+(\frac{\sigma_{xy}}{S_{xy}})^2+(\frac{\sigma_{xz}}{S_{xz}})^2\geq 1$
6	Delamination tensile	Hashin-type	$(\frac{\sigma_{zz}}{Z_T})^2+(\frac{\sigma_{xz}}{S_{xz}})^2+(\frac{\sigma_{yz}}{S_{yz}})^2\geq 1$

7	Out of plane compressive	Hashin-type	$(\frac{\sigma_{zz}}{Z_C})^2 + (\frac{\sigma_{xz}}{S_{xz}})^2 + (\frac{\sigma_{yz}}{S_{yz}})^2 \geq 1$
X: Fiber Direction Y: Transverse to fibers Z: Thickness direction T: Tensile C: Compressive For Hashin criterion: $S_T = S_{yz}$ *and* $S_A = S_{xy} = S_{xz}$			

In the next phase, the material properties of the identified failed elements will be degraded according to the failure mode of each element. The degrading percentage is defined as a parameter in finite element code which is under control of the designer. It is noticeable that for the sake of simplicity, a single degradation percentage was defined in this research to be applied in different degradation scenarios. However, the model can be improved by considering different degradation percentages for different modes of failure or degradations percentages related to the failure severity. The selection of the optimum material degradation percentage is out of the scope of this study. A very small degradation percentage will increase the running time of the analysis while a significantly high percentage can cause the solution convergence problems. Here in this research the degradation percentage was selected based on the literature [112] and some trial and errors. In this study four degradation scenarios were defined (refer to Table 4-1 for failure modes):

1. Matrix degradation: Applied to failure modes 1 and 2 and reduction in E_Y, G_{XY} and G_{YZ}.
2. Fiber degradation: Applied to failure modes 3 and 4 and reduction in all material properties.
3. Shear out degradation: Applied to failure mode 5 and reduction in G_{XY}.
4. Delamination degradation: Applied to failure modes 6 and 7 and reduction in E_Z, G_{XZ} and G_{YZ}.

The scenario numbers 1, 3 and 4 are not able to be overwritten by each other while the scenario number 2 can be applied on an element which is already degraded by other scenarios. In the other words, if one element fails due to matrix failure, shear out or delamination it may only fail again due to fiber failure at a higher level of loading. After degradation process, the whole structure will be checked for final failure. The final failure can be defined based on:

1. The stiffness of the joint.
2. The propagation of the damage

In the first approach, the part will reach the final failure when the load-displacement curve experiences an abrupt and significant drop which can be interpreted as sudden drop in the stiffness of the joint. Here in this study, the propagation of the damage was considered as the criterion to check the final failure. In better words, to stop the loop of PDM process (will be explained later in detail for each of the study cases). Eventually, if the final failure occurred the model stops if not the load will be increased, and the process will be restarted from static analysis.

4.2 Failure analysis - Bolt joint

In the first analysis, the failure mechanism of thick composites subjected to the bolt joint load was investigated. In this study, the plate was subjected only to the clamping force of the bolt joint. To investigate the failure, the clamping torque was gradually increased up to the point at which the failure was visually detectable on the surfaces of the laminate. Therefore, the final failure of the specimen is defined as the point where crack reaches the outward surface of the sample. For the case of bolt joint, the longitudinal cracks appeared on the upper and lower surfaces between 100 and 110 lb-ft of the clamping torque and then propagated suddenly through the thickness and longitudinally. Figure 4-2 shows the effect of the crack (at 100 lb-ft of clamping torque) on the strains along fibers (G1) and transverse to them (G2), obtained from strain gages installed at the mentioned directions (refer to Figure 2-16). As it is illustrated in this figure, the strain transverse to the fibers dropped abruptly due to failure while the axial strain was not affected significantly. The point of failure is shown in Figure 4-2.

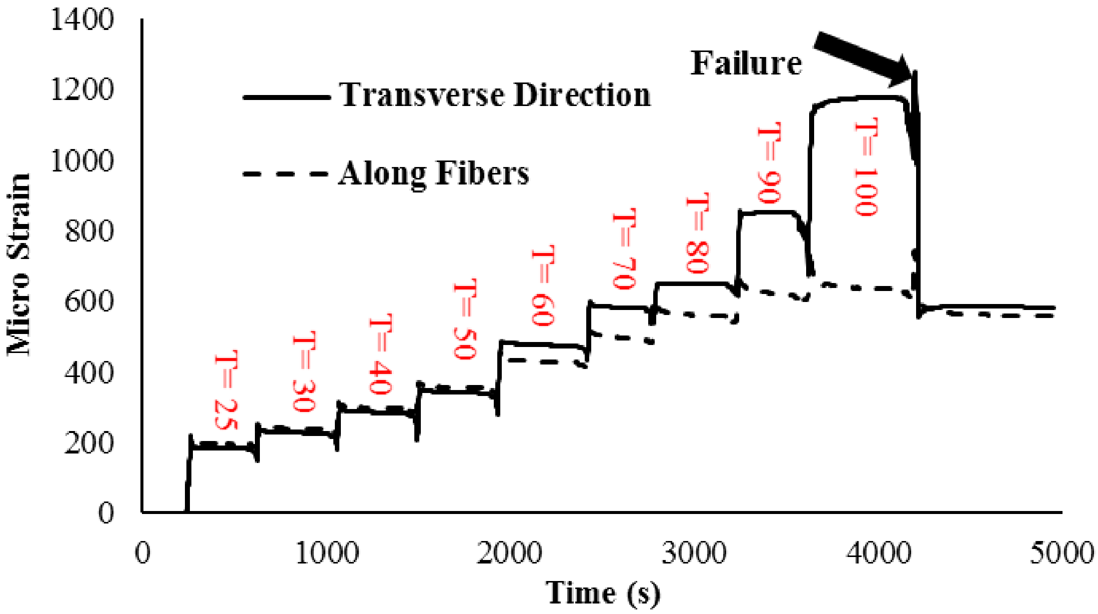

Figure 4-2: Strain along fibers and in transverse direction (The clamping torque is indicated in lb-ft)

Figure 4-3 shows the crack positions on the top surface. The visual observation of the sample revealed that the crack initiated at the vicinity of the washer outer edge and propagated both in axial direction and along the thickness of the plate. Since in this model, the top and bottom surfaces both encounter the same loading and boundary conditions, the same cracks appeared on both surfaces. Figure 4-4 shows the position of the cracks beneath the washer. In this figure, the dotted line represents the location of the outer edge of the washer and the solid line is the position of the bolt head outer diameter.

The area of the washer can be segmented into two regions. The inner region keeps the contact with the plate because of the contact force of the bolt head from upper side. This region includes almost 80% of the washer total area. On the other hand, the outer region does not experience the pressure of the bolt head on the upper surface. It seems that the outer region of the washer loses the full contact with the plate beneath that. It can be seen in the figure that the cracks were positioned at the edge of the contacted area. Visual observations after experiment, showed that the washer underwent a high conical deformation. All the mentioned evidences support the hypothesis that the loss of contact between the washer and the plate controls the position of the crack. Figure 4-5 illustrates the pattern of crack development through the thickness.

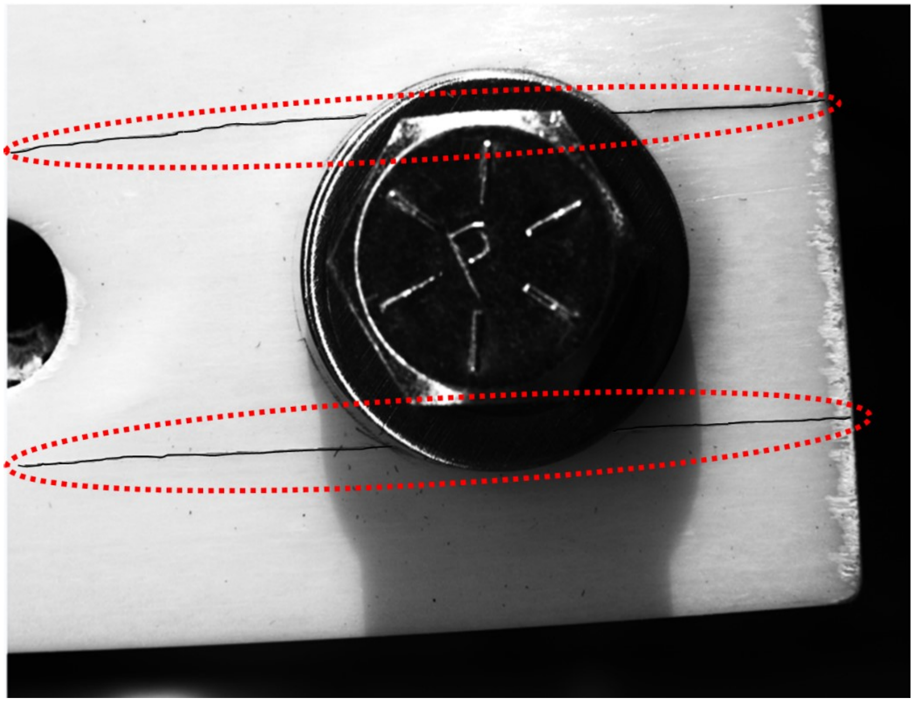

Figure 4-3: Crack positions on the top surface

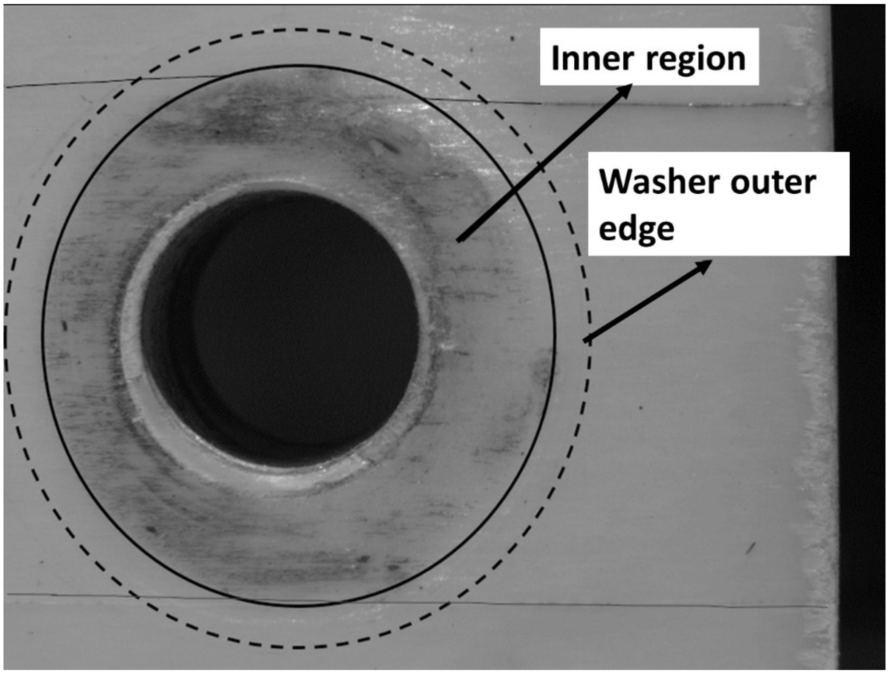

Figure 4-4: Crack position after removing washer

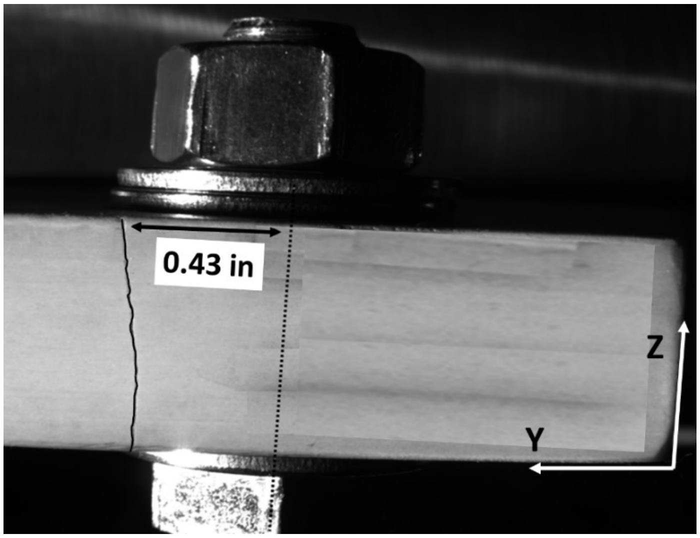

Figure 4-5: Crack development through the thickness

The progressive damage simulation was performed on the finite element model of the bolt joint. The material degradation percentage was considered as 85%. The analysis started with the pretension force of 11.1 klbs (corresponding to clamping torque of 90 lb-ft) at which no failed elements observed during simulation. The pretension force was increased with the steps of 615.4 lbs (5 lb-ft of clamping torque). The very first failed elements appeared around the outer edge of the washer and the edge of the hole at the pretension force of 12.30 klbs. Figure 4-6 shows the first failed element positions. Based on the experiments done on the relation between clamping torque and the pretension force (refer to Equation.1), 12.305 klbs of pretension force corresponds to 100 lb-ft of clamping torque. The position of the failure initiation obtained from the failure simulation correlates well with the position of the crack observed during the experiment.

It is noticeable that during experiment, the crack appeared suddenly at 100 lb-ft of the clamping torque. It seems that right after crack initiation, the complete propagation occurred.

In other words, the sample experienced crack initiation and propagation simultaneously. Therefore, the crack did not propagate gradually but it happened suddenly at one moment. A closer observation of the results obtained from failure analysis showed that the failure mode of all failed elements was mode 7 (refer to Table 4-1) and the elements failed due to the compressive stress induced by the washer contact. The failed area around the hole edge can propagate very fast in a very short distance toward the free edge of the hole and release the crack energy. Therefore, no observable cracks were found at this area during experiment.

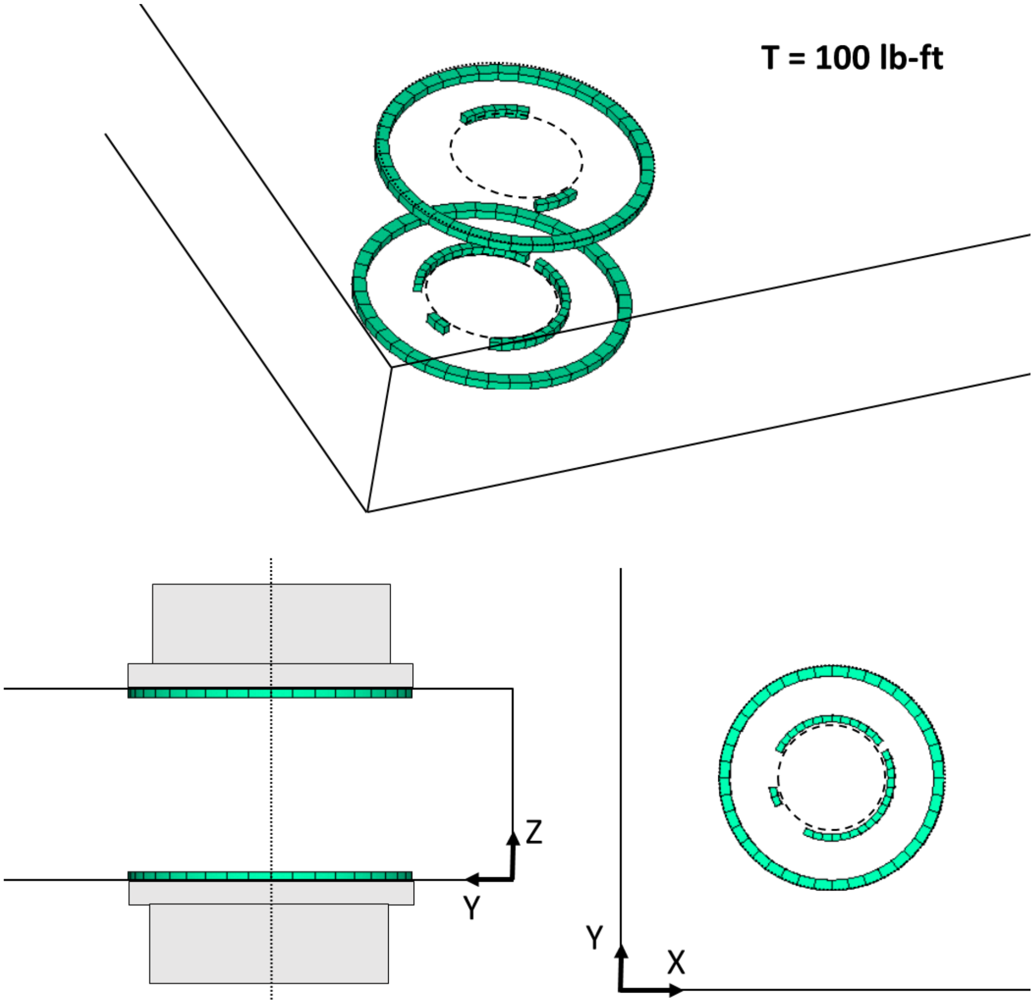

Figure 4-6: The position of failure initiation

The elements positioned at the outer edge of the washer encountered almost the same compression stress in Z direction. As shown in Figure 4-3, the cracks propagated parallel to the X axis (parallel to the fibers) rather than perpendicular to the fibers at this location. To elaborate this phenomenon, the deformation of the plate at the edge of the washer is represented in Figure 4-7. As it is obvious from this figure, the plate material intends more to tilt upward by approaching to the outer edge of the washer. A closer look at the failed elements revealed that the normal stress (S_{zz}) is the dominant stress with a greatest contribution to failure. The distribution of S_{zz} in radial direction is illustrated in Figure 4-8. Figure 4-8 shows that at a radial distance of less than 0.05” to the washer outer edge, the normal stress (S_{zz}) started to change from high compression to tension. This transition in stress distribution causes the failure. Although mode 7 is called delamination in compression in Hashin criterion (refer to Table 4-1), the type of failure happened in this loading condition cannot be associated with any of three types of defined delamination.

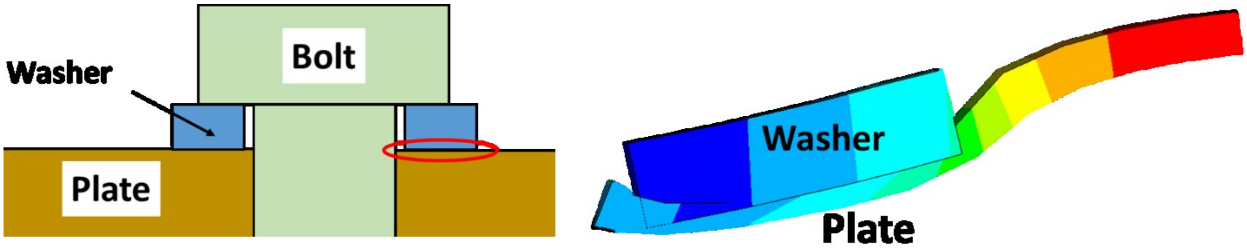

Figure 4-7: Deformation of the plate at the washer edges.

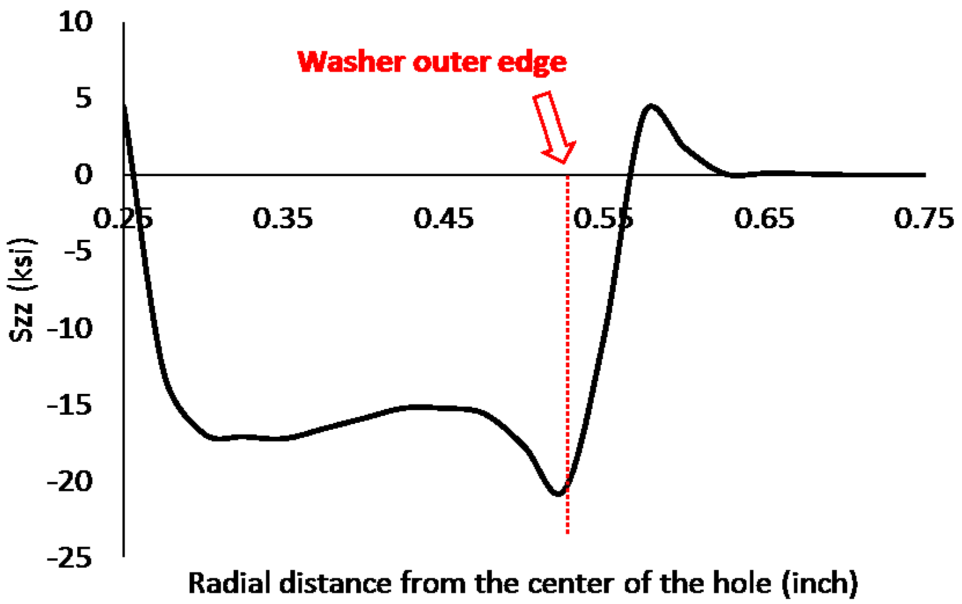

Figure 4-8: Interlaminar normal stress distribution in radial direction

As it is mentioned before and shown in Figure 4-3 to Figure 4-5, the failure propagated parallel to X axis which the direction of the fibers in the unidirectional specimen. Figure 4-9 compares the propagation of the crack parallel to the fibers and perpendicular to them. If the crack intends to grow parallel to the Y axis (perpendicular to the fibers) it will face the fibers along the thickness, so fiber axial strength will contribute in the resistance of the material against the crack propagation. The unidirectional layup sequence of the plate makes more resistance against the crack propagation parallel to the Y axis (perpendicular to the fibers) since the fibers will have some contribution against the separating forces. In the other hand, when the crack propagates parallel to the fibers (parallel to the X axis), it may find its way along the thickness by passing through the spaces between fibers and it is not necessary to cut the fibers along their length. Therefore, only matrix will resist against the separating forces. It is clear that the second scenario produces less resistance against the propagation of the failure.

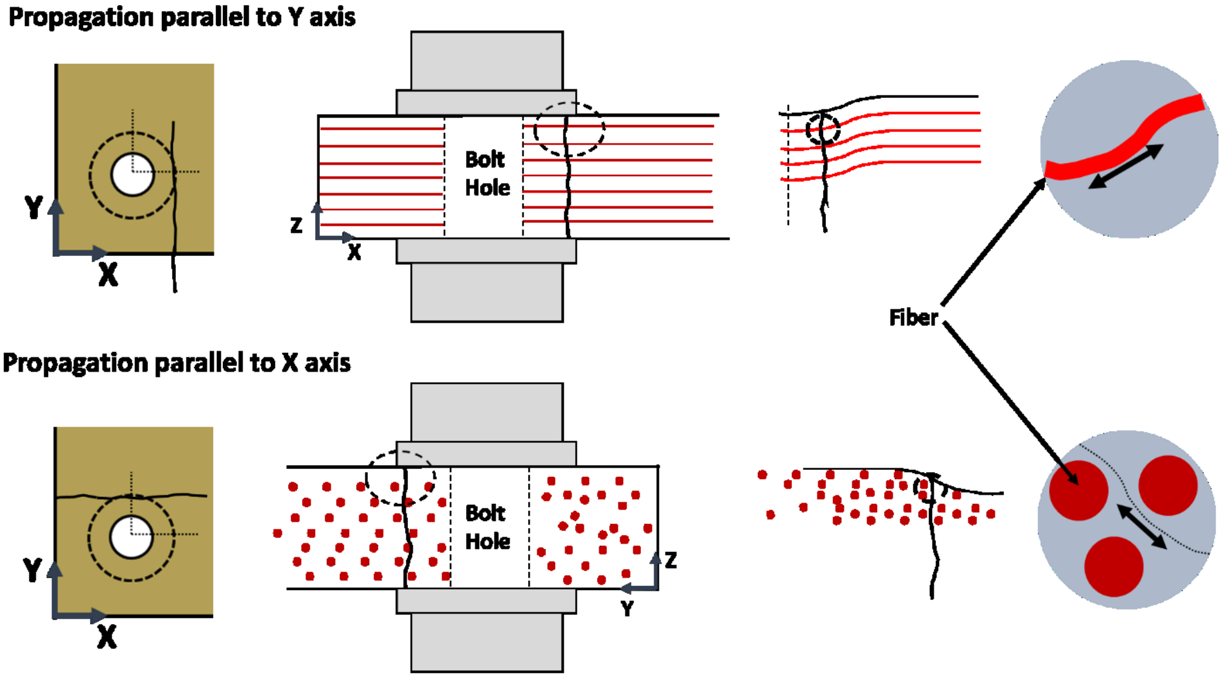

Figure 4-9: Crack propagation comparison

As a conclusion, the failure model can predict the crack position and failure clamping torque for the laminate subjected to the clamping force of bolt joint. Since the crack initiation and propagation happened at the same time during experiment, once the failed elements appeared in the analysis, that clamping torque was considered as the final failure torque of the laminate. It is noticeable that the failure model could not predict the sudden propagation of the crack after the initiation. The unidirectional layup sequence of the laminate, the position of the first failed elements, and the interlaminar normal stress distribution interpret the initiation and propagation of the crack observed during experiment.

4.3 Failure analysis - Flexural beam

The procedure to test the failure of the flexural beam was as described in chapter 3. The only difference is that the specimen was loaded until the final failure occurred. During the experiments, the final failure of the sample was defined as the point at which the axial force of the actuator dropped more than 50%. The experiments were performed on both clamped-clamped and cantilever configurations for unidirectional and cross-ply samples. All investigations were done on a plate consist of 80 layers of the Glass/Epoxy unless otherwise specified. The material properties of the Glass/Epoxy were defined as Table 2-2. The actuator was elongated with the rate of 5 mm/min up to the final failure.

4.3.1 Unidirectional sample

From the experimental tests done on several unidirectional samples, it is found that the final failure of the plate happens when the crack reaches the lateral sides of the plate. At this specific moment, a significant drop in the actuator force was observed. In addition, the DIC images showed sudden crack appearance on the side surface of the plate when actuator load significantly dropped. Figure 4-10 shows the DIC images captured right before and after final failure for both study cases. The area represented in Figure 4-10 is located under the front row bolt joints. It can be said that the plate will fail right after the crack appearance on the side surface. In other words, when the crack reaches the side surface it will propagate abruptly and cause the final failure. During the finite element failure simulation, the final failure of the sample was defined based on the crack propagation towards the side surfaces of the plate.

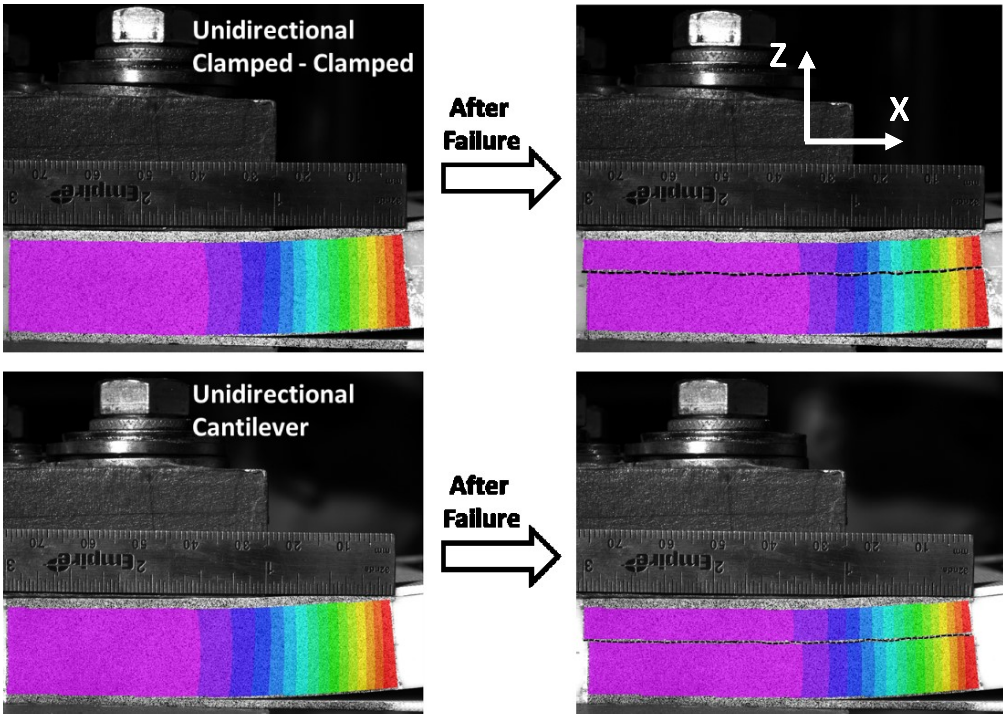

Figure 4-10: Final failure occurrence in unidirectional plates - DIC

Based on the on-site observation during the test, the cracks were heard in three steps in both clamped-clamped and cantilever configurations. For clamped-clamped model the cracks were heard first at the actuator displacement of 22 mm which was a small sound, then a medium one at 27.4 mm and a loud sound at 30.8 mm of actuator displacement. The final failure was reported at approximately 43 mm of actuator displacement. While the cracks of unidirectional cantilever model were heard at 26, 28.2 and 29.5 mm of actuator displacement and the final failure occurred at 46 mm. The actuator force at which clamped-clamped model failed was recorded as 14068 N while for cantilever the recorded force was 13736 N. As it can be seen in Figure 4-10 the cracks were located between 1.2 to 2 mm above the mid plane of the thickness.

Since the failure test data recorded for cantilever and clamped-clamped models were very close, to reduce the complexity of the failure simulation the cantilever model was selected for this purpose. To reduce the running time of the failure analysis of the flexural beam model, it was decided to decrease mesh density of the plate. Hence, for the premier analysis the number of the element across the thickness of the plate reduced to 10 from 20, which means each element was associated with a layup section consisting of 8 layers. In addition, it was observed that the critical area from the point of stresses is the clamped area at the fixed end, for this reason the mesh pattern at the regions outside the clamped area were reconfigured with coarser density.

Beside the mesh density, two other parameters should be considered when progress damage modeling is performed. First, the load increment and second, the material degradation percentage. Considering a very large load increment will reduce the opportunity of the elements to fail. As it was described before, at each load step whole model will be checked to find the failed elements then the material properties of these elements will be reduced to create a new model. Since the new model has lower strength comparing to the previous one, it will fail easier at higher load levels. By applying a large load increment, the number of load steps until final failure will be reduced. Consequently, the elements of the plate will have lower chance to be degraded at the load levels before the final failure. In contrast, very small load increment will increase the number of load steps and obviously the running time of the model to reach the final failure.

Different scenarios can be defined regarding the material degradation for the failed elements. It is possible to degrade the material properties completely or partially. In this model, the degradation percentage is being defined by the designer. Apparently, the degradation percentage can vary from material to material, in different loading conditions and based on the mode and severity of the failure. Here in this model, a single degradation percentage was defined and applied on certain material properties according to the mode of failure of the element (refer to Failure Modeling in this chapter).

Another aspect which should be included in this failure analysis, is the nonlinear large deformation analysis. As it was found during the experiments, the final failure of the plate happened around 45 mm of the actuator displacement, hence it was supposed to apply such a large displacement to the loading end of the plate. Considering the plate thickness (0.75 inch or 18.3 mm), this displacement would be a large deformation for the specimen. The linear large small deformation analysis which were performed for model validation where plate was subjected to maximum of 10 mm of deflection, was replaced by nonlinear large deformation analysis. This additional solving feature will increase the running time of each load step, but it would be mandatory for an accurate solution.

For the first attempt, the load increment was kept as 4 mm and three different degradation percentages were tested. In these analysis, the plate was loaded upward between 10 to 50 mm with the load step of 4 mm. Three different material degradation percentages were selected as 85%, 90% and 100%.

Table 4-2 compares the results obtained from different scenarios selected for failure analysis. It is noticeable that the final failure was defined as the deflection at which the failed elements reach the side surfaces. As indicated in Table 4-2, for the degradation factor of 100%, the final failure did not occur since the simulation could not converge to a solution for the deflection of 38 mm or higher. It can be concluded that killing the failed element with 4 mm of load increment is not an appropriate scenario to simulate accurately the failure behavior of the plate.

Table 4-2: Scenarios for cantilever unidirectional failure analysis

Scenario	Degradation %	Load Increment	Final Failure
1	85	4 mm	46 – 50 mm
2	90	4 mm	46 – 50 mm
3	100	4 mm	-
4	85	2 mm	44 – 46 mm
5	85	1 mm	44 – 45 mm

To elaborate the effect of degradation factor, Figure 4-11 and Figure 4-12 compare the failed region obtained from scenario 1 and 2 (refer to Table 4-2). As it was expected, a higher degradation factor led to a larger failed region in the sample. The crack on the side surface appeared around the mid plane of the thickness which matches well with the location of the crack obtained from experiments. Comparing the results of the simulation with the experiment showed that the degradation of 85 to 90 % provides a more similar failure estimation comparing with the experiment.

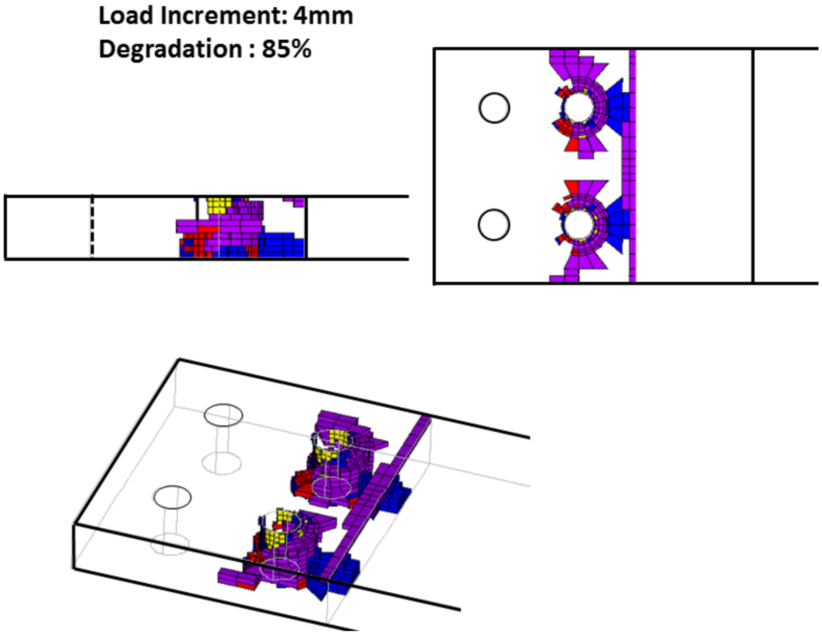

Figure 4-11: Failure propagation in unidirectional cantilever – Scenario 1 (4 mm - 85%)

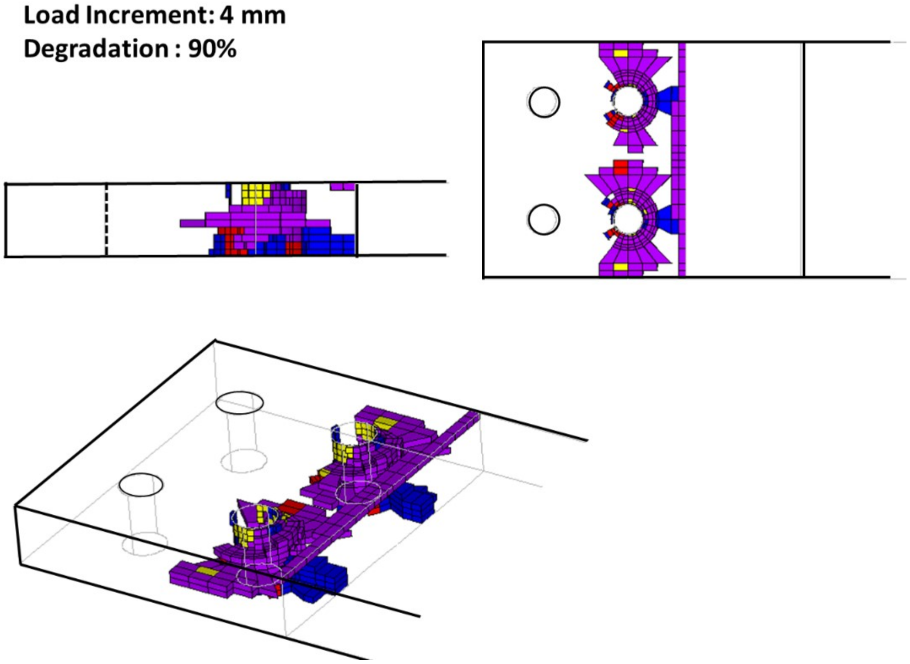

Figure 4-12: Failure propagation in unidirectional cantilever – Scenario 2 (4 mm - 90%)

To investigate the effect of the loading increment on the failure propagation, a simulation was performed by using the degradation factor of 85% and load increment of 2 mm (refer to scenario 4 at Table 4-2. Results showed that the final failure happened between 44 to 46 mm. As the meshing pattern, outside of the clamped region is very coarse, the failure analysis results at this region is not trustable using this meshing pattern. The position of the crack along thickness is at the upper side of the midplane. Comparing the number of failed elements between scenarios number 1 and 4 of Table 4-2, showed that with the increment of 2 mm, the failed region was greater than the 4 mm of load increment. Finally, the load increment was reduced to 1 mm and the degradation percentage was selected to be 85% (refer to scenario 5 at Table 4-2). The results showed that the final failure occurred between 44 to 45 mm of displacement. Figure 4-13 illustrates the results obtained for final failure of the plate underwent the failure analysis according to scenario 5. Reducing the loading increment from 2 mm to 1 mm increased the number of failed elements by 70%. In the following section the results obtained from scenario 5 are compared with the experiment.

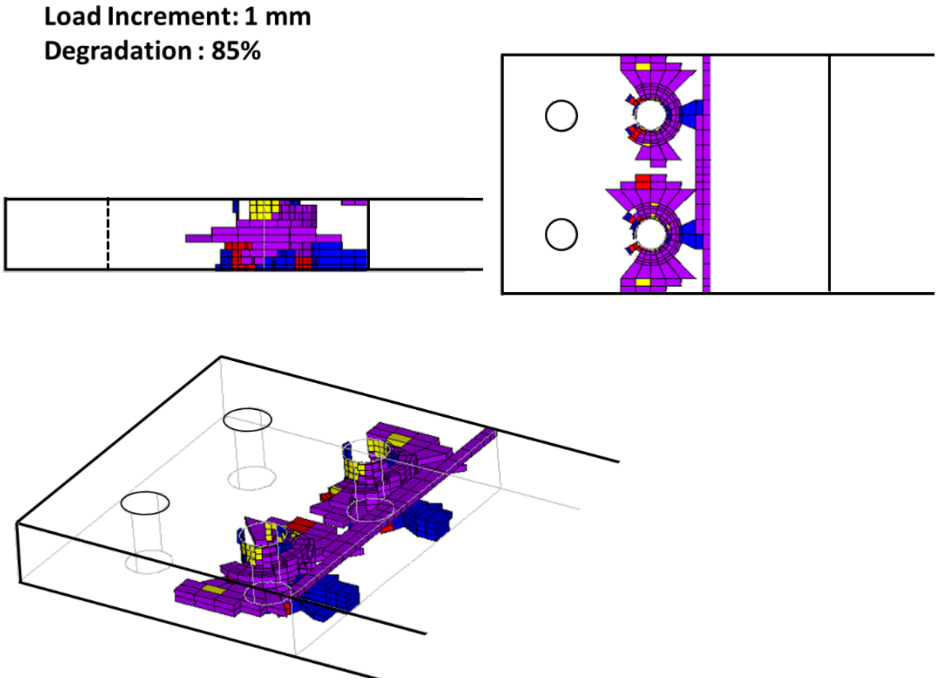

Figure 4-13: Failure propagation in unidirectional cantilever – Scenario 5 (1 mm - 85%)

Since the elongation of the actuator could be different from the upward displacement of the load line which is defined for cantilever model (refer to Figure 3-10), it was desired to find the load line displacement from the experiments rather than the actuator elongation (refer to Figure 3-10 for loading line definition). To find the displacement of the loading line in cantilever model the results obtained from digital image correlation on the top surface was utilized. Since a three-dimensional digital image correlation analysis was performed on the top surface of the plate, the out of plane displacement of the top surface (U_Z) was available. In addition, the DIC system captured photos at the time interval of one second which provided a photo at a moment very close the final failure. Figure 4-14 shows the top surface out of plane deformation of the unidirectional cantilever model right before the final failure which corresponds to 46 mm of the actuator elongation.

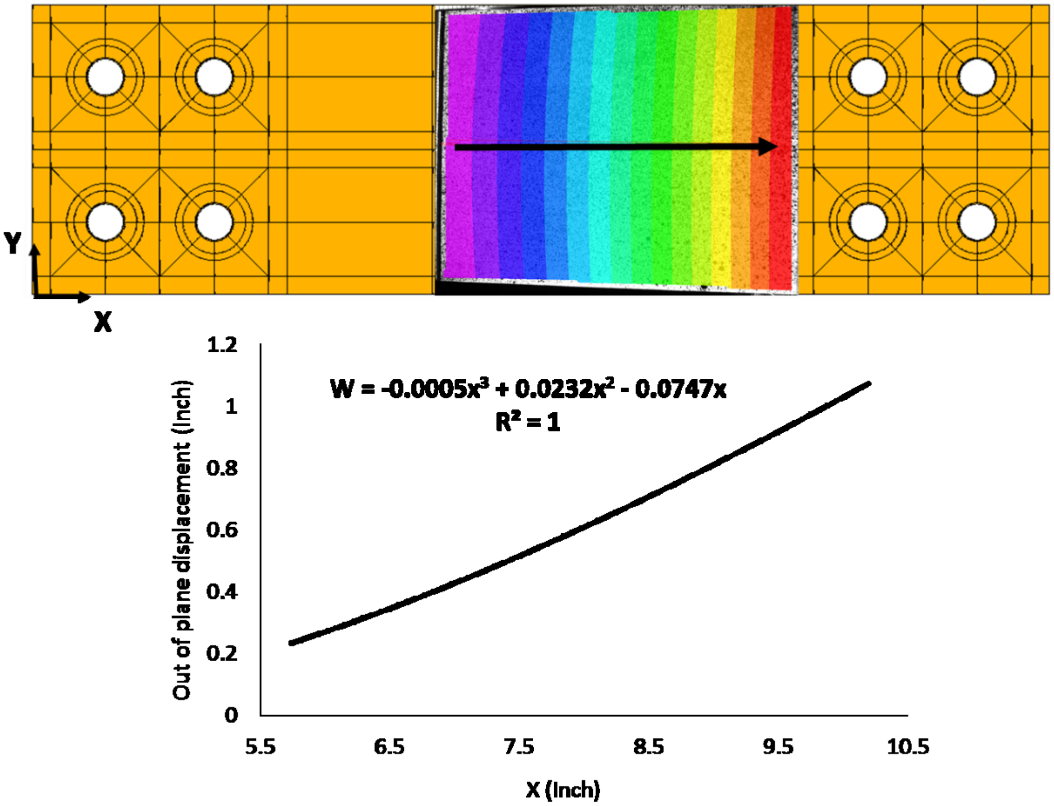

Figure 4-14: Unidirectional cantilever out of plane displacement at 46 mm of actuator elongation

As it is indicated in Figure 4-14, a line has been fitted to the curve obtained from DIC data on the top surface. To find the upward displacement of the load line of the cantilever beam the curve was extrapolated to the position of $x = 12.25$ inch (which corresponds to the load line position on the cantilever sample). Based on the equation illustrated in Figure 4-14, the displacement of the load line of the cantilever model at the 46 mm of actuator elongation would be 1.69 inch or 43 mm. Considering the results of the finite element failure analysis (scenario 5) which predicted the final failure at the load line displacement of 44 to 45 mm, it can be said that the model was able to predict both the location of the crack and the failure displacement level with a good accuracy.

To investigate the effect of the mesh density on the failure prediction, a finer mesh pattern was created. The number of the elements along the thickness was changed from 10 to 20 elements and the density of the mesh was increased specially around the joints. The new mesh pattern increased the number of the plate elements from 10040 to 29920 elements which is almost three times more. The cantilever unidirectional plate with the finer mesh pattern was loaded between 10 to 50 mm of displacement with the increment of 4 mm and the material degradation percentage was selected as 85%.

Figure 4-15 shows the failure propagation in the model with a finer mesh. Comparing this figure with Figure 4-11, revealed that the creating of a finer mesh would not necessarily provide better correlation with the experiment. For the model with finer mesh the failure propagated over a smaller region considering that Figure 4-15 corresponds to 50 mm of the displacement. The model with a finer mesh predicted final failure between 46 to 50 mm of displacement. Therefore, in this model, a finer mesh did not provide results with a better correlation with the experiment. Study the effect of mesh density is not the main subject of this research, therefore results obtained above may not be applicable for all study cases. What is explained above is only applicable for this study case and cannot be generalized.

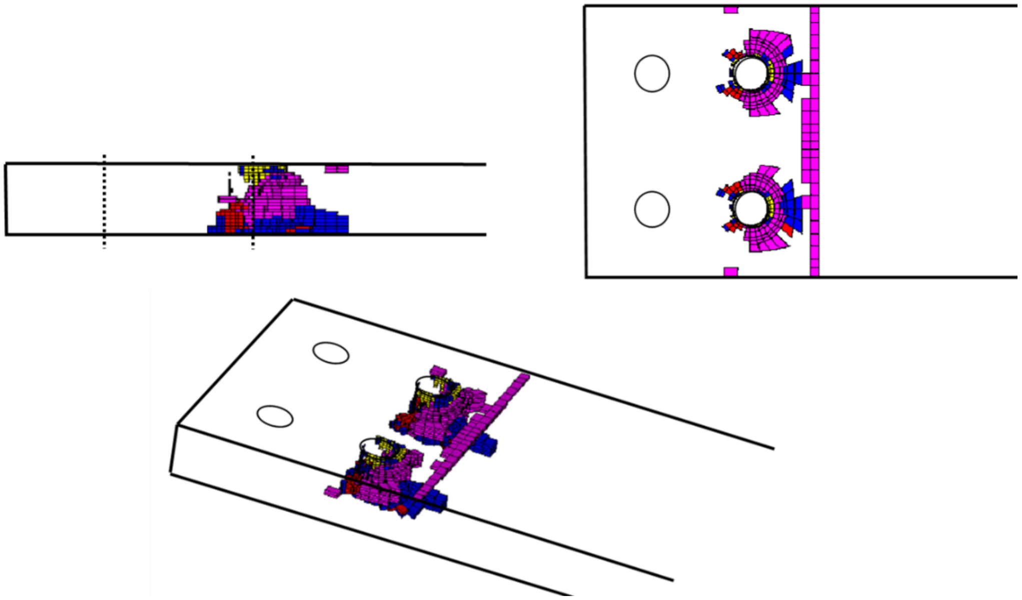

Figure 4-15: Failure propagation in unidirectional cantilever – Fine mesh (4mm – 85%)

(Compare with Figure 4-11)

The propagation of the failure inside the plate was also investigated by cutting the sample at two different sections and looking at the crack shaped during the experiment. The same sections were created in the model and the failure propagation was obtained. Figure 4-16 and Figure 4-17 show the crack shape obtained from experiments and the propagation calculated by failure model at the sections located at X = 3 inch and X = 2.25 inch respectively. As it is illustrated in these two figures the crack shape matches with failed elements configuration at these two different axial positions.

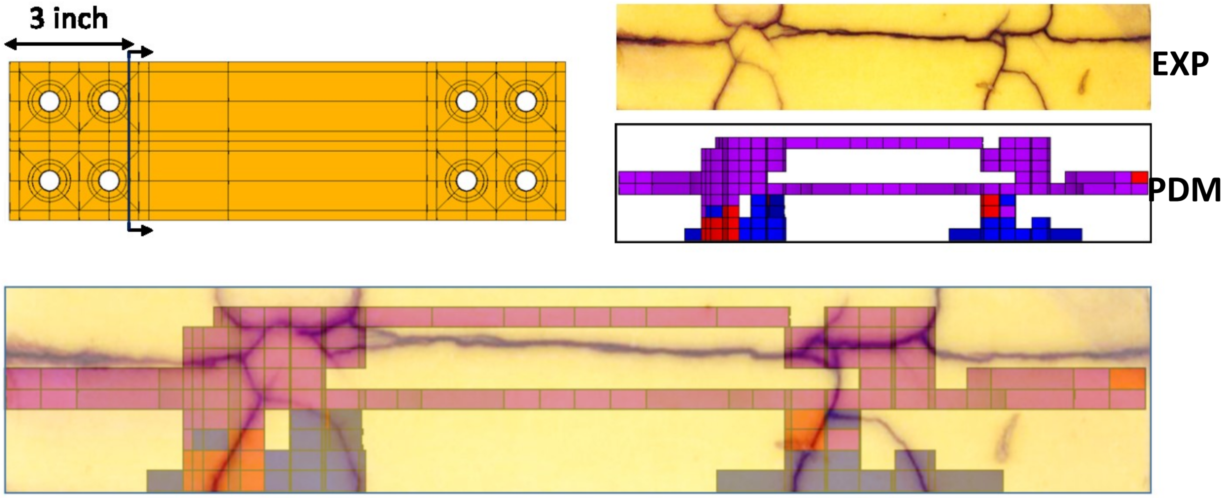

Figure 4-16: Failure propagation at X=3 inch – PDM vs Experiment

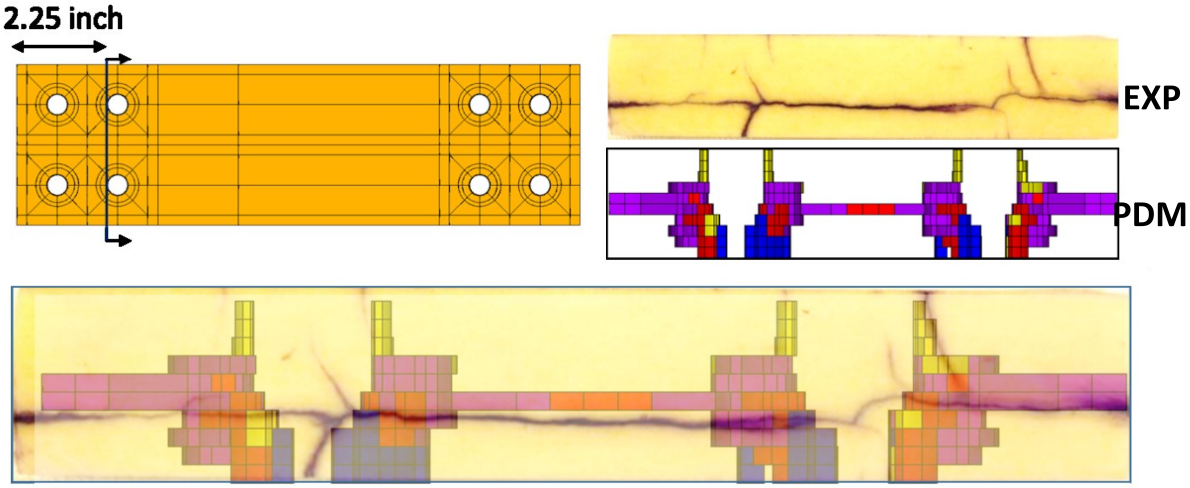

Figure 4-17: Failure propagation at X=2.25 inch – PDM vs Experiment

To summarize, the proposed model can predict failure in the unidirectional sample. The results showed that the actuator displacement at which the final failure took place during experiment corresponds very well with the displacement level at which the failed elements reached the side surfaces of the plate during the simulation. Although the model can predict the failure propagation up to the point when failure appears on the side surfaces it is not able to simulate the sudden propagation of the crack after this point. In other words, during experiment when the crack reaches the side surfaces it developed abruptly through the plate while this phenomenon could not be captured by the model.

The results of failure analysis for the unidirectional sample revealed that the first failed elements appeared at the edge of the front bolt holes at 10 mm displacement of the load line. Up to the displacement of 26 mm, the failure accumulated around the front bolt holes. At this load level, the elements positioned at the edge of the steel plate failed because of the stress concentration which exist at this position. Then these two failed areas propagated in the region between front holes and steel plate edge. At the loading level of 44 to 45 mm of displacement, the first failed elements appeared at the thickness side of the plate. The position of the failed elements across the thickness corresponds very well with the cracks observed during experiment. Figure 4-18 illustrates the initiation and propagation of the failure inside the unidirectional cantilever sample.

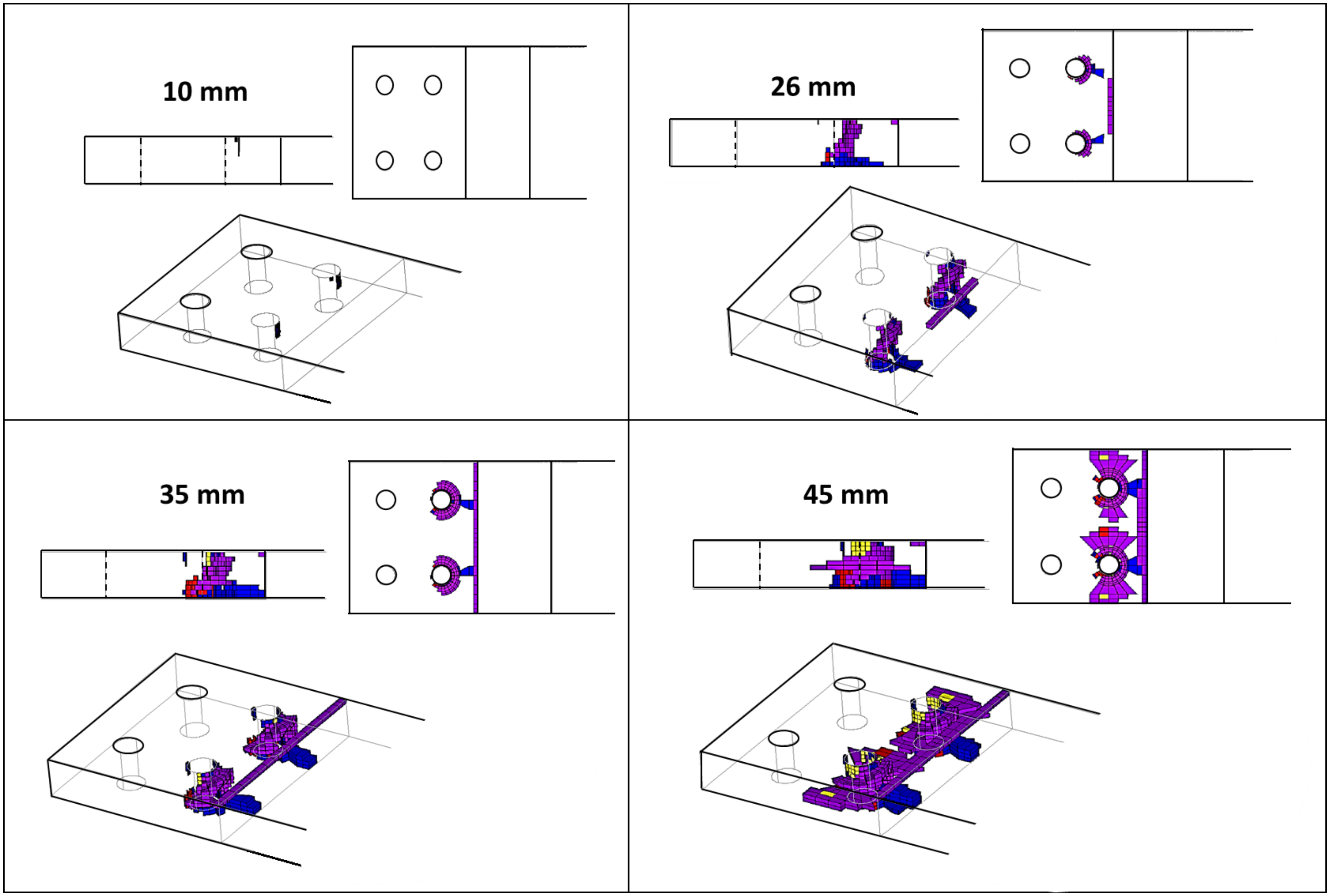

Figure 4-18: Failure propagation inside the unidirectional cantilever sample

(Numbers indicate loading end displacement)

It has to be notified that only the elements located under the clamped area of the fixed end of the plate were considered for failure analysis (corresponds to 25% of the whole plate volume) to reduce the running time of the process. A closer investigation of the results obtained from unidirectional cantilever failure analysis showed that at 45 mm of the displacement level (which was defined as the final failure of the sample), 7% of the whole volume of the clamped area were failed which corresponds to the 18.5% of total elements of this region. Figure 4-19 represents the volume of the failed region due to each failure mode, for each loading level of Figure 4-18.

The delamination had the most contribution in the failure of the sample. Also, the rate of the delamination propagation changed considerably as the process approached the final failure (45 mm of displacement). In addition, according to Figure 4-19 the fiber failure was negligible up to 35 mm of displacement while it developed for higher steps of the loading. Finally, the rate of failure propagation due to matrix failure was almost constant. Figure 4-20 shows the area percentage of failure due to each of the failure modes for different displacement levels. As it is obvious from this chart, delamination or in a better word failure in Z direction had the most significant contribution in the final failure of the whole plate. For example, the total region failed due to other failure modes is almost equal to the half of the region failed due to delamination (failure in Z direction). It is illustrated in Figure 4-20 that for the last steps before the final failure, the contribution of the matrix failure decreased while other failure modes took over a greater contribution to the final failure region in the plate.

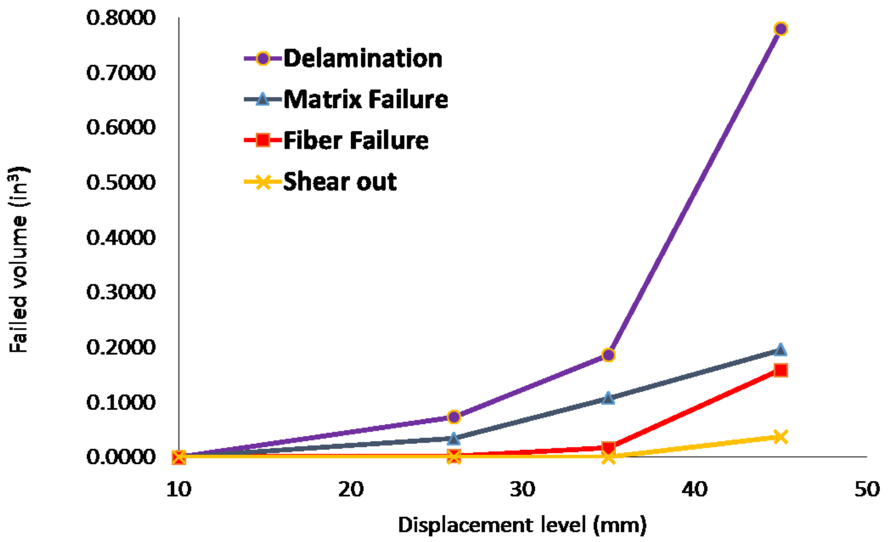

Figure 4-19: The modes of the failure for the unidirectional cantilever sample

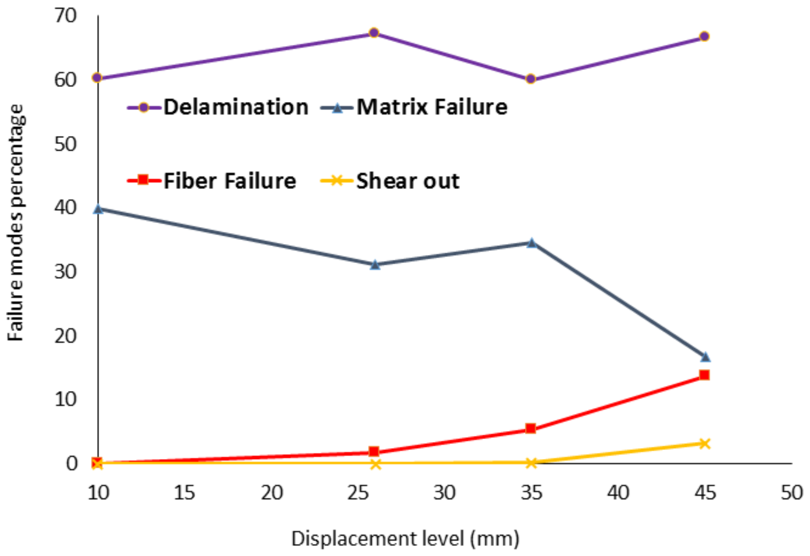

Figure 4-20: Percentage of each failure modes at different displacement levels

As it was described in Table 4-1, the stresses which contribute in mode 6 and mode 7 of failure (delamination) are the interlaminar normal stress, σ_Z and interlaminar shear stresses σ_{XZ} and σ_{YZ}. It was desired to find out which of the above stresses has the most significant effect on the failure of the elements to distinguish the mode of delamination. Therefore, the stresses were found for the failed elements that appeared on the side surface. They were plugged in to equation for delamination according to Table 4-1. It is shown in Figure 4-21 that the interlaminar shear stress, σ_{XZ}, has the dominant effect which represents the second mode of delamination. The same delamination mode was observed when the crack position obtained from DIC was investigated in more detail. Figure 4-22 shows the crack position on the side surface obtained from experiment. It is obvious that the second mode of delamination occurred at this region.

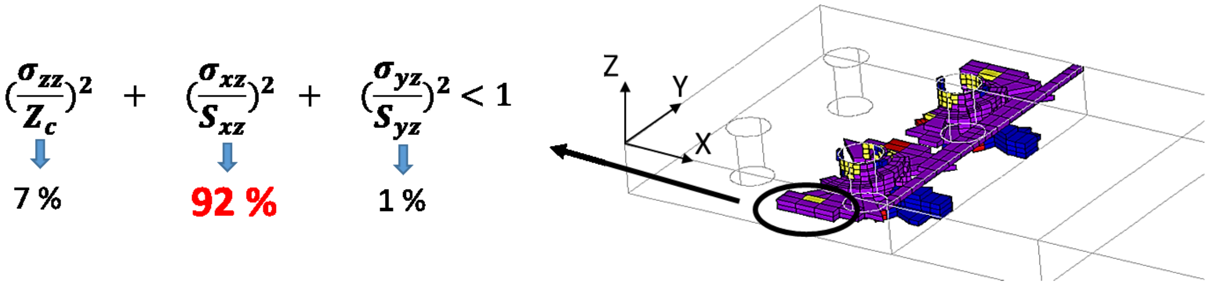

Figure 4-21: Contribution of each stress in delamination of the elements on the side surface

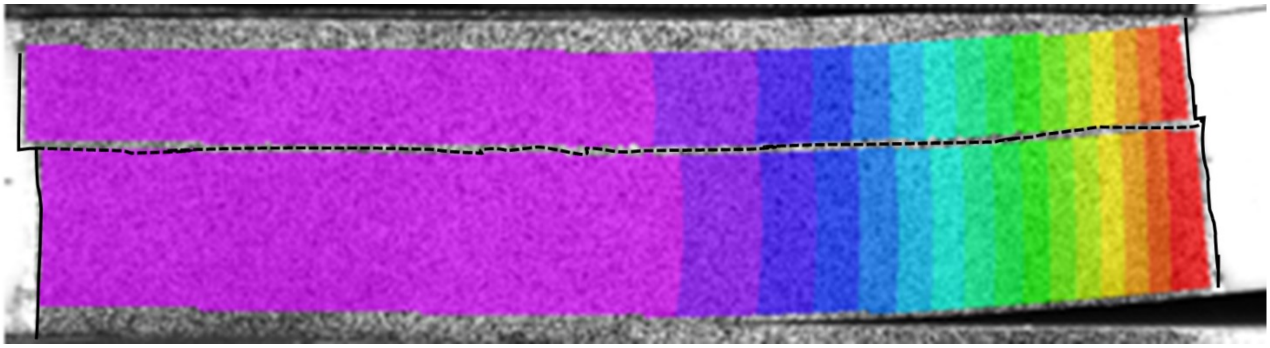

Figure 4-22: Mode 2 delamination of the sample

4.3.2 Thickness effect on failure of unidirectional sample

The failure analysis was duplicated for the plates with 20, 40, 60, and 80 number of layers. The goal of these analysis was to find out the effect of thickness on failure behavior of the cantilever unidirectional sample. To reduce the number of necessary load steps to catch the final failure (when crack reaches the side surfaces), the plates were loaded upward from the initial displacement of 10 mm with the load step of 10 mm. The end point of the analysis was selected based on the data obtained during the experimental test of each sample. To validate the model prediction, the experimental tests were also repeated for the plates with mentioned thicknesses and their data were recorded. Table 4-3 summarizes the actuator displacement obtained at the point of failure of plates with different thicknesses. The analysis of the plate with 80 layers was duplicated with the new loading step to provide the similar analysis condition for all plates with different thicknesses.

Table 4-3: Final failure load level - Experiments

Plate	Final failure - actuator displacement
20 layers	No final failure up to 75 mm
40 layers	No final failure up to 75 mm
60 layers	57 mm
80 layers	45 mm

As it can be seen in Table 4-3, no failure occurred up to 75 mm of actuator displacement for the 20-layer and 40-layer samples. The test could not be continued for more than 75 mm of displacement because of the test setup limitations. The test setup was not designed to provide more than 75 mm of actuator displacement. During the failure analysis of the 20-layer plate, no failed element appeared up to 100 mm of loading line displacement, therefore the analysis was not proceeded after this point. For 40-layer plate, the first failed elements appeared between 40 to 50 mm of displacement. For the plate with 60 unidirectional layers, the failure initiated between 20 to 30 mm of displacement. Finally, for the 80-layer plate the first failed element appeared between 10 to 20 mm of displacement during analysis. To compare the intensity of the failure initiation a parameter called Failure Volume Index (FVI) was defined according to Equation 2. Figure 4-23 shows the failure initiation region for different plates and the corresponding FVI. As it is clear in this figure, failure starts faster and over a larger zone in thicker plates. For all the laminates except the thinnest one (20 layer plate), the failure started at the edge of the front lane bolt joints.

$$Failed\ volume\ index = \frac{Volume\ of\ the\ failed\ region}{Plate\ volume} \times 10^{3} \qquad \text{Equation 2}$$

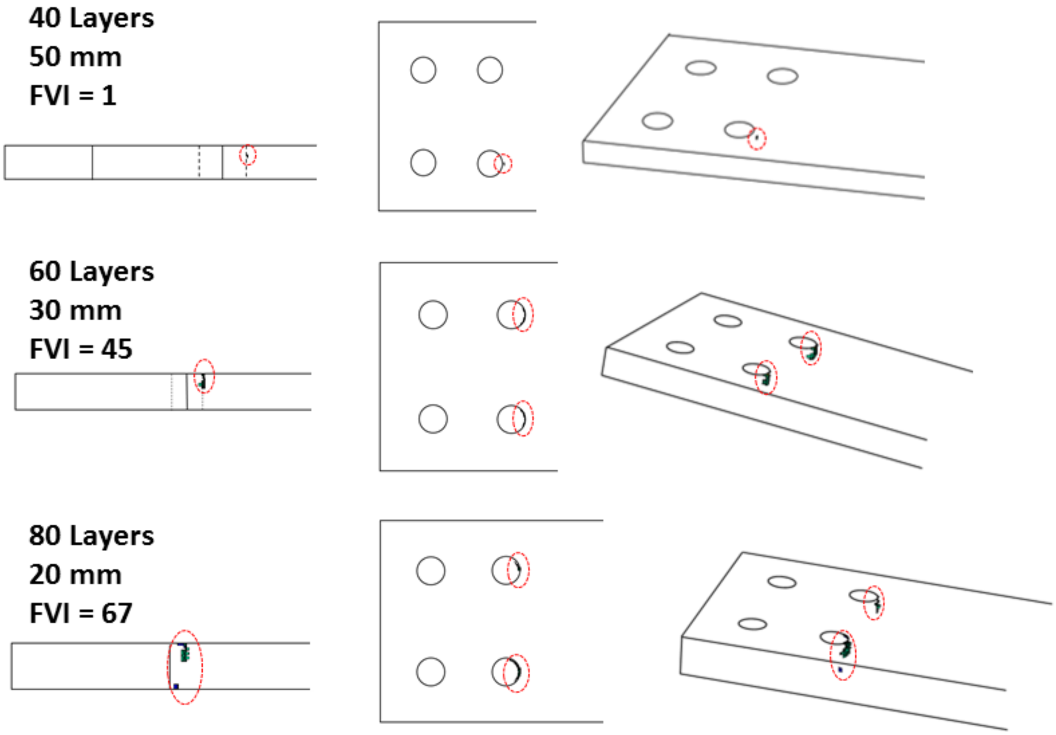

Figure 4-23: Failure initiation for plates with different thicknesses

Since the load increment was selected too large (10 mm) during the analysis, the final failure obtained did not correlate well with the experiment for 60 and 80 layer plates. For comparison of the propagation of the failure between different plates, the state of the elements of each of the plates was extracted from analysis. As mentioned before there were no failed elements for 20-layer plate. Figure 4-24 illustrates the failure volume index (FVI) as it was defined in Equation 2. The FVI is shown for different plates from the initiation point to the displacements which corresponds to the maximum deflection applied during experiment.

As it is indicated in Figure 4-24, the failure initiation happens at lower deflection levels for thicker plates. Also, the thicker the plate is, the final failure happens earlier. There is a considerable difference between plates with 40 and 60 layers in terms of the rate of failure propagation while this difference is not that significant between 60 and 80-layer plates. At the same deflection level of 50 mm, the failure propagates over a significantly larger zone in 80-layer plate comparing to the other thinner ones.

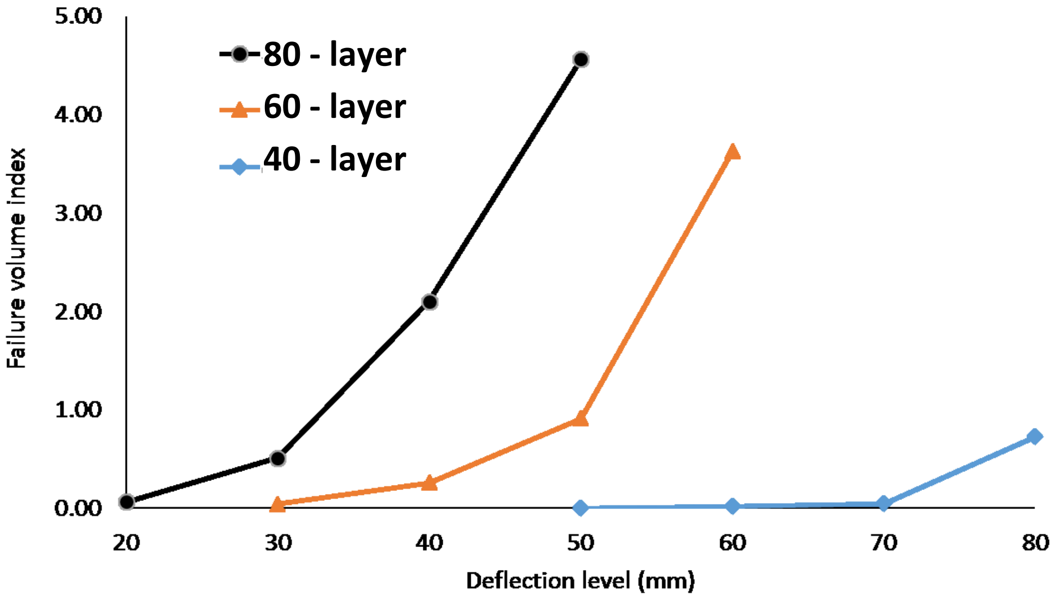

Figure 4-24: Failure volume index from initiation to maximum deflection

4.3.3 Cross ply sample

For further investigation of the failure model feasibility for the laminates with the layer sequences other than unidirectional, a cross ply sample consisting of 80 layers was manufactured and tested up to the failure. Therefore, the layup sequence of the new sample was $[0/90]_{20S}$. Based on the data reported from the experimental investigation the cross-ply cantilever samples failed between 51 to 53 mm of the actuator displacement for three different trials. For comparison with analysis the experimental failure point was considered as 52 mm of actuator displacement. As to be expected, the cross-ply samples had the failure delamination completely contained between the middle two 90-degree plies. All three cross-ply samples showed change of delamination plane at about X=3 inches, which corresponds to the location just in front of the most highly stressed bolt holes. Figure 4-25 shows the DIC images before and right after the final failure of the cross-ply sample. The change of delamination plane at the axial position corresponding to the front lane bolt joints is being highlighted in Figure 4-25 .

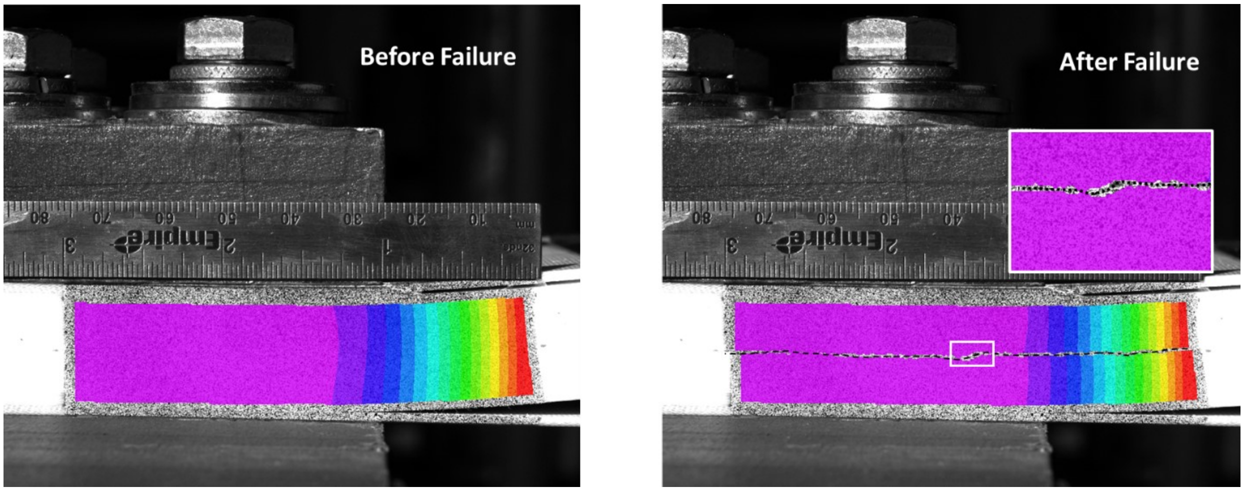

Figure 4-25: Crack position on the side surface of the cross-ply sample

The finite element model had to be modified for simulation of the failure of the cross-ply laminate. As it was described in section Cross ply cantilever, the elements of the half top and bottom parts of the sample were associated with different sections to model the symmetric layup sequence. One of the challenges which raised during the failure analysis of the cross-ply sample was the material strength which has to be defined for failure analysis.

To elaborate the problem, two layered solid elements consisting of 2 layers, with unidirectional and cross ply sequences are shown in Figure 4-26. As it was described in the

Failure Modeling section, to find the failed elements the stress results obtained for each element were compared with the material strength of that element regarding the equation of the Hashin failure criterion (refer to Table 4-1). In other words, the failure code considers the element as a single block with predefined material strength in different directions instead of considering the element as a layered volume. For unidirectional laminate, each element has the same material properties as orthotropic properties of a single lamina. In contrast, for an element with two [0/90] plies (refer to Figure 4-26), the element strength in X and Y directions (in plane properties) are not equal to the lamina orthotropic material properties. Therefore, for failure analysis of the cross-ply laminate, it was required to find the material strength of the layered solid element which was used to mesh the plate.

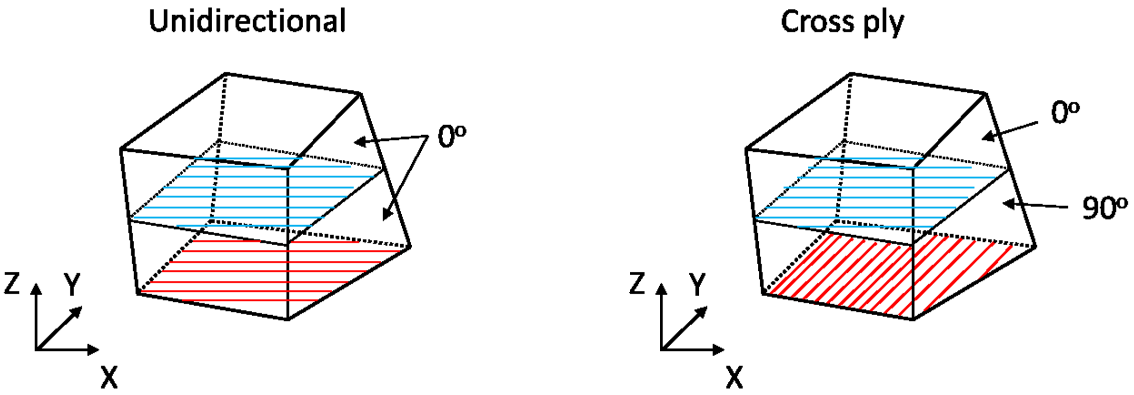

Figure 4-26: Unidirectional vs Cross ply layered solid elements

One solution to overcome the above challenge is to create as many elements as the number of layers along the thickness and associate different sections to each element. This method works theoretically but it would require a vast number of elements which it is not feasible using ordinary computers. Another solution is utilizing classical lamination theory (CLT) to find the equivalent strength of the element under different loading scenarios. Following an example of the calculation to find the strength of the $[0/90]_4$ element is reviewed. To calculate the strength of the material in other directions, the same scenario was considered.

Figure 4-27 shows a cross-ply laminate consisting of 8 layers subjected to a unit axial force. The mentioned plate represents the element which was used for cross ply laminate failure analysis. This element was analyzed using classical lamination theory and the max stress failure criterion to find the force at which the whole laminate fails. The calculated force was divided by the laminate thickness to find the failure stress. This failure stress represents the ultimate strength of the defined element. Different loading conditions were considered for calculation of the other material strength of the element block.

Table 4-4 summarizes the strengths obtained for the cross-ply element and compares them with the lamina orthotropic strength. As it was expected for cross ply laminate of $[0/90]_4$, similar strength in axial and transverse directions was obtained. Also, the in-plane shear strength obtained is equal to the unidirectional in plane shear strength. Since the zero angle layers play the key role in axial direction tensile strength, by reducing the number of zero layers to half, the tensile strength in axial direction reduced from 247.7 ksi to 108 ksi which is approximately a 50% reduction while the transverse tensile strength improved significantly.

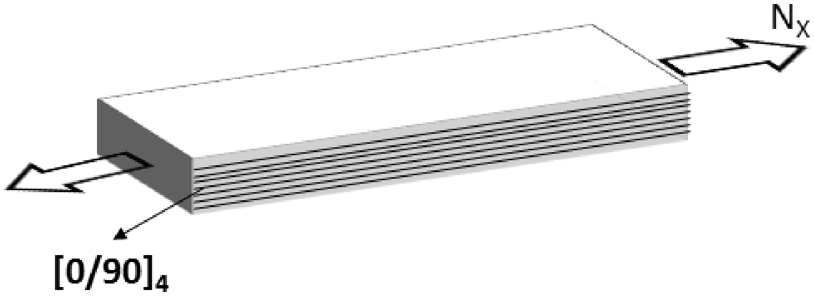

Figure 4-27: Cross ply element under a unit axial force

Table 4-4: Material strength defined for cross-ply cantilever sample

Strength Property (ksi)	Unidirectional $[0]_8$	Cross ply $[0/90]_4$
Axial Tension	247.7	108
Axial Compression	-139	-111
Transverse Tension	8.88	108
Transverse Compression	-20.14	-111
In-plane shear	11.6	11.6

The out of plane axial and compression properties of the laminate is controlled by the matrix therefore it can be assumed that they remain identical. For the sake of simplicity, it was assumed that the interlaminar strength of the cross-ply element is the average of the interlaminar shear strengths of the unidirectional element in two different planes (XZ plane and YZ plane). It should be mentioned that the cross-ply laminate has the same interlaminar shear strength for the XZ and YZ planes. Finally, the material strength of the cross-ply element block was defined in Table 4-4.

To compare the experiment data with the analysis results, it is necessary to find the relation between the actuator displacement and the displacement of the loading line on the model (located at X = 12.25 inch). Similar to unidirectional plate, this relation was found using the DIC out of plane deformation data on the top surface. Figure 4-28 illustrates the out of plane displacement (in Z axis) for cross ply cantilever sample over the area of interest on the top surface at the actuator elongation of 52 mm. Also, the displacement distribution versus X axis is shown in the graph of Figure 4-28. This relation was extrapolated to the position of the load line on the model (X = 12.25 inch) and the upward displacement of the load line at the final failure point was obtained as 1.69 inch or 43 mm.

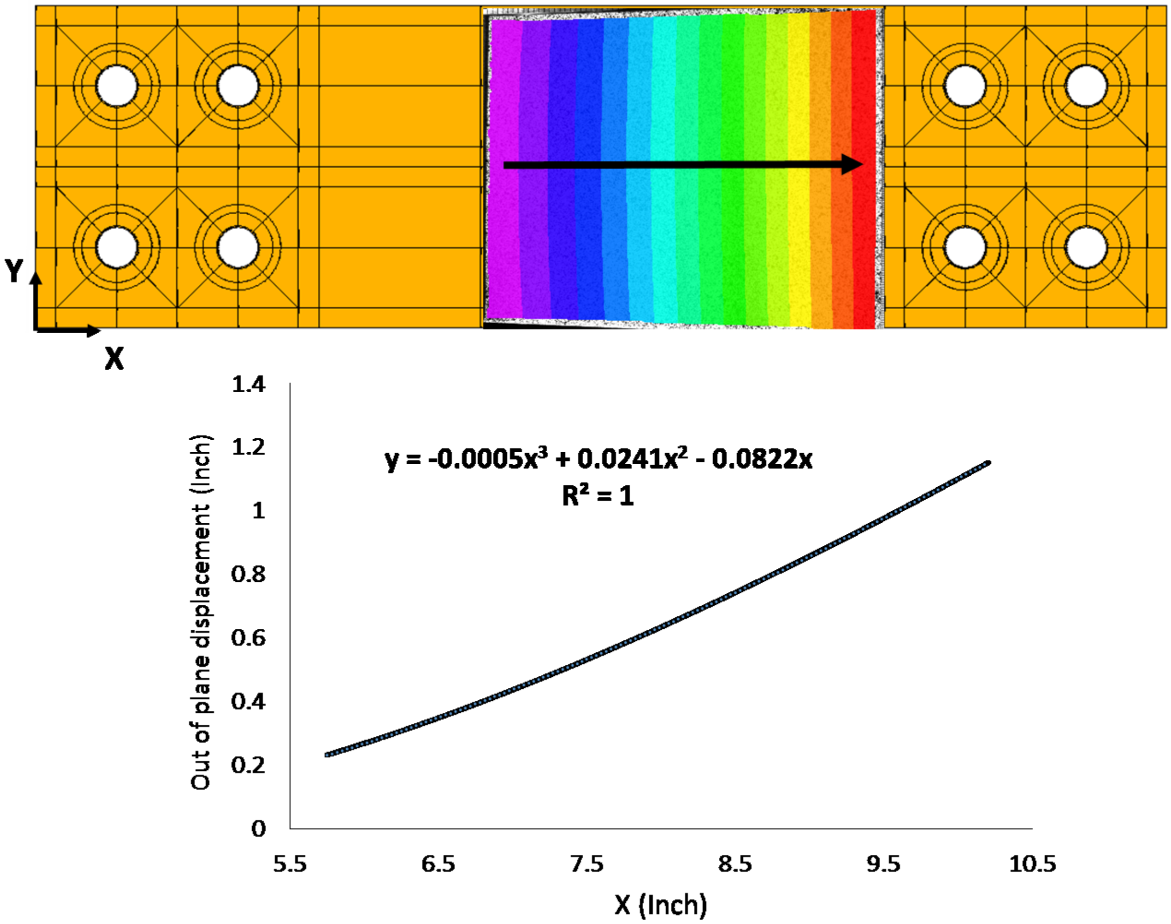

Figure 4-28: Cross ply cantilever out of plane displacement at 52 mm of actuator elongation

During the experimental test of cross-ply cantilever sample, the final failure occurred at the average actuator displacement of 52 mm. Since the plate is subjected to flexural bending, the axial strength and stiffness of the plate will control mainly the behavior of the plate. The cross-ply laminate failed at the higher displacement comparing to the unidirectional laminate. In addition, the average of the actuator force at the final failure of the unidirectional plate was 28% higher than the cross-ply laminate. This phenomenon show that the stiffness of the cross-ply laminate is less than unidirectional one which was expected because of lower number of zero-degree layers. Table 4-5 compares the final actuator displacement and force for both unidirectional and cross-ply laminates.

Table 4-5: Comparison of final failure of cantilever laminates – Unidirectional vs Cross-ply

Laminate	**Final failure actuator displacement**	**Final failure actuator force**
Unidirectional cantilever	45 mm	13.9 KN
Cross-ply cantilever	52 mm	10.8 KN

Following assumptions were considered during the failure analysis of the cross-ply laminate:

1. The material strength of the laminate element was defined as per Table 4-4.
2. The cross-ply laminate has the same interlaminar shear strength for the XZ and YZ planes which is the average of the shear strength of the unidirectional laminate in the above planes.
3. The failure modes of 1 to 4 of Hashin criterion (refer to Table 4-1) were not distinguishable for the case of the cross-ply laminate. Therefore, they were combined as the material failure in X and Y directions as per Table 4-6.
4. For the cross-ply laminate three degradation scenarios were defined (refer to Table 4-6):
    a. Material failure (in X and/or Y direction): was applied to modes 1 and 2, degrades all the material properties

   b. Fiber-Matrix shear out (In XY plane): was applied to mode 3, degrades G_{XY} and v_{XY}.
   c. Delamination (in Z direction): was applied to modes 4 and 5, degrades E_Z, G_{XZ} and G_{YZ}.
5. For the Material failure scenario of the cross-ply laminate, all the material properties of the element will be degraded in case of the failure of the element.
6. Each element can fail and be degraded only once during the whole failure analysis.

By modifying the failure analysis code considering the above assumptions, it was found that the final failure of the cross-ply cantilever laminate (defined as the point where the failure region reaches the side surface) happened at the cross ply model loading end displacement of the 40 mm. Results illustrated in Figure 4-28 and extrapolation of the top surface out of plane displacement to the position of the load line (X = 12.25 inch) showed that the load line upward displacement at the actuator elongation of 52 mm was approximately 43 mm. Therefore, the difference between analysis and experiment is about 7.5 % which represents well agreement between two approaches and shows that the model presented more conservative failure prediction.

Figure 4-29 shows the position of the crack on the side surface obtained from failure analysis. It is shown in Figure 4-25 and was mentioned before that during the experiments, the cross-ply laminates showed a change in the plane of delamination around the position of X = 3 inch. As it is indicated in Figure 4-29, it was found during analysis that the plane of the delamination changed at the position of the X= 2.9 inch. This fact shows a close agreement with the experimental observation about the position of the delamination. Also, the results showed that for the cross-ply laminate, 65% of the elements failed due to delamination, 29% due to material failure and 6% due to fiber-matrix shear out. This phenomenon correlates with the experiment in which the failure appeared mostly as the delamination.

Table 4-6: Failure modes for cross-ply laminate

Failure Mode		**Criteria**
1	Material tensile cracking	$(\frac{\sigma_{yy}}{Y_T})^2 + (\frac{\sigma_{xy}}{S_{xy}})^2 + (\frac{\sigma_{yz}}{S_{yz}})^2 \geq 1$ $(\frac{\sigma_{xx}}{X_T})^2 + (\frac{\sigma_{xy}}{S_{xy}})^2 + (\frac{\sigma_{xz}}{S_{xz}})^2 \geq 1$
2	Material compressive cracking	$(\frac{\sigma_{yy}}{Y_C})^2 + (\frac{\sigma_{xy}}{S_{xy}})^2 + (\frac{\sigma_{yz}}{S_{yz}})^2 \geq 1$ $(\frac{\sigma_{xx}}{X_C}) \geq 1$
3	Fiber-Matrix shear out	$(\frac{\sigma_{xx}}{X_C})^2 + (\frac{\sigma_{xy}}{S_{xy}})^2 + (\frac{\sigma_{xz}}{S_{xz}})^2 \geq 1$
4	Delamination tensile	$(\frac{\sigma_{zz}}{Z_T})^2 + (\frac{\sigma_{xz}}{S_{xz}})^2 + (\frac{\sigma_{yz}}{S_{yz}})^2 \geq 1$
5	Delamination compressive	$(\frac{\sigma_{zz}}{Z_C})^2 + (\frac{\sigma_{xz}}{S_{xz}})^2 + (\frac{\sigma_{yz}}{S_{yz}})^2 \geq 1$
X: Fiber Direction	Y: Transverse to fibers	Z: Thickness direction

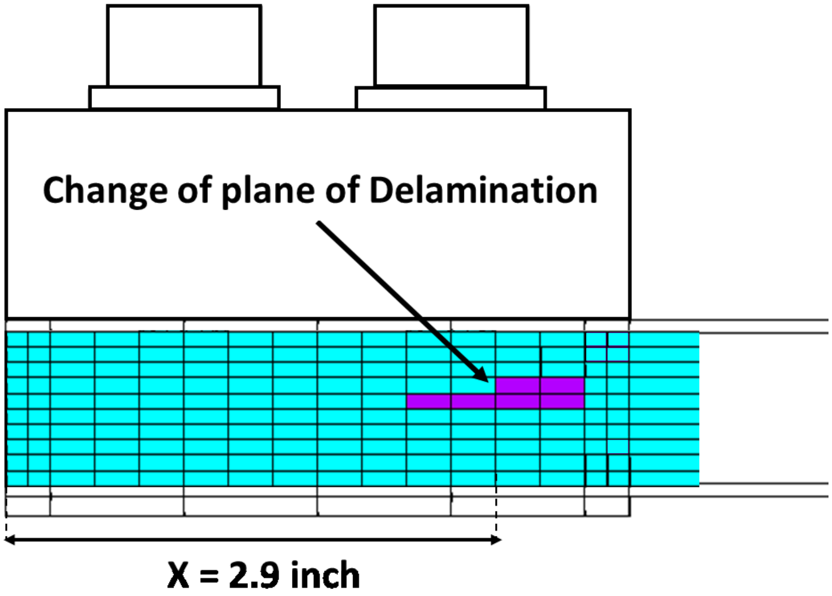

Figure 4-29: The position of the crack on the side surface of the cross-ply laminate – Failure analysis

To summarize, the proposed PDM model was modified to be applicable to cross-ply laminate. The introduced method to find the equivalent material properties for an element as a single block, can be applied for any other layup sequence. Although equivalent material properties and different degradation scenarios (comparing to unidirectional laminate) were utilized to simulate the failure of cross-ply laminate, the model is still able to predict failure behavior and ultimate displacement of the sample with acceptable accuracy. For further investigation, it is recommended to use different methods to find the equivalent material properties of the element and compare the accuracy of the method for different layup sequences.

5 Summary and Recommendations

The principal goal of this study was to introduce a numerical model to predict the structural behavior of thick laminated composite plate subjected to flexural bending loads in presence of the bolt joints. The results of stress analysis of thick composite were associated with a failure criterion and a progressive damage model in order to predict the failure initiation and propagation. This numerical model can be helpful for designers to predict the structural behavior of the yoke. Also, the finite element fully parametric simulation provides the ability to study the effect of different parameters such as bolt and washer size, number of layers and layers orientation on the failure behavior of the yoke in related loading conditions. Therefore, the developed stress and failure analysis model will be helpful to reduce the number of iterative experimental tests during the design process.

Three steps were selected to develop the final model:

To study the effect of bolt joint as the critical part of the whole assembly.

To improve the bolt joint model to include the major structural aspects of the yoke of helicopter in the simulation.

To develop the progressive damage model and incorporate it in the stress analysis package.

A summary of each of the above steps and some recommendation for further investigation are presented in the following.

5.1 Summary

In Chapter 2, the effect of the bolt joint on thick composite laminate was studied both numerically and experimentally. A fully parametric three-dimensional finite element model was developed using ANSYS. The preload force in the stud of the bolt was the only source of loading which was simulated utilizing pretension elements. Experimental tests were performed to find the relation between the clamping torque and the bolt preload which was required for the analysis. A similar mesh pattern and sizing were created manually on the contacted surfaces to increase the accuracy of the contact simulation and reduce the contact nonlinear solution time.

Experimental tests were carried out to validate the accuracy of the bolt joint modeling. In the first experimental approach, strain gages were utilized to measure strain at the external surfaces of top and thickness sides of the plate. Since strain gages provide data only at a specific point, Digital Image Correlation (DIC) method were used in parallel, to compare the fields of strain over nonfaying areas on both top and side surfaces of the plate. The DIC results provided the opportunity to validate full field displacement and strain distribution on external surfaces.

The results revealed that the maximum difference between strain gages and finite element analysis was in the order of or less than the gages sensitivity. This fact shows the accuracy of the finite element simulation in strain prediction. In general, it could be concluded that lateral strain at the top surface is higher comparing to axial strain at the points around the washer. The similar behavior observed for the gages installed on the side surface. Also, FEA and DIC methods agreed very well on the fields of strain distribution on both top and side surfaces. About the amount of strain, a better correlation was obtained on the top surface comparing to the thickness side.

The experimentally validated model was utilized to perform further studies on the effect of thickness of the plate on the interlaminar stresses. For a single bolt joint, interlaminar stresses thickness-wise distribution varied at different in plane positions. It was observed that even a slight change in washer and bolt size can affect significantly the interlaminar stresses distribution. As a conclusion, the effect of washer and bolt configuration on the interlaminar stresses is more considerable than the effect of the thickness of the plate.

The bolt joint model of Chapter 2, was improved in Chapter 3 to include the aspects of flexural bending of the plate. Two main configurations were numerically modeled and experimentally tested. In clamped-clamped configuration, bolt joints were utilized at each end of the plate while in cantilever model only the fixed end had four bolt joints. For finite element simulation, direct modeling was replaced by APDL programming to provide a fully parametric model which is well suited for parametric studies.

Although some of the experimental setup aspects were simplified during simulation to reduce the model complexity, the three-dimensional simulation included all major aspects of the experimental tests. The composite plate was meshed using layered solid element which was associated with a composite section to define layers orientation and thickness. The hydraulic actuator loading system was incorporated in finite element model for clamped-clamped sample while for the sake of simplicity the loading end mechanism was omitted from cantilever simulation. The accuracy of the numerical model was verified by two experimental methods using strain gages and Digital Image Correlation.

In general, the results showed a good correlation both qualitatively and quantitatively, between strains obtained from numerical simulation and Digital Image Correlation data, as well the strain gages. The proposed model accuracy in terms of strain prediction is higher for main strains (E.g. axial strain e_{XX} and interlaminar shear strain e_{XZ}). For the regions with lower strain (less than 500 microstrains), the correlation is not as good compared to the other areas. However, by considering the accuracy of the DIC (about 50 microstrain), the FEA results are still in an acceptable agreement with DIC.Due to the nature of the sample manufacturing process (i.e. vacuum bagging parts instead of cavity moulding), the sample did not have perfectly parallel surfaces from resin bleeding from the corners. This may be the source of some discrepancy between FEA, DIC, and strain gauge results which can be mitigated by improving the manufacturing process.

It was found that DIC is more practical in areas with higher strains. The difference between DIC and FEA was less than 5% for the ultimate strains, which is a significant achievement in terms of the correlation with experiments. DIC also provides the benefit of full field strain measurement over the spot measurements provided by strain gauges.

The verification process of the proposed model was repeated for the plates with different thicknesses in cantilever configuration. Similar to the 80-layer plate, good qualitative and quantitative correlation between ANSYS and DIC results obtained for plates with other thicknesses. The effect of the loading fixture which is not simulated in the finite element analysis of cantilever model, caused some discrepancies between numerical results and experimental data. This discrepancy was higher for the points located closer to the fixture (loading end). Also, the thinner plates are more sensitive to the loading mechanism affects.

A Progressive Damage Model (PDM) was introduced in Chapter 4 to perform failure initiation and propagation simulation, in presence of the bolt joint and flexural bending. Any

PDM requires a stress analysis tool and an appropriate failure criterion. The stress analysis method was introduced through Chapter 2 and Chapter 3 of the present thesis. To develop the failure analysis model, Hashin was selected as PDM failure criterion since it works with three-dimensional state of stress at each element and can be incorporated with the finite element numerical models introduced in Chapter 2 and Chapter 3. In addition, this criterion can distinguish between different modes of failure and identify the dominant stress that contributed in failure. The final failure of the plate was defined based on the propagation of the failed elements which was different for different loading conditions. In this research the best combination of the mesh density, load increment and material degradation percentage for PDM analysis, were selected through some trial and errors.

For failure analysis of the bolt joint, the plate was subjected to a single bolt joint and the clamping torque was gradually increased from zero up to the point that the cracks were visually detectable on the surfaces of the laminate. Since the crack initiation and propagation happened at the same time during experiment, the point at which the failed elements appeared in the analysis was introduced as the final failure torque of the plate. Although, the proposed failure model agreed with the experiment about the crack position and failure clamping torque, it is not able to simulate the sudden propagation of the crack after initiation.

For the failure experimental tests of the flexural beam, the final failure of the sample was defined as the point at which the axial force of the actuator dropped more than 50%. Comparing the actuator load profile and DIC images revealed that the plate failed right after the crack appearance on the side surface. This criterion was considered as the final failure definition during simulation.

For cantilever unidirectional sample failure simulation, at the loading level (actuator displacement) of 44 to 45 mm of displacement, the first failed elements appeared at the thickness side of the plate. The position of the failed elements across the thickness corresponds very well with the cracks observed during experiments. Also, the actuator displacement at which the first failed elements appeared on the side surface corresponds to the final failure of the sample, obtained from experiments.

The results showed that most of the element failed due to modes 6 and 7 (delamination) of Hashin criterion and the elements at the side surface mainly failed due to interlaminar shear stress (σ_{XZ}). At this region, the images of DIC revealed the second mode of delamination which corresponds well with the results found during simulation. Analysis of the unidirectional plates with different number of layers revealed that the failure initiation happens at lower deflection levels for thicker plates. Also, the thicker the plate is, the final failure happens earlier. At the same deflection level of 50 mm, the failure propagates over a significantly larger zone in 80-layer plate comparing to the other thinner ones.

It was experimentally observed that the cantilever cross-ply laminate failed at a higher actuator displacement and a lower actuator force, comparing to the unidirectional laminate and it had the failure delamination completely contained between the middle two 90-degree plies. For cross-ply sample, PDM agreed well with experiment and provided a more conservative failure prediction. Also, a good correlation was obtained about the failure behavior predicted by model and the experiment.

5.2 Recommendation

Although, Chapter 2 showed the viscoelastic behavior of thick composite laminates subjected to bolt joint loads and compared this phenomenon between composite and aluminium plates, a future study is recommended to consider the effect of thickness, material, and laminate layup sequence on the viscoelastic reaction rate and severity.

Since Chapter 3 introduced a fully parametric numerical model for flexural bending of thick composite laminate, a separate study is recommended to investigate the effect of different parameters such as bolt joint characteristic, material properties and layup sequence. Also, in-detail investigation of the thickness effect requires modeling and testing of plates with a wider range of thicknesses. The output of such a study could identify a clear border between thin and thick unidirectional composite flexural beams.

The proposed failure model in Chapter4, was not successful to simulate the sudden propagation of the crack after its appearance on the side surfaces. The code can be improved to capture this behavior which was observed in both bolt joint and flexural beam models.

6 Contributions

1. A numerical fully parametric model was developed to predict in plane and out-of-plane stresses in a composite bolt joint. Joint characteristics, number of layers, layup sequence, lamina thickness, material and loading conditions were defined as design parameters. This fully parametric model can be used for further parametric studies. Digital Image Correlation (DIC) and strain gages were utilized in parallel to measure the strain distribution on the surface around the washer and along the thickness of the laminate and validate the finite element model.
2. The interlaminar stress distribution were investigated for bolt joints in unidirectional laminates with the number of layers from 2 to 80 layers. Some guidelines were proposed to distinguish between thin and thick composites stress behavior based on the interlaminar stresses distributions.
3. The bolt joint model was improved to include the flexural bending effect. The flexural bending model can simulate the structural behavior of composite laminates with different geometry and layup sequence when subjected to flexural bending. The presented model included both flexural bending and bolt joint effects at the same time and was experimentally validated for composite laminates with a wide range of thicknesses.
4. The flexural bending model was validated using both strain gages and DIC for both unidirectional and cross-ply laminates under two different loading conditions. In clamped-clamped model, four bolt joints included at each side of laminate while cantilever model had only four bolts at fixed end. Finite element results revealed qualitative and quantitative agreements with experimental data. The investigation of the thickness effect was done both experimentally and numerically for flexural bending model.

5. A progressive damage model was introduced and incorporated in the bolt joint and flexural bending finite element simulations. Progressive Damage Model (PDM) was adapted to finite element model of thick composite laminate to predict both initiation and propagation of the failure. The final failure and the pattern of the crack propagation were compared with experimental results. The PDM degraded the properties of each failed element according to the corresponding failure mode.
6. Since for thick composite laminates, the initiation of the crack is not detectable during experiment, the proposed failure simulation method will be helpful to study the history of the failure from the initiation point. When the simulation analysis results revealed similar final failure and propagation pattern with the experiments, the pattern of the propagation of the failed elements was followed back to reach the initiation point.
7. The effect of the thickness and layup sequence on the failure behavior of composite laminates under flexural bending and bolt joint loads was investigated numerically and verified by the experiments.

References

[1] S. Van Hoa, *Principles of the manufacturing of composite materials*. DEStech Publications, Inc., 2009.

[2] “ANSYS Academic, Release 16.2, Help System, Mechanical APDL, Element Reference, ANSYS, Inc.” 2016.

[3] E. J.Barbero, *Introduction to composite materials design*, Second. CRC Press, 2011.

[4] D. Hull and T. W. Clyne, *An Introduction to Composite Materials*, Second. Cambridge University Press, 1996.

[5] F. L. Matthews and R. D. (Rees D. . Rawlings, *Composite materials : engineering and science*. 2008.

[6] J. N. (Junuthula N. Reddy and J. N. (Junuthula N. Reddy, *Mechanics of laminated composite plates and shells : theory and analysis*. CRC Press, 2004.

[7] J. M. Whitney and A. W. Leissa, “Analysis of Heterogeneous Anisotropic Plates,” *J. Appl. Mech.*, vol. 36, no. 2, p. 261, Jun. 1969.

[8] S. B. Dong, “On the Theory of Laminated Anisotropic Shells and Plates,” *J. Aerosp. Sci.*, vol. 29, no. 8, pp. 969–975, Aug. 1962.

[9] E. Carrera, “Theories and finite elements for multilayered, anisotropic, composite plates and shells,” *Arch. Comput. Methods Eng.*, vol. 9, no. 2, pp. 87–140, Jun. 2002.

[10] J. M. Whitney, “The Effect of Transverse Shear Deformation on the Bending of Laminated Plates,” *J. Compos. Mater.*, vol. 3, no. 3, pp. 534–547, Mar. 1969.

[11] M. H. TOORANI and A. A. LAKIS, “GENERAL EQUATIONS OF ANISOTROPIC PLATES AND SHELLS INCLUDING TRANSVERSE SHEAR DEFORMATIONS, ROTARY INERTIA AND INITIAL CURVATURE EFFECTS,” *J. Sound Vib.*, vol. 237, no. 4, pp. 561–615, Nov. 2000.

[12] J. M. Whitney and N. J. Pagano, “Shear Deformation in Heterogeneous Anisotropic Plates,” *J. Appl. Mech.*, vol. 37, no. 4, p. 1031, Dec. 1970.

[13] K. H. Lo, R. M. Christensen, and E. M. Wu, “A High-Order Theory of Plate Deformation—Part 2: Laminated Plates,” *J. Appl. Mech.*, vol. 44, no. 4, p. 669, Dec. 1977.

[14] K. H. Lo, R. M. Christensen, and E. M. Wu, “A High-Order Theory of Plate Deformation—Part 1: Homogeneous Plates,” *J. Appl. Mech.*, vol. 44, no. 4, p. 663, Dec. 1977.

[15] N. D. Phan and J. N. Reddy, “Analysis of laminated composite plates using a higher-order shear deformation theory,” *Int. J. Numer. Methods Eng.*, vol. 21, no. 12, pp. 2201–2219, Dec. 1985.

[16] J. N. (Junuthula N. Reddy and C. F. Liu, “A higher-order shear deformation theory of laminated elastic shells,” *Int. J. Eng. Sci.*, vol. 23, no. 3, pp. 319–330, Jan. 1985.

[17] J. N. Reddy, “A Simple Higher-Order Theory for Laminated Composite Plates,” *J. Appl. Mech.*, vol. 51, no. 4, p. 745, Dec. 1984.

[18] E. Carrera, “Evaluation of Layerwise Mixed Theories for Laminated Plates Analysis,” *AIAA J.*, vol. 36, no. 5, pp. 830–839, May 1998.

[19] E. REISSNER, “A Consistent Treatment of Transverse Shear Deformations in Laminated Anisotropic Plates,” *AIAA J.*, vol. 10, no. 5, pp. 716–718, May 1972.

[20] D. H. Robbins and J. N. Reddy, “Modelling of thick composites using a layerwise laminate theory,” *Int. J. Numer. Methods Eng.*, vol. 36, no. 4, pp. 655–677, Feb. 1993.

[21] C. P. Wu and H. C. Kuo, “An interlaminar stress mixed finite element method for the analysis of thick laminated composite plates,” *Compos. Struct.*, vol. 24, pp. 29–42, 1993.

[22] J. Y. Kim and C. S. Hong, “Three-dimensional finite element analysis of interlaminar stresses in thick composite laminates,” *Comput. Struct.*, vol. 40, no. 6, pp. 1395–1404, 1991.

[23] M. Tahani and A. Andakhshideh, “Interlaminar stresses in thick rectangular laminated plates with arbitrary laminations and boundary conditions under transverse loads,” *Compos. Struct.*, vol. 94,

no. 5, pp. 1793–1804, 2012.

[24] R. B. Pipes, “Interlaminar Stresses in Composite Laminates Under Uniform Axial Extension,” *J. Compos. Mater.*, vol. 4, no. October, pp. 538–548, 1970.

[25] E. J. BARBERO, J. N. REDDY, and J. L. TEPLY, “General two-dimensional theory of laminated cylindrical shells,” *AIAA J.*, vol. 28, no. 3, pp. 544–553, Mar. 1990.

[26] K. P. Soldatos and P. Watson, “A method for improving the stress analysis performance of one- and two-dimensional theories for laminated composites,” *Acta Mech.*, vol. 123, no. 1–4, pp. 163–186, Mar. 1997.

[27] J. N. Reddy, “A generalization of two-dimensional theories of laminated composite plates,” *Commun. Appl. Numer. Methods*, vol. 3, no. 3, pp. 173–180, May 1987.

[28] A. K. Noor and M. D. Mathers, “Nonlinear finite-element analysis of laminated composite shells,” Jan. 1974.

[29] K. M. Rao and H.-R. Meyer-Piening, “Analysis of thick laminated anisotropic composite plates by the finite element method,” *Compos. Struct.*, vol. 15, no. 3, pp. 185–213, 1990.

[30] H. Yildiz and M. Sarikanat, “Finite-element analysis of thick composite beams and plates,” *Compos. Sci. Technol.*, vol. 61, no. 12, pp. 1723–1727, 2001.

[31] K. Zimmermann, D. Zenkert, and M. Siemetzki, “Testing and analysis of ultra thick composites,” *Compos. Part B Eng.*, vol. 41, no. 4, pp. 326–336, 2010.

[32] E. E. Theotokoglou, “Behaviour of thick composite tubes considering of delamination,” *Theor. Appl. Fract. Mech.*, 2006.

[33] W. Hufenbach, R. Gottwald, B. Grüber, M. Lepper, and B. Zhou, “Stress concentration analysis of thick-walled laminate composites with a loaded circular cut-out by using a first-order shear deformation theory,” *Compos. Sci. Technol.*, vol. 68, no. 10–11, pp. 2238–2244, 2008.

[34] R. B. Heslehurst, *Design and analysis of structural joints with composites materials*. DEStech

Publications, Inc., 2013.

[35] Y. Yang, H. Qinshu, and C. Fu, “Three-Dimensional Finite Element Analysis of Composite Bolted Joints,” in *Second International Conference on Computer Modeling and Simulation*, 2010, pp. 344–347.

[36] J. Montgomery, “Methods for Modeling Bolts in the Bolted Joint,” in *ANSYS User’s Conference*, 2002.

[37] J. F. Chen, E. V. Morozov, and K. Shankar, “Simulating progressive failure of composite laminates including in-ply and delamination damage effects,” *Compos. Part A Appl. Sci. Manuf.*, vol. 61, pp. 185–200, 2014.

[38] S. D. Thoppul, J. Finegan, and R. F. Gibson, “Mechanics of mechanically fastened joints in polymer-matrix composite structures - A review,” *Compos. Sci. Technol.*, vol. 69, no. 3–4, pp. 301–329, 2009.

[39] W. H. Chen and S. S. Lee, “Numerical and experimental failure analysis of composite laminates with bolted joints under bending loads,” *J. Compos. Mater.*, vol. 29, no. 10, pp. 15–36, 1999.

[40] W.-H. Chen, S.-S. Lee, and J.-T. Yeh, “Three-dimensional contact stress analysis of a composite laminate with bolted joint,” *Compos. Struct.*, vol. 30, no. 3, pp. 287–297, 1995.

[41] T. Ireman, “Three-dimensional stress analysis of bolted single-lap composite joints,” *Compos. Struct.*, vol. 43, pp. 195–216, 1998.

[42] U. A. Khashaba, H. E. M. Sallam, A. E. Al-Shorbagy, and M. A. Seif, “Effect of washer size and tightening torque on the performance of bolted joints in composite structures,” *Compos. Struct.*, vol. 73, no. 3, pp. 310–317, Jun. 2006.

[43] S. Hsien-Tang, C. Fu-Kuo, and Q. Xilin, “The response of composite joints with bolt-clamping loads Part II: Model Verification,” *J. Compos. Mater.*, vol. 36, no. 1, pp. 69–92, 2002.

[44] S. Hsien-Tang, C. Fu-Kuo, and Q. Xilin, “The response of composite joints with bolt-clamping loads

Part I: Model Development," *J. Compos. Mater.*, vol. 36, no. 1, pp. 47–67, 2002.

[45] a. Olmedo, C. Santiuste, and E. Barbero, "An analytical model for the secondary bending prediction in single-lap composite bolted-joints," *Compos. Struct.*, vol. 111, no. 1, pp. 354–361, 2014.

[46] P. A. Sharos, B. Egan, and C. T. McCarthy, "An analytical model for strength prediction in multi-bolt composite joints at various loading rates," *Compos. Struct.*, vol. 116, pp. 300–310, 2014.

[47] M. A. McCarthy, V. P. Lawlor, P. C. O'Donnell, K. Harris, P. Kelly, and J. P. Cunningham, "Measurement of Bolt Pre-load in Torqued Composite Joints," *Strain*, vol. 41, no. 3, pp. 109–112, Aug. 2005.

[48] Z. Q. Wang, S. Zhou, J. S. Zhou, and X. Y. Sun, "Properties Analysis of Bolted Composite T-Joint," *Key Eng. Mater.*, vol. 467–469, pp. 575–578, Feb. 2011.

[49] C. Friedrich and H. Hubbertz, "Friction behavior and preload relaxation of fastening systems with composite structures," *Compos. Struct.*, vol. 110, no. 1, pp. 335–341, 2014.

[50] S. J. Kim and J. H. Kim, "Finite element analysis of laminated composite plates with multi-pin joints considering friction," *Comput. Struct.*, vol. 55, no. 3, pp. 507–514, 1995.

[51] C. T. McCarthy, M. A. McCarthy, W. F. Stanley, and V. P. Lawlor, "Experiences with Modeling Friction in Composite Bolted Joints," *J. Compos. Mater.*, vol. 39, no. 21, pp. 1881–1908, 2005.

[52] S. Żółkiewski, "TESTING COMPOSITE MATERIALS CONNECTED IN BOLT JOINTS," *J. VIBROENGINEERING*, vol. 13, pp. 817–822, 2011.

[53] J. Zhang, Z. Ma, X. Cheng, and G. Chen, "Finite element model and load distribution analysis for three-bolted single-lap composite joints," *Mater. Compos. Sin.*, vol. 29, no. 3, pp. 179–183, 2012.

[54] J. Matuszewski, "Fastener guidelines for composite materials," *Mater. Technol.*, vol. 19, pp. 2032–210, 2004.

[55] P. P. Camanho and F. L. Matthews, "Stress analysis and strength prediction of mechanically

fastened joints in FRP: a review," *Compos. Part A Appl. Sci. Manuf.*, vol. 28, no. 6, pp. 529–547, Jan. 1997.

[56] W. S. Chan and S. Vedhagiri, "Analysis of Composite Bonded/Bolted Joints Used in Repairing," *J. Compos. Mater.*, vol. 35, no. 12, pp. 1045–1061, Jun. 2001.

[57] M. L. Dano, G. Gendron, and A. Picard, "Stress and failure analysis of mechanically fastened joints in composite laminates," *Compos. Struct.*, vol. 50, no. 3, pp. 287–296, Nov. 2000.

[58] L. Feo, G. Marra, and A. S. Mosallam, "Stress analysis of multi-bolted joints for FRP pultruded composite structures," *Compos. Struct.*, vol. 94, no. 12, pp. 3769–3780, Dec. 2012.

[59] R. E. Rowlands, M. U. Rahman, T. L. Wilkinson, and Y. I. Chiang, "Single- and multiple-bolted joints in orthotropic materials," *Composites*, vol. 13, no. 3, pp. 273–279, Jul. 1982.

[60] P. J. Gray and C. T. McCarthy, "A global bolted joint model for finite element analysis of load distributions in multi-bolt composite joints," *Compos. Part B Eng.*, vol. 41, no. 4, pp. 317–325, Jun. 2010.

[61] S. a. Nassar, V. L. Virupaksha, and S. Ganeshmurthy, "Effect of Bolt Tightness on the Behavior of Composite Joints," *J. Press. Vessel Technol.*, vol. 129, no. 1, p. 43, 2007.

[62] B. Egan, C. T. McCarthy, M. A. McCarthy, and R. M. Frizzell, "Stress analysis of single-bolt, single-lap, countersunk composite joints with variable bolt-hole clearance," *Compos. Struct.*, vol. 94, no. 3, pp. 1038–1051, Feb. 2012.

[63] B. Sergeev, E. Madenci, and D. R. Ambur, "Influence of bolt spacing and degree of anisotropy in single-lap joints," *Comput. Struct.*, vol. 76, no. 1, pp. 89–103, 2000.

[64] G. A. Isaicu, X. Ding, G. L. Cloud, and B. B. Raju, "3-D Experimental and Numerical Analyses of Single-lap Bolted Joints in Thick Composites," in *SEM Annual Conference & Exposition on Experimental and Applied Mechanics*, 2005.

[65] G. L. Cloud, X. Ding, S. Thelander, and B. B. Raju, "Strains beneath washers in thick single-lap

composite bolted joint using embedded DSPI and RSG's .," in *SEM Annual Conference & Exposition on Experimental and Applied Mechanics*, 2005.

[66] G. Restivo, G. Marannano, and G. a Isaicu, "Three-dimensional strain analysis of single-lap bolted joints in thick composites using fibre-optic gauges and the finite-element method," *J. Strain Anal. Eng. Des.*, vol. 45, no. 7, pp. 523–534, 2010.

[67] J. H. Stockdale and F. L. Matthews, "The effect of clamping pressure on bolt bearing loads in glass fibre-reinforced plastics," *Composites*, vol. 7, no. 1, pp. 34–38, Jan. 1976.

[68] T. A. Collings, "The strength of bolted joints in multi-directional cfrp laminates," *Composites*, vol. 8, no. 1, pp. 43–55, Jan. 1977.

[69] F.-K. Chang, R. A. Scott, and G. S. Springer, "Strength of Mechanically Fastened Composite Joints," *J. Compos. Mater.*, vol. 16, no. 6, pp. 470–494, Nov. 1982.

[70] C. Cooper and G. J. Turvey, "Effects of joint geometry and bolt torque on the structural performance of single bolt tension joints in pultruded GRP sheet material," *Compos. Struct.*, vol. 32, no. 1–4, pp. 217–226, Jan. 1995.

[71] Y. Yan, W. D. Wen, F. K. Chang, and P. Shyprykevich, "Experimental study on clamping effects on the tensile strength of composite plates with a bolt-filled hole," *Compos. Part A Appl. Sci. Manuf.*, vol. 30, no. 10, pp. 1215–1229, Oct. 1999.

[72] M. A. McCarthy, V. P. Lawlor, W. F. Stanley, and C. T. McCarthy, "Bolt-hole clearance effects and strength criteria in single-bolt, single-lap, composite bolted joints," *Compos. Sci. Technol.*, vol. 62, no. 10–11, pp. 1415–1431, Aug. 2002.

[73] G. Kelly and S. Hallström, "Bearing strength of carbon fibre/epoxy laminates: Effects of bolt-hole clearance," *Compos. Part B Eng.*, vol. 35, no. 4, pp. 331–343, Jan. 2004.

[74] Y. Xiao and T. Ishikawa, "Bearing strength and failure behavior of bolted composite joints (part II: Modeling and simulation)," *Compos. Sci. Technol.*, vol. 65, no. 7–8, pp. 1032–1043, Jun. 2005.

[75] H.-S. Wang, C.-L. Hung, and F.-K. Chang, “Bearing Failure of Bolted Composite Joints. Part I: Experimental Characterization,” *J. Compos. Mater.*, vol. 30, no. 12, pp. 1284–1313, Aug. 1996.

[76] H. J. Park, “Effects of stacking sequence and clamping force on the bearing strengths of mechanically fastened joints in composite laminates,” *Compos. Struct.*, vol. 53, no. 2, pp. 213–221, Aug. 2001.

[77] K. I. Tserpes, G. Labeas, P. Papanikos, and T. Kermanidis, “Strength prediction of bolted joints in graphite/epoxy composite laminates,” *Compos. Part B Eng.*, vol. 33, no. 7, pp. 521–529, Oct. 2002.

[78] Y. Xiao and T. Ishikawa, “Bearing strength and failure behavior of bolted composite joints (part I: Experimental investigation),” *Compos. Sci. Technol.*, vol. 65, no. 7–8, pp. 1022–1031, Jun. 2005.

[79] Á. Olmedo and C. Santiuste, “On the prediction of bolted single-lap composite joints,” *Compos. Struct.*, vol. 94, no. 6, pp. 2110–2117, May 2012.

[80] U. A. Khashaba, T. A. Sebaey, and K. A. Alnefaie, “Failure and reliability analysis of pinned-joints composite laminates: Effects of stacking sequences,” *Compos. Part B Eng.*, vol. 45, no. 1, pp. 1694–1703, Feb. 2013.

[81] A. Öndürücü, Ü. Esendemir, and R. F. Tunay, “Progressive failure analysis of glass-epoxy laminated composite pinned-joints,” *Mater. Des.*, vol. 36, pp. 617–625, Apr. 2012.

[82] S. Goswami, “A Finite Element Investigation on Progressive Failure Analysis of Composite Bolted Joints Under Thermal Environment,” *J. Reinf. Plast. Compos.*, vol. 24, no. 2, pp. 161–171, Jan. 2005.

[83] T. E. Tay, G. Liu, V. B. C. Tan, X. S. Sun, and D. C. Pham, “Progressive Failure Analysis of Composites,” *J. Compos. Mater.*, vol. 42, no. 18, pp. 1921–1966, Sep. 2008.

[84] Z. Wang, S. Zhou, J. Zhang, X. Wu, and L. Zhou, “Progressive failure analysis of bolted single-lap composite joint based on extended finite element method,” *Mater. Des.*, vol. 37, pp. 582–588,

May 2012.

[85] A. Riccio, “Effects of Geometrical and Material Features on Damage Onset and Propagation in Single-lap Bolted Composite Joints under Tensile Load: Part II – Numerical Studies,” *J. Compos. Mater.*, vol. 39, no. 23, pp. 2091–2112, Dec. 2005.

[86] M. Ozen and O. Sayman, “Failure loads of mechanical fastened pinned and bolted composite joints with two serial holes,” *Compos. Part B Eng.*, vol. 42, no. 2, pp. 264–274, Mar. 2011.

[87] V. P. Lawlor, M. A. McCarthy, and W. F. Stanley, “An experimental study of bolt-hole clearance effects in double-lap, multi-bolt composite joints,” *Compos. Struct.*, vol. 71, no. 2, pp. 176–190, Nov. 2005.

[88] F. Sen, M. Pakdil, O. Sayman, and S. Benli, “Experimental failure analysis of mechanically fastened joints with clearance in composite laminates under preload,” *Mater. Des.*, vol. 29, no. 6, pp. 1159–1169, Jan. 2008.

[89] C. T. McCarthy, M. A. McCarthy, and V. P. Lawlor, “Progressive damage analysis of multi-bolt composite joints with variable bolt-hole clearances,” *Compos. Part B Eng.*, vol. 36, no. 4, pp. 290–305, Jun. 2005.

[90] J. H. Kweon, J. W. Jung, T. H. Kim, J. H. Choi, and D. H. Kim, “Failure of carbon composite-to-aluminum joints with combined mechanical fastening and adhesive bonding,” *Compos. Struct.*, vol. 75, no. 1–4, pp. 192–198, Sep. 2006.

[91] T. S. Lim, B. C. Kim, and D. G. Lee, “Fatigue characteristics of the bolted joints for unidirectional composite laminates,” *Compos. Struct.*, vol. 72, no. 1, pp. 58–68, Jan. 2006.

[92] T. S. Lim, B. C. Kim, and D. G. Lee, “Fatigue characteristics of the bolted joints for unidirectional composite laminates,” 2004.

[93] M. a. McCarthy, C. T. McCarthy, V. P. Lawlor, and W. F. Stanley, “Three-dimensional finite element analysis of single-bolt, single-lap composite bolted joints: part I—model development

and validation," *Compos. Struct.*, vol. 71, no. 2, pp. 140–158, 2005.

[94] C. T. McCarthy and M. A. McCarthy, "Three-dimensional finite element analysis of single-bolt, single-lap composite bolted joints: Part II - Effects of bolt-hole clearance," *Compos. Struct.*, vol. 71, no. 2, pp. 159–175, Nov. 2005.

[95] V. Kradinov, E. Madenci, and D. R. Ambur, "Application of genetic algorithm for optimum design of bolted composite lap joints," *Compos. Struct.*, vol. 77, no. 2, pp. 148–159, Jan. 2007.

[96] J. ZHANG, L. LIU, K. CHEN, and H. WANG, "Influence of Bolt-hole Interference Fit Conditions on Load Capacity in Composite Mechanical Joints," *J. Shanghai Jiaotong Univ.*, 2013.

[97] Y. S. Liu, X. J. Shao, and Z. F. Yue, "Study of Three-Dimensional Stress Distribution and Damage Characterization of Bolt Composite Joint," *Key Eng. Mater.*, vol. 324–325, pp. 395–398, 2006.

[98] Y. Pekbey, "Experimental characterization of an E-glass/epoxy composite plate in pin-loaded joints," *Adv. Compos. Lett.*, vol. 16, no. 2, pp. 55–63, 2007.

[99] M. L. Dano, E. Kamal, and G. Gendron, "Analysis of bolted joints in composite laminates: Strains and bearing stiffness predictions," *Compos. Struct.*, vol. 79, no. 4, pp. 562–570, 2007.

[100] G. Murri, S. Salpekar, and T. O'Brien, "Fatigue Delamination Onset Prediction in Unidirectional Tapered Laminates," in *Composite Materials: Fatigue and Fracture (Third Volume)*, 100 Barr Harbor Drive, PO Box C700, West Conshohocken, PA 19428-2959: ASTM International, 1991, pp. 312-312–28.

[101] J. A. Speck, *Mechanical fastening, joining, and assembly*. Marcel Dekker, 1997.

[102] H. Hamidi, "CONCOM-BellFlex-03-Material Characterization Procedure and Plan," Concordia University, Montreal, Canada, 2017.

[103] "ANSYS Modeling and Meshing Guide," 2005.

[104] "Vic-2D V6 Reference Manual, Correlated Solutions Incorporated (C.S.Inc)."

[105] C. S. HEER, "Flexural Test Setup," M.Eng Project Report, Mechanical Engineering Department,

Supervisors S.V. Hoa and R. Ganesan, Concordia University, Montreal, Canada, Montreal, 2013.

[106] J. F. SIMPSON, A. GORJIPOOR, and S. VAN HOA, “Effect of Boundary Conditions on the Cantilever Bending of Thick Glass Fiber Reinforced Polymer (GFRP) Composite Plates,” in *International Workshop, Mechanical Behavior of Thick Composites*, 2016.

[107] A. Gorjipoor, J. F. Simpson, R. Ganesan, and S. V. Hoa, “Computational and experimental strain analysis of flexural bending of thick glass/epoxy laminates,” *Compos. Struct.*, vol. 176, 2017.

[108] P. P. Camanho, *FAILURE CRITERIA FOR FIBRE-REINFORCED POLYMER COMPOSITES*. Departamento de Engenharia Mecânica e Gestăo Industrial, Faculdade de Engenharia da Universidade do Porto, 2002.

[109] Z. Hashin, “Failure Criteria for Unidirectional FibreComposites,” *J. Appl. Mech.*, vol. 47, pp. 329–334, 1980.

[110] M. Shokrieh, L. Lessard, and C. Poon, “Three-Dimensional Progressive Failure Analysis of Pin/Bolt Loaded Composite Laminates,” in *AGARD590 CONFERENCE PROCEEDINGS*, p. (7-1)-(7-10), Sept 1996.

[111] L. Lessard, “Compression failure in laminated composites containing an open hole,” Stanford University, CA, USA., 1989.

[112] K. I. Tserpes, P. Papanikos, and T. H. Kermanidis, “A three-dimensional progressive damage model for bolted joints in composite laminates subjected to tensile loading,” *Fatigue Fract. Eng. Mater. Struct.*, vol. 24, pp. 663–675, 2001.

[113] “ANSYS Parametric Design Language Guide,” 2009.

[114] J. Bonet and R. D. Wood, *Nonlinear Continuum Mechanics for Finite Element Analysis*. Cambridge University Press., 1997.

[115] M. Gadala and J. Wang, “No TitleSimulation of Metal Forming Processes with Finite Element Methods". International Journal for Numerical Methods in Engineering,” *Int. J. Numer. Methods*

Eng., vol. 44, pp. 1397–1428, 1999.

[116] S. Cescotto and R. Charilier, “Frictional Contact Finite Elements Based on Mixed Variational Principles,” *Int. J. Numer. Method Eng.*, vol. 36, pp. 1681–1701, 1992.

[117] S. Cescotto and Y. Zhu, “Large Strain Dynamic Analysis Using Solid and Contact Finite Elements Based on a Mixed Formulation - Application to Metalforming,” *J. Met. Process. Technol.*, vol. 45, pp. 657–663, 1994.

[118] J. Simo and T. Laursen, “An Augmented Lagrangian Treatment of Contact Problems Involving Friction,” *Comput. Struct.*, vol. 42, no. No. 1, pp. 97–116, 1992.

[119] “ANSYS Mechanical APDL Theory Reference,” *ANSYS Inc*, vol. Release15, no. November, pp. 1–909, 2013.

Publications

Conferences

- A. Gorjipoor, R. Ganesan, S. V. Hoa, “Effect of thickness on interlaminar stresses in composite laminate with bolt joints”, 10th Canadian-International Conference on Composites, July 2017, Ottawa, Canada.
- A. Gorjipoor, S. V. Hoa, R. Ganesan, “Investigation the effect of thickness on failure propagation in a composite flexural beam”, 3rd International Conference on Mechanics of Composites, July 2017, Bologna, Italy.
- J. Fortin Simpson, A. Gorjipoor, S.V. Hoa, “Effect of Boundary Conditions on the Cantilever Bending of Thick Glass Fiber Reinforced Polymer (GFRP) Composite Plates”, International Workshop on Mechanical Behavior of Thick Composites, March 2016, Montreal, Canada.
- A. Gorjipoor, S. V. Hoa, R. Ganesan, “Failure Prediction in Thick Composite Laminate Subjected to Bolt Loads”, International Workshop on Mechanical Behavior of Thick Composites, March 2016, Montreal, Canada.
- A. Gorjipoor, R. Ganesan, S.V. Hoa, “Effect of Washer Size and Clamping Torque on Thick Composite Bolted Joints”, CANCOM 2015, Edmonton, Canada, Aug 2015.
- A. Gorjipoor, R. Ganesan, S.V. Hoa, F. Shadmehri, "Stress analysis of a thick composite laminate with a bolted joint ", 10th Canada-Japan Workshop on Composites, Vancouver, Canada, Aug 2014.

Journals

- A. Gorjipoor, S. V. Hoa and R. Ganesan, “Numerical model for investigation of the strain distribution in thick composite plates subjected to bolt load”, Aerospace Science and Technology, Volume 59, December 2016, Pages 94-102.
- A. Gorjipoor, J.F. Simpson, R. Ganesan, S.V. Hoa, “Computational and experimental strain analysis of flexural bending of thick glass/epoxy laminates”, Composite Structures, Volume 176, 15 September 2017, Pages 526-538.

Appendix A

A review of the elements

Solid 186

SOLID186 is a higher order 3-D 20-node solid element that exhibits quadratic displacement behavior. The element is defined by 20 nodes having three degrees of freedom per node: translations in the nodal x, y, and z directions. The element supports plasticity, hyper elasticity, creep, stress stiffening, large deflection, and large strain capabilities. It also has mixed formulation capability for simulating deformations of nearly incompressible elastoplastic materials, and fully incompressible hyper-elastic materials. A lower-order version of the SOLID186 element is SOLID185. To model layered thick shells or solids, the layered section definition is given by ANSYS section (SECxxx) commands.

SOLID186 is available in two forms:

1. Homogeneous Structural Solid
2. Layered Structural Solid

The characteristics of layered solid element are as following:

- This element is primarily intended for conveniently modeling the in-plane effects in layered thick shells or solids. The in-plane stiffness is the average of the individual layer stiffnesses. For complicated through-thickness behaviors, consider using multiple layers of homogeneous (non-layered) SOLID186 elements.
- The element must not have a zero volume. Also, the element may not be twisted such that the element has two separate volumes (which occurs most frequently when the element is not numbered properly).
- An edge with a removed mid-side node implies that the displacement varies linearly, rather than parabolically, along that edge.
- If the material of a layer is hyper-elastic, the layer orientation angle has no effect.
- To obtain more accurate transverse shear results, multiple elements must be generated though the thickness.
- The shape function to find nodal displacement and temperature is like Equation A-1. See Figure A-1 for notations. The element temperature is considered bilinear in-plane of the

element and linear through each layer. For more details refer to [[39] O. C. Zienkiewicz. ***The Finite Element Method***. McGraw-Hill Company. London. 1977.]

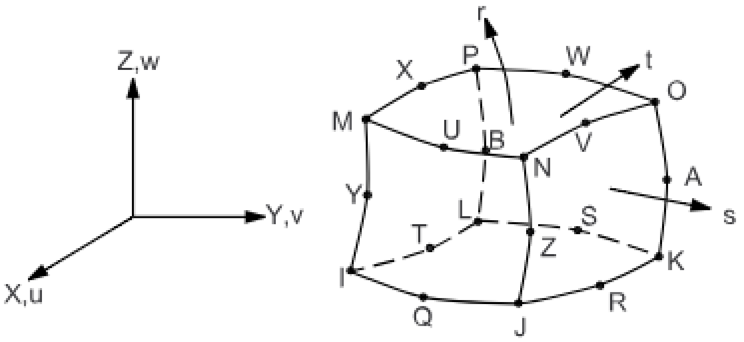

Figure A-1: 20-Node solid element

$$
\begin{aligned}
u=\tfrac{1}{8}\big(&u_I(1-s)(1-t)(1-r)(-s-t-r-2)+u_J(1+s)(1-t)(1-r)(s-t-r-2)\\
&+u_K(1+s)(1+t)(1-r)(s+t-r-2)+u_L(1-s)(1+t)(1-r)(-s+t-r-2)\\
&+u_M(1-s)(1-t)(1+r)(-s-t+r-2)+u_N(1+s)(1-t)(1+r)(s-t+r-2)\\
&+u_O(1+s)(1+t)(1+r)(s+t+r-2)+u_P(1-s)(1+t)(1+r)(-s+t+r-2)\big)\\
&+\tfrac{1}{4}\big(u_Q(1-s^2)(1-t)(1-r)+u_R(1+s)(1-t^2)(1-r)\\
&+u_S(1-s^2)(1+t)(1-r)+u_T(1-s)(1-t^2)(1-r)\\
&+u_U(1-s^2)(1-t)(1+r)+u_V(1+s)(1-t^2)(1+r)\\
&+u_W(1-s^2)(1+t)(1+r)+u_X(1-s)(1-t^2)(1+r)\\
&+u_Y(1-s)(1-t)(1-r^2)+u_Z(1+s)(1-t)(1-r^2)\\
&+u_A(1+s)(1+t)(1-r^2)+u_B(1-s)(1+t)(1-r^2)\big)
\end{aligned}
$$

Equation A-1

Element formulations presented in this section are based on the principle of virtual work. These formulations have been implemented in PLANE182, PLANE183, SOLID185, SOLID186. For more details refer to [113].

Fundamental Equations

General finite strain deformation has the following characteristics:

- Geometry changes during deformation. The deformed domain at a particular time is generally different from the undeformed domain and the domain at any other time.
- Strain is no longer infinitesimal so that a large-strain definition has to be employed.
- Cauchy stress cannot be updated simply by adding its increment. It has to be updated by a particular algorithm in order to take into account the finite deformation.
- Incremental analysis is necessary to simulate the nonlinear behaviors.

The updated Lagrangian method is applied to simulate geometric nonlinearities. Assuming all variables, such as coordinates x_i, displacements u_i, strains ε_{ij}, stresses σ_{ij}, velocities v_i, volume V and other material variables have been solved for and are known at time t; one solves for a set of linearized simultaneous equations having displacements (and hydrostatic pressures in the mixed u-P formulation) as primary unknowns to obtain the solution at time t + Δt. These simultaneous equations are derived from the element formulations which are based on the principle of virtual work:

$$\int_{v} \sigma_{ij} \delta e_{ij} dV = \int_{v} f_i^B \delta u_i dV + \int_{s} f_i^S \delta u_i ds$$

where:

σ_{ij} = Cauchy stress component

$e_{ij} = \frac{1}{2}\left(\frac{\partial u_i}{\partial x_j} + \frac{\partial u_j}{\partial x_i}\right)$ = deformation tensor

u_i = displacement

x_i = current coordinate

f_i^B = component of body force

f_i^S = component of surface traction

V = volume of deformed body

S = surface of deformed body on which tractions are prescribed

The internal virtual work can be indicated by:

$$\delta W = \int_V \sigma_{ij} \delta e_{ij} dV$$

Element formulations are obtained by differentiating this virtual work expression [114] and [115]. In derivation, only linear differential terms are kept and all higher order terms are ignored so that finally a linear set of equations can be obtained. Two methods were used to obtain the solution:

1. Pure displacement formulation takes displacements or velocities as primary unknown variables. All other quantities such as strains, stresses and state variables in history-dependent material models are derived from the displacements. It is the most widely used formulation and is able to handle most nonlinear deformation problems.
2. In mixed U-P formulations the hydrostatic pressure or volume change rate is interpolated on the element level and solved on the global level independently in the same way as displacements.

Both methods have some pros and cons which are explained in detail in [ANSYS REF APDL].

CONTA 174/TARGE 170

CONTA174 is an 8-node element that is intended for general rigid-flexible and flexible-flexible contact analysis. In a general contact analysis, the area of contact between two (or more) bodies is generally not known in advance. CONTA174 is applicable to 3-D geometries. It may be applied for contact between solid bodies or shells. For flexible-flexible contact, both contact and target surfaces are associated with deformable bodies. The contact and target surfaces constitute a "Contact Pair".
The CONTA174 contact element is associated with the 3-D target segment elements (TARGE170) using a shared real constant set number. This element is located on the surface of 3-D solid, shell elements (called underlying element). It has the same geometric characteristics as the underlying elements. The contact surface can be either side or both sides of the shell or beam elements.

CONTA174 uses Gauss integration points by default ([116] and [117]) which generally provides more accurate results than when using the nodes themselves as the integration points.

Four different contact algorithms are implemented in this element:

- Pure penalty method
- Augmented Lagrangian method [118].
- Pure Lagrange multiplier method
- Lagrange multiplier on contact normal and penalty on frictional direction

For details of each method refer to [119].